Technische Universität München

Walther-Meissner-Institut

Bayerische Akademie der Wissenschaften

Frequency control and sensing of mechanical properties in nanostring-based electromechanics

Master's thesis

Lukas Niekamp

Supervisor: PD Dr. Hans Huebl

Advisor: Thomas Luschmann

Garching – December 20, 2022

Abstract

The field of cavity electromechanics studies the interaction between electromagnetic modes confined in superconducting microwave cavities and mechanical resonators. Recently, the concept of inductive coupling has been demonstrated, where the inductance of the microwave circuit is modulated by the mechanical displacement. This coupling scheme allows for higher vacuum optomechanical coupling rates and is therefore considered a promising approach for reaching the single-photon strong coupling regime.

In this work, we report on efforts towards entering this regime. We present a novel fabrication process for a flux-tunable microwave resonator that is shunted to ground by a dc-SQUID with integrated nanostrings. This multi-step process is expected to enable higher internal quality factors that are an essential requirement for single-photon strong coupling. We characterize two of the flux-tunable resonators and find a major improvement of internal quality factors from the first to the second sample. However, both samples show hysteretic behavior which demands for a further optimization of the device geometry. In addition, we investigate the shift of the uncoupled mechanical frequency of a nanostring integrated into a SQUID and consider the creation of flux vortex lines inside the nanostring as a possible explanation for this residual frequency shift.

Contents

Chapter 1.

Introduction

The harmonic oscillator is among the most important models in physics. Its most tangible realization are undoubtedly macroscopic mechanical resonators such as masses on springs, suspended membranes or doubly-clamped beams. The field of optomechanics studies the interaction between electromagnetic and mechanical modes and provides the ideal toolkit for the read-out of their motion [1]. To this end, one can couple the mechanical resonator either to optical modes at THz frequencies confined in optical cavities or to microwave modes at GHz frequencies propagating in electrical circuits. While the first approach is known as cavity optomechanics, the latter is commonly called cavity electromechanics. These approaches allow for measuring the displacement of mechanical resonators with masses ranging from several kilograms to a few picograms with record high sensitivities [2, 3, 4, 5, 6]. Besides the detection of mechanical motion, optomechanics opens the way towards investigating mechanical resonators in the quantum regime [1, 7]. An indispensable prerequisite for doing so is the ability to cool the mechanical component to its quantum ground state that has been demonstrated in both the optical [8] and the microwave domain [9]. Once this is achieved, quantum mechanical effects can be observed. These include the hybridization of mechanical and electromagnetic modes [10, 11] as well as the coherent exchange of excitations between them [12, 13]. Furthermore, the generation of entanglement between microwaves and mechanical motion [14] as well as between two mechanical resonators [15, 16] and squeezing of the mechanical state [17, 18, 19] were realized. Even for quantum information processing with superconducting circuits, optomechanical devices might play a key role as they enable the conversion of quantum signals between the microwave regime, where the circuits typically operate, and the telecom band, which can be used for long range communication [20]. All of the above mentioned experiments can be described within the linearized approximation of the optomechanical Hamiltonian. In order to harness the full nonlinearity of this interaction, the single-photon strong coupling regime needs to be reached, in which novel quantum mechanical effects, such as the generation of non-classical mechanical states, are predicted to become experimentally accessible [1, 21, 22]. A potential pathway towards single-photon strong coupling are inductively coupled electromechanical devices in which the mechanical motion is transduced to a change in the inductance of a microwave cavity. This novel class of devices has long been predicted to allow for larger vacuum coupling rates than the previous capacitive coupling schemes [23, 24, 25, 26]. Recently, several realizations of inductive coupling have been demonstrated experimentally [27, 28, 29, 30]. While the demonstrated coupling rates did exceed what was previously possible, all of the presented devices still operate outside of the single-photon strong coupling regime.

In this thesis, we report on efforts towards realizing single-photon strong coupling by fabricating a nano-electromechanical device consisting of a superconducting microwave resonator shunted to ground by a dc SQUID with embedded mechanically compliant nanostrings. Our device is inspired by the one in Ref. [28], however we aim for enhanced internal quality factors of the microwave resonator and therefore resort to a more sophisticated fabrication process. Moreover, we investigate the mechanical frequency shift of a nanostring embedded into a SQUID, based on the work done in Ref. [31]. Specifically, we focus on the shift of the uncoupled frequency of the nanostring and consider the creation of flux lines inside the nanostring that couple to the mechanical motion as a possible cause of this unexpected frequency shift.

This thesis is structured as follows. In Chap. 2, we provide the theoretical background necessary for understanding the experimental work of this thesis. Chap. 3 presents the layout of our device. We introduce the experimental methods in Chap. 4, which includes an overview of the fabrication of flux-tunable resonators as well as the experimental setup. The next two chapters present the experimental results of this work. In Chap. 5, we describe the characterization of fixed-frequency and flux-tunable CPW resonators and Chap. 6 is dedicated to the investigation of the above mentioned mechanical frequency shift of a nanostring. Finally, we conclude the thesis with a summary and an outlook on possible future directions building on the presented results.

Chapter 2.

Theory

This chapter presents the theoretical background necessary to understand the experimental results of this work. Section 2.1 introduces the optomechanical Hamiltonian that describes the interaction of an electromagnetic with a mechanical mode. In this section, we touch upon the full nonlinear Hamiltonian, its linearized approximation and the single-photon strong coupling regime. Next, we introduce important elements of superconducting quantum circuits in Sec. 2.2, namely coplanar waveguide microwave resonators (Sec. 2.2.1), the Josephson junction (Sec. 2.2.2) and the dc-SQUID (Sec. 2.2.3). A coplanar waveguide resonator shunted to ground by a dc-SQUID constitutes a flux-tunable resonator, to which Sec. 2.2.4 is dedicated. These flux-tunable resonators allow for building nano-electromechanical devices via an inductive coupling scheme which we explain in Sec. 2.3. One implementation of such an inductively coupled nano-electromechanical device is a flux-tunable resonator featuring a mechanically compliant string integrated into its SQUID. Sec. 2.4 treats the mechanical aspects of a SQUID with a mechanically compliant string. In Sec. 2.4.1, we present models for the shift of the mechanical frequency induced by the Lorentz force and in Sec. 2.4.2, we discuss the experimentally observed residual shift of the uncoupled mechanical frequency that might be attributed to the coupling between mechanical motion and flux lines.

2.1. The optomechanical Hamiltonian

Opto- and electromechanical systems widely differ in terms of the masses and frequencies of the mechanical elements, the cavity frequencies and the overall implementation of the mechanical and electromagnetic resonators and their interaction [32, 1]. Nevertheless, all opto- and electromechanical systems can be described by the same Hamiltonian, known as the optomechanical Hamiltonian, which in general leads to coupled nonlinear equations of motion [1]. Here, we are first going to motivate this Hamiltonian, then look at its linearized form and finally summarize the conditions under which the system resides in the nonlinear regime and the effects predicted to emerge therein.

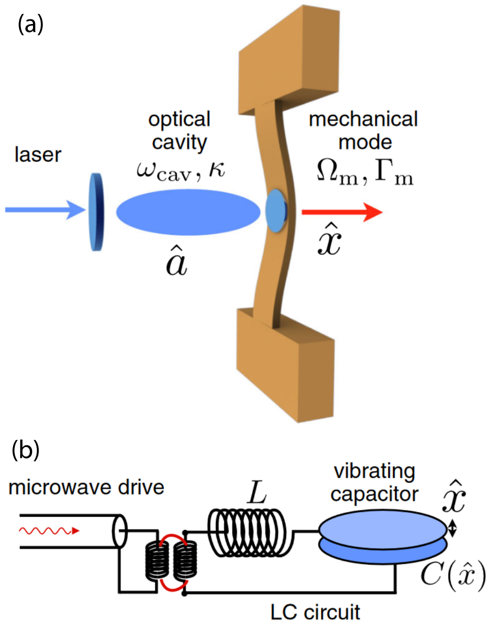

Figure 2.1.1.: (a) Schematic illustration of a typical optomechanical device consisting of a Fabry-Pérot cavity with a mechanically compliant end mirror. An optical mode of frequency ω_{cav} and decay rate κ couples to a mechanical mode of frequency Ω_{m} and damping rate Γ_{m} via the radiation pressure force. The cavity is driven by an external laser. (b) Schematic circuit diagram of a common electromechanical device, where the vibrations of a plate capacitor modulate its capacitance C and therefore the resonance frequency of a LC circuit. Concepts where the inductance L instead of the capacitance is modulated exist as well. The LC circuit is coupled to an external microwave drive. Taken from [1].

The nonlinear optomechanical Hamiltonian In order to obtain the most simple form of the optomechanical Hamiltonian, it suffices to take into account one electromagnetic mode of frequency ω_{cav} interacting with only one mechanical mode of frequency Ω_{m} [1]. Usually, the electromagnetic mode under consideration is the one closest to the frequency of the driving mode and the choice of the mechanical mode is arbitrary to a large extent. Schematics of standard opto- and electromechanical systems are shown in Fig. 2.1.1. Both the mechanical mode and the optical mode can be treated as harmonic oscillators, such that the uncoupled Hamiltonian $\hat{H}_0$ of the hybrid system reads

$$\hat{H}_0 = \hbar\omega_{\mathrm{cav}}\hat{a}^\dagger\hat{a} + \hbar\Omega_{\mathrm{m}}\hat{b}^\dagger\hat{b}, \tag{2.1}$$

where $\hat{a}^\dagger$ ($\hat{a}$) and $\hat{b}^\dagger$ ($\hat{b}$) are the creation (annihilation) operators of the optical and mechanical mode, respectively. The coupling between the two modes arises as the cavity frequency depends parametrically on the mechanical displacement x: $\omega_{\mathrm{cav}} = \omega_{\mathrm{cav}}(x)$. As a consequence, the mechanical motion modulates the resonance frequency of the cavity. As the mechanical displacement is usually very small, one can expand the change of the cavity frequency to first order as

$$\omega_{\mathrm{cav}}(x) \approx \omega_{\mathrm{cav}} + \frac{\partial\omega_{\mathrm{cav}}}{\partial x}x = \omega_{\mathrm{cav}} - Gx. \tag{2.2}$$

The minus sign in the definition $\partial\omega_{\mathrm{cav}}/\partial x = -G$ makes sense especially in the context of a Fabry-Pérot cavity with frequency $\omega_{\mathrm{cav}} = n\pi c/L$, where n is the integer mode number, c the speed of light and L the cavity length [1]. The mechanical displacement x is defined such that for $x > 0$ the cavity length increases and consequently, the cavity frequency decreases. As one would like to have positive coupling strengths, i.e. $G > 0$, it is convenient to introduce the minus sign. With this expansion, the interaction part of the Hamiltonian can be expressed as

$$\hat{H}_{\mathrm{int}} = -\hbar G \hat{a}^\dagger \hat{a} \hat{x} = -\hbar g_0 \hat{a}^\dagger \hat{a} (\hat{b} + \hat{b}^\dagger), \tag{2.3}$$

where $\hat{x} = x_0(\hat{b} + \hat{b}^\dagger)$ is the operator of mechanical displacement and $g_0 = Gx_0$ the vacuum optomechanical coupling rate, quantifying the interaction strength between a single phonon and a single photon [1]. The zero-point motion x_0 of the mechanical oscillator

$$x_0 = \sqrt{\frac{\hbar}{2m\Omega_{\mathrm{m}}}} \tag{2.4}$$

is its position uncertainty in the quantum mechanical ground state. Hence, the full Hamiltonian of the optomechanical system is given by

$$\hat{H} = \hat{H}_0 + \hat{H}_{\mathrm{int}} = \hbar\omega_{\mathrm{cav}} \hat{a}^\dagger \hat{a} + \hbar\Omega_{\mathrm{m}} \hat{b}^\dagger \hat{b} - \hbar g_0 \hat{a}^\dagger \hat{a} (\hat{b} + \hat{b}^\dagger). \tag{2.5}$$

Of course, one can include higher order terms in the expansion of the cavity resonance frequency in Eq. 2.2, which leads to an interaction term quadratic in the displacement operator [33]. However, the quadratic coupling is in most cases much smaller than the linear coupling, such that it is neglected in the Hamiltonian in Eq. 2.5. It is important to note that since the interaction part is cubic in operators, the equations of motion of the operators in the Heisenberg picture are quadratic in operators and therefore nonlinear. Usually, the cavity is driven by an external coherent driving field with Hamiltonian [1]

$$\hat{H}_{\mathrm{d}} = i\hbar\sqrt{\kappa_{\mathrm{ext}}}(\hat{a}^\dagger \, \alpha_{\mathrm{in}} e^{-i\omega_{\mathrm{L}} t} - \hat{a} \, \alpha_{\mathrm{in}}^* e^{i\omega_{\mathrm{L}} t}), \tag{2.6}$$

where ω_{L} is the frequency and α_{in} the amplitude of the driving field and κ_{ext} quantifies the coupling strength between drive and cavity field.

The linearized optomechanical Hamiltonian In most cases it is not necessary to keep the full nonlinear Hamiltonian for an appropriate description of the optomechanical system. Instead, one can resort to a linearized version of Eq. 2.5. This linearized optomechanical Hamiltonian is applicable whenever the average occupation of the cavity $\langle \hat{a} \rangle$ is much larger than the quantum fluctuation of the cavity field or when the decay rate κ of the cavity is large [1]. Then, one can decompose the cavity field as

$$\hat{a} = \langle \hat{a} \rangle + \delta\hat{a} = \alpha + \delta\hat{a}. \tag{2.7}$$

It is convenient to switch to a frame rotating a the drive frequency with the unitary transformation $\hat{U} = \exp\big(i\omega_{\mathrm{L}}\hat{a}^\dagger\hat{a}t\big)$. Then, the optomechanical Hamiltonian in Eq. 2.5 becomes

$$\hat{U}\hat{H}\hat{U}^\dagger - i\hbar\hat{U}\frac{\partial\hat{U}^\dagger}{\partial t} = -\hbar\Delta\hat{a}^\dagger\hat{a} + \hbar\Omega_{\mathrm{m}}\hat{b}^\dagger\hat{b} - \hbar g_0(\alpha + \delta\hat{a})^\dagger(\alpha + \delta\hat{a})(\hat{b} + \hat{b}^\dagger), \tag{2.8}$$

where we have inserted the decomposition Eq. 2.7 and $\Delta = \omega_{\mathrm{L}} - \omega_{\mathrm{cav}}$ is the detuning between the drive field and the cavity. The first term in the interaction part proportional to $|\alpha|^2$ is due to an average radiation pressure force that shifts the equilibrium position of the mechanical oscillator by δx. It can be omitted when accounting for this shift in the operators of the mechanics and replacing $\Delta + G\delta x \to \Delta$. The third term of the interaction proportional to $\delta\hat{a}^\dagger\delta\hat{a}$ is also typically neglected, as it is considered small compared to $\alpha\delta\hat{a}^\dagger$ and $\alpha^*\delta\hat{a}$. Then, only the term proportional to $(\alpha^*\delta\hat{a} + \alpha\delta\hat{a}^\dagger)$ remains. One can always assume α to be real, such that it is related to the mean photon number in the cavity $\bar{n}$ by $\alpha = \sqrt{\bar{n}}$. Finally, one arrives at the linearized optomechanical Hamiltonian

$$\hat{H}^{(\mathrm{lin})} = -\hbar\Delta\hat{a}^\dagger\hat{a} + \hbar\Omega_{\mathrm{m}}\hat{b}^\dagger\hat{b} - \hbar g_0\sqrt{\bar{n}}(\delta\hat{a}^\dagger + \delta\hat{a})(\hat{b} + \hat{b}^\dagger). \tag{2.9}$$

Importantly, the effective coupling strength between photons and phonons is no longer given by g_0 but by $g = g_0\sqrt{\bar{n}}$. This means that the effective coupling strength can be enhanced via the average number of photons in the cavity that is related to the input power of the drive.

Important milestones of cavity electromechanics were achieved with systems to which this linearized approximation applies [9, 11, 14]. When the mechanical frequency Ω_{m} by far exceeds the cavity linewidth κ, the system is said to be in the resolved-sideband regime. In this regime, the mechanical mode can be efficiently cooled to the quantum ground state for a detuning $\Delta = -\Omega_{\mathrm{m}}$ [34], which was demonstrated experimentally [9]. This can be understood as follows. For $\Delta = -\Omega_{\mathrm{m}}$, terms in the interaction part of the Hamiltonian that change the total number of quanta (that is $\delta\hat{a}\hat{b}$ and $\delta\hat{a}^\dagger\hat{b}^\dagger$) can be omitted as they are offresonant [1]. Then, the remaining interaction term reads $-\hbar g(\delta\hat{a}^\dagger\hat{b} + \delta\hat{a}\hat{b}^\dagger)$. The first term describes the creation of a photon at frequency ω_{cav} in the cavity mode and an annihilation of a phonon in the mechanics. This process is known as anti-Stokes Raman scattering [35] and gives rise to an anti-Stokes field blue detuned from the driving field by the mechanical frequency Ω_{m}. It is illustrated in Fig. 2.1.2 (a). The second term describes the opposite process: a photon annihilated in the cavity and

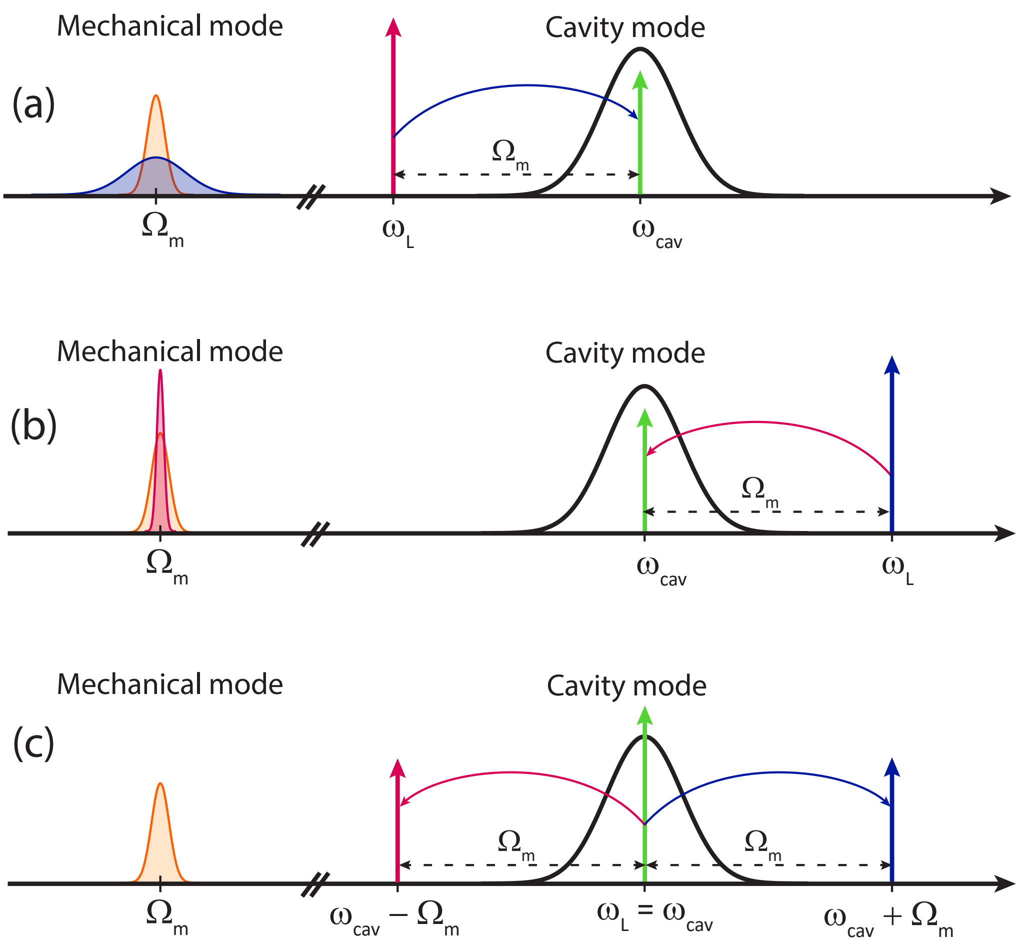

Figure 2.1.2.: Dominant scattering processes induced by the linearized optomechanical Hamiltonian for different detunings $\Delta = \omega_{\mathrm{L}} - \omega_{\mathrm{cav}}$ between the frequency of the driving field ω_{L} and the cavity frequency ω_{cav}. (a) When driving the cavity on the red sideband with $\Delta = -\Omega_{\mathrm{m}}$, the anti-Stokes Raman scattering process (blue arrow) that creates a photon at frequency ω_{cav} in the cavity and annihilates a phonon in the mechanics is enhanced as the cavity density of states is large at ω_{cav}, while the Stokes Raman scattering process is suppressed. This leads to cooling of the mechanical mode, indicated be the increased mechanical linewidth. (b) For a detuning of $\Delta = \Omega_{\mathrm{m}}$, the Stokes Raman scattering process (arrow in magenta) that creates a photon in the cavity and a phonon in the mechanics is enhanced, whereas the anti-Stokes Raman scattering is suppressed. Driving the cavity on the blue sideband thus results in heating of the mechanical mode as indicated by the reduced mechanical linewidth. (c) When driving the cavity on resonance ($\Delta = 0$), both scattering processes are equally likely as the cavity density of states is the same at $\omega_{\mathrm{cav}} - \Omega_{\mathrm{m}}$ and $\omega_{\mathrm{cav}} + \Omega_{\mathrm{m}}$. Therefore, neither cooling nor heating occur and Ω_{m} and Γ_{m} are not modified.

a creation of a phonon. As the cavity mode is in the vacuum state in the beginning, the transition rate for the first process exceeds that for the second one until equilibrium is reached. Thus, driving the cavity on the red sideband leads to an overall reduction of the number of excitations in the mechanics and therefore cooling. For a detuning of $\Delta = +\Omega_\mathrm{m}$, the dominant part of the interaction is given by $-\hbar g(\delta\hat{a}^\dagger\hat{b}^\dagger + \delta\hat{a}\hat{b})$, which describes a simultaneous creation or annihilation of an excitation in both the cavity and the mechanical mode. This process of Stokes Raman scattering [35] creates a Stokes field red detuned from the driving field by Ω_m and is illustrated in Fig. 2.1.2 (b). As a consequence, this causes a population of the mechanical mode which can be interpreted as heating. Driving the cavity on the blue sideband is an essential step in a protocol generating entanglement between the microwave field and the mechanical mode that was implemented in Ref. [14]. In general, the mechanical resonance frequency Ω_m as well as the mechanical damping rate Γ_m shift due to the interaction between the cavity field and the mechanics. This is a fundamental phenomenon in opto- and electromechanics known as backaction. Only when the cavity is driven on resonance ($\Delta = 0$) both Stokes and anti-Stokes fields are created at $\omega_\mathrm{cav} \pm \Omega_\mathrm{m}$ as illustrated in Fig. 2.1.2 (c) and there is no modification of Ω_m and Γ_m [1]. In order to avoid the backaction due to the optomechanical interaction, we choose $\Delta = 0$ in our experiments investigating the frequency shift of a nanostring integrated into a SQUID loop (see Sec. 4.2 and Chap. 6).

The single-photon strong coupling regime The fundamental limitation of the linearized Hamiltonian in Eq. 2.9 is that it converts Gaussian input states of the light field only to Gaussian states of the mechanics. Therefore, the generation of nonclassical mechanical states with negative Wigner density is not possible within this protocol. Nevertheless, such states might be created from nonclassical input states such as Fock states that can be transferred onto the mechanics by the linearized interaction [1].
In order to harness the nonlinearity of the full optomechanical Hamiltonian in Eq. 2.5, it is necessary to reach the single-photon strong coupling regime, where the vacuum optomechanical coupling rate exceeds the cavity decay rate:

$$\frac{g_0}{\kappa} > 1. \tag{2.10}$$

If this condition is met, a single phonon in the mechanical mode shifts the resonance frequency of the cavity by more than its linewidth [1]. To develop a better intuition for the single-photon strong coupling regime, one can consider the mechanical displacement δx caused by a single photon in the cavity. It is given by [1, 36]

$$\frac{\delta x}{x_0} = 2\frac{g_0}{\Omega_\mathrm{m}}. \tag{2.11}$$

For nonlinear effects to be observable, the device needs to reside in the resolved-sideband regime $\Omega_{\mathrm{m}} \gg \kappa$ [1]. In the single-photon strong coupling regime, a single photon then displaces the equilibrium position of the mechanics by more than the zero point motion x_0 if $g_0 > \Omega_{\mathrm{m}}$ [1, 21, 36]. In this regime, interesting quantum effects are predicted to emerge that are qualitatively different from the ones observable for $g_0 < \kappa$. These include the generation of nonclassical mechanical states with negative Wigner density [22] and the phenomenon of photon blockade, where the presence of a single photon prevents a second photon from entering the cavity [21]. Experiments that come close to the single-photon strong coupling regime have been performed on systems with clouds of ultracold atoms inside optical cavities [37, 38]. However, these systems did not reside in the resolved-sideband regime that has been demonstrated in several opto- and electromechanical systems by now [8, 9, 28]. To date, there is no experimental realization of the single-photon strong coupling regime in opto- and electromechanical systems.

2.2. Superconducting quantum circuits

2.2.1. Coplanar waveguide microwave resonators

Microwave resonators constitute essential building blocks in nano-electromechanical systems and can be implemented in different ways. One such implementation are two-dimensional superconducting coplanar waveguide (CPW) resonators that consist of a center conductor of width w that is separated from a ground plane by gaps of width s. The structure is sustained by a substrate with relative permittivity ϵ_{r}. A sketch of the cross-section of a CPW resonator is shown in Fig. 2.2.1. In the fabrication of our devices, we pattern CPW resonators into superconducting niobium (Nb) thin films on top of a silicon (Si) substrate with $\epsilon_{\mathrm{r}} = 11.9$ [39].

The CPW resonator supports only standing waves of the electromagnetic field with frequencies close to its resonance frequency due to boundary conditions at its ends. There are two different types of boundary conditions: an open boundary condition in the form of a capacitor where the current vanishes and the voltage is maximal and a short to ground where the current is maximal and the voltage vanishes [40]. One open boundary and one short to ground result in a $\lambda/4$-resonator, whereas a $\lambda/2$-resonator is made by introducing two open ends. In this work, we always investigate $\lambda/4$-resonators that are capacitively coupled to a microwave feedline as shown in Fig. 2.2.1 (b), which allows for driving the resonator by sending microwave signals through the feedline. At low temperatures and low excitation powers, the quantized nature of the electromagnetic field inside the CPW resonator becomes important and each of its modes needs to be described as a quantum mechanical harmonic oscillator [40].

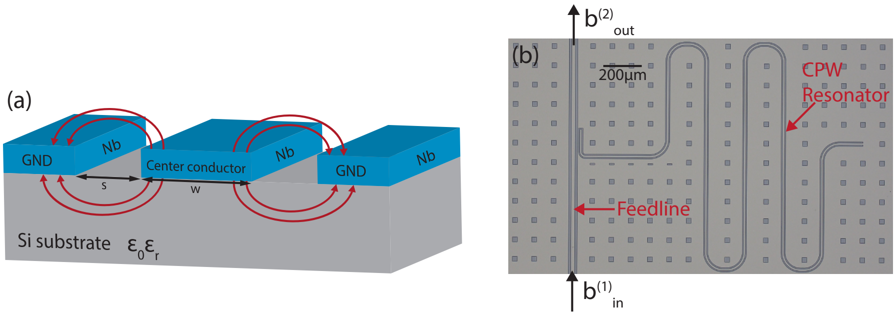

Figure 2.2.1.: (a) Sketch of the cross-section of a CPW resonator that consists of a center conductor of width w separated from a ground plane by a gap of width s. The center conductor and ground plane are made of a superconducting material such as niobium (Nb). The CPW resonator is sustained by a silicon (Si) substrate with permittivity $\epsilon_0\epsilon_\mathrm{r}$. The red arrows indicate the electric field of a electromagnetic mode propagating in the resonator. (b) Top view of a $\lambda/4$ CPW resonator capacitively coupled to a microwave feedline. The input field at port 1 is denoted by $b_\mathrm{in}^{(1)}$ and the output field at port 2 by $b_\mathrm{out}^{(2)}$.

For $\lambda/4$-resonators, the frequency of the fundamental mode is given by [41]

$$\frac{\omega_0}{2\pi} = \frac{c}{\sqrt{\epsilon_\mathrm{eff}}}\frac{1}{4l} = \frac{v}{4l}, \tag{2.12}$$

where c is the speed of light in vacuum, ϵ_eff the effective permittivity, v the phase velocity and l the resonator's length. The phase velocity can also be expressed as $v = 1/\sqrt{L_0 C_0}$, where L_0 (C_0) is the inductance (capacitance) of the CPW per unit length. Neglecting kinetic inductance, L_0 depends only on the geometry of the CPW and C_0 is always entirely determined by the geometry as well as the effective permittivity ϵ_eff via [41]

$$L_0 = \frac{\mu_0}{4}\frac{K(k_0^{'})}{K(k_0)} \quad \text{and} \quad C_0 = 4\epsilon_0\epsilon_\mathrm{eff}\frac{K(k_0)}{K(k_0^{'})}, \tag{2.13}$$

where K is the complete elliptic integral of the first kind with geometry-dependent arguments. Furthermore,

$$k_0 = \frac{w}{w+2s} \quad \text{and} \quad k_0^{'} = \sqrt{1-k_0^2}. \tag{2.14}$$

As we deal with CPWs made of superconducting material, the resistance can initially be assumed negligible [1] [40] and the characteristic impedance Z_0 is given by [41]

$$Z_0 = \sqrt{\frac{L_0}{C_0}}. \tag{2.15}$$

[1]There exists a surface impedance which contributes to the internal quality factor of the resonator [42].

In order to minimize reflections of incoming microwave signals, the characteristic impedance of the CPW must be designed to $50\,\Omega$, which is achieved for $w = 10\,\mu\mathrm{m}$ and $s = 6\,\mu\mathrm{m}$ in our case.

An important figure of merit of oscillators in general and microwave resonators in particular is the quality factor Q. There are different equivalent definitions of Q, one of which is [43, 1]

$$Q = 2\pi \frac{\langle E \rangle}{\Delta E} = \frac{\omega_0}{\kappa}. \tag{2.16}$$

Here, $\langle E \rangle$ denotes the average energy stored inside the resonator, ΔE is the energy loss per period and κ the total loss rate. The total loss rate can be divided into a contribution κ_{int} due to internal losses and a contribution κ_{ext} due to losses to the microwave feedline to which the CPW resonator is coupled: $\kappa = \kappa_{\mathrm{int}} + \kappa_{\mathrm{ext}}$. The inverses of the corresponding quality factors add up and yield the total quality factor

$$\frac{1}{Q} = \frac{1}{Q_{\mathrm{int}}} + \frac{1}{Q_{\mathrm{ext}}}. \tag{2.17}$$

In real devices, one usually aims for internal quality factors as high as possible, or equivalently, internal losses as low as possible. In superconducting circuits, there are different sources of internal losses such as two-level systems (TLS), quasiparticles, vortices or parasitic modes [44]. The external quality factor in contrast determines the coupling strength to the microwave feedline (the lower Q_{ext}, the stronger the coupling) and can be adjusted via the geometry of the device. A resonator with $Q_{\mathrm{int}} > Q_{\mathrm{ext}}$ ($Q_{\mathrm{int}} < Q_{\mathrm{ext}}$) is called overcoupled (undercoupled), as the rate of absorption of photons inside the resonator is smaller (larger) than the transition rate of photons between cavity and feedline. In the special case of $Q_{\mathrm{int}} = Q_{\mathrm{ext}}$, the resonator is said to be critically coupled.

Scattering parameter for a CPW resonator capacitively coupled to a feedline We are now going to sketch the derivation of the S_{21} scattering parameter for a CPW resonator capacitively coupled to a feedline. Such a system is shown in Fig. 2.2.1 (b). The S_{21} parameter is defined as the ratio of the output field at port 2 to the input field at port 1:

$$S_{21} = \frac{b_{\mathrm{out}}^{(2)}}{b_{\mathrm{in}}^{(1)}}. \tag{2.18}$$

In order to derive this quantity, we make use of input-output theory that allows for a quantum mechanical description of a cavity coherently driven by external electromagnetic modes and closely follow Refs. [45, 46]. As already mentioned, each eigenmode of the CPW resonator is described by a quantum harmonic oscillator. Here, we focus on the fundamental mode with angular frequency ω_{cav}, as that is usually the mode one measures in experiments. Of course, the corresponding Hamiltonian is given by

$$\hat{H}_{\text{cav}} = \hbar\omega_{\text{cav}}\Big(\hat{a}^\dagger\hat{a} + \frac{1}{2}\Big), \tag{2.19}$$

where $\hat{a}^\dagger$ ($\hat{a}$) is the creation (annihilation) operator of the fundamental mode. The external field used to drive the resonator is modeled as a bath of modes with Hamiltonian

$$\hat{H}_{\text{bath}} = \int d\omega\, \hbar\omega\, \hat{b}^\dagger(\omega)\hat{b}(\omega), \tag{2.20}$$

where the integration over angular frequencies ranges from $-\infty$ to $+\infty$. In the picture of a CPW resonator coupled to a feedline, these modes propagate in the feedline. Lastly, the coupling of the modes in the feedline to the mode of the resonator is accounted for by an interaction Hamiltonian that one commonly assumes to be linear in $\hat{b}^\dagger$ and $\hat{b}$. It is of the form

$$\hat{H}_{\text{int}} = i\hbar \int d\omega\, g\, \big[\hat{b}^\dagger(\omega)\hat{a} - \hat{a}^\dagger\hat{b}(\omega)\big], \tag{2.21}$$

where we assume the coupling constant g to be independent of frequency. The full Hamiltonian of the system is then given by

$$\hat{H} = \hat{H}_{\text{cav}} + \hat{H}_{\text{bath}} + \hat{H}_{\text{int}}. \tag{2.22}$$

In the Heisenberg picture, we obtain the following equations of motions for the annihilation operators $b(\omega)$ of the external modes and a of the cavity mode

$$\dot{b}(\omega) = \frac{1}{i\hbar}[b(\omega), H] = -i\omega b(\omega) + g\, a \tag{2.23}$$

$$\dot{a} = \frac{1}{i\hbar}[a, H] = -i\omega_{\text{cav}} a - \int d\omega\, g\, b(\omega), \tag{2.24}$$

where we have dropped the hats above the operators for convenience and used the usual commutation relations of the operators $[a, a^\dagger] = 1$ and $[b(\omega), b(\omega')^\dagger] = \delta(\omega - \omega')$. One can immediately write down the solution of the equation of motion for b. It is given by

$$b(\omega) = b_0(\omega)\, e^{-i\omega(t-t_0)} + g \int_{t_0}^{t} dt'\, e^{-i\omega(t-t')} a(t'), \tag{2.25}$$

where we omit the dependence of $b(\omega)$ on t and $b_0(\omega)$ is the annihilation operator at t_0, where both $t_0 < t$ and $t_0 > t$ are allowed. We can now plug this solution for $t_0 < t$ into the equation of motion for the cavity mode and redefine g in terms of the transition rate of a photon between cavity and bath κ_{ext} as $g = \sqrt{\kappa_{\text{ext}}/(2\pi)}$. Furthermore, we define the input field as

$$b_{\text{in}}(t) = \frac{1}{\sqrt{2\pi}} \int d\omega\, e^{i\omega(t-t_0)} b_0(\omega). \tag{2.26}$$

The second term on the right hand side of Eq. 2.24 then describes the temporal evolution of the cavity mode due to the exchange of photons with the bath:

$$\dot{a}\big|_{\text{ext}} = -\sqrt{\kappa_{\text{ext}}} b_{\text{in}}(t) - \frac{\kappa_{\text{ext}}}{2} a. \tag{2.27}$$

So far, the model does not account for internal damping of the cavity mode, such that we need to put in this term by hand:

$$\dot{a}\big|_{\text{int}} = -\frac{\kappa_{\text{int}}}{2} a, \tag{2.28}$$

where κ_{int} is the internal damping rate. In the same way, one can define an output field for $t_0 > t$ and plug the solution of Eq. 2.23 for $t_0 > t$ into Eq. 2.24. This way, one can express the equation of motion for the resonator field in terms of b_{in} or b_{out}:

$$\dot{a} = -i\omega_{\text{cav}} a - \left(\frac{\kappa_{\text{int}}}{2} - \frac{\kappa_{\text{ext}}}{2}\right) a - \sqrt{\kappa_{\text{ext}}} b_{\text{out}}(t) \tag{2.29}$$

$$\dot{a} = -i\omega_{\text{cav}} a - \left(\frac{\kappa_{\text{int}}}{2} + \frac{\kappa_{\text{ext}}}{2}\right) a - \sqrt{\kappa_{\text{ext}}} b_{\text{in}}(t) \tag{2.30}$$

Subtraction of these two equations yields the following boundary condition:

$$b_{\text{out}} = b_{\text{in}} + \sqrt{\kappa_{\text{ext}}} a. \tag{2.31}$$

As we measure the CPW resonator in transmission, an important subtlety arises. The part of the cavity mode that couples back into the feedline has two possible directions of propagation: towards port 1 or towards port 2. For this reason, a factor of 1/2 needs to be taken into account and the actual boundary condition reads

$$b_{\text{out}}^{(2)} = b_{\text{in}}^{(1)} + \frac{1}{2}\sqrt{\kappa_{\text{ext}}} a. \tag{2.32}$$

We now switch to Fourier space, such that the equation of motion Eq. 2.30 becomes algebraic and we can solve it for a. This yields

$$a = -\frac{\sqrt{\kappa_{\text{ext}}}}{i(\omega_{\text{cav}} - \omega) + \frac{\kappa}{2}} b_{\text{in}}. \tag{2.33}$$

This expression for a allows us to connect the average number of photons in the cavity $\langle a^\dagger a \rangle$ to the input power $P = \hbar\omega \langle b_{\text{in}}^\dagger b_{\text{in}} \rangle$. At resonance (i.e. $\omega = \omega_{\text{cav}}$), the average cavity

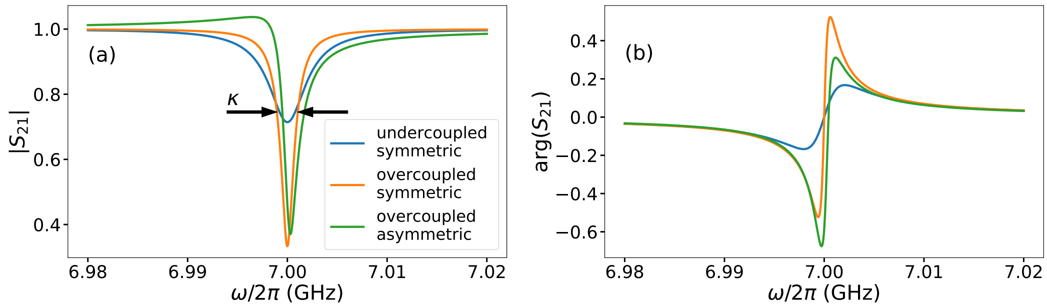

Figure 2.2.2.: (a) The absolute value of the S_{21} parameter given in Eq. 2.35 for both an undercoupled (blue) and overcoupled resonator (orange and green). The full width half maximum κ of $1 - |S_{21}|$ is indicated for the transmission in orange. For $\phi \neq 0$, the transmission becomes asymmetric. We have taken the following quality factors for the transmission spectra: $Q_{\text{int}} = 2 \times 10^3$, $Q_{\text{ext}} = 5 \times 10^3$ for the undercoupled resonator and $Q_{\text{int}} = 10^5$, $Q_{\text{ext}} = 5 \times 10^3$ for the overcoupled resonators. For the asymmetric transmission $\phi = \pi/8$. (b) The corresponding phases of the transmission spectra shown in (a).

occupation is given by

$$\langle a^\dagger a \rangle = \frac{4\kappa_{\text{ext}}}{\kappa^2} \frac{P}{\hbar\omega_{\text{cav}}}. \tag{2.34}$$

In order to derive an expression for the complex S_{21} scattering parameter, we plug the solution for a from Eq. 2.33 into the boundary condition Eq. 2.32 and arrive at

$$S_{21} = 1 - \frac{\kappa_{\text{ext}}}{\kappa + i(\omega - \omega_{\text{cav}})} = 1 - \frac{\frac{Q}{Q_{\text{ext}}}}{1 + 2iQ\frac{\omega - \omega_{\text{cav}}}{\omega_{\text{cav}}}}, \tag{2.35}$$

where $Q = \omega_{\text{cav}}/\kappa$ and $Q_{\text{ext}} = \omega_{\text{cav}}/\kappa_{\text{ext}}$ are the total and external quality factor, respectively (cf. Eq. 2.16). In order to incorporate a possible mismatch between the input and output impedances at the two ports, one can include a complex external quality factor $Q_{\text{ext}} = |Q_{\text{ext}}|e^{-i\phi}$ that leads to a deviation of the resonance dip from the symmetric Lorentzian lineshape [47]. The absolute value and the phase of the S_{21} scattering parameter given in Eq. 2.35 is shown in Fig. 2.2.2 for different resonator parameters.

Finally, one needs to include contributions to the transmitted signal from outside the sample. The main external sources are due to the finite length of the cables, the finite speed of light and the attenuation of the signal in the cables. They lead to an offset phase α, a phase shift proportional to the excitation frequency that is parametrized by the cable delay τ and an amplitude a that accounts for the attenuation [47]. The total S_{21} scattering parameter therefore reads

$$S_{21} = ae^{i\alpha}e^{-i\omega\tau}\left[1 - \frac{\frac{Q}{|Q_{\text{ext}}|}e^{i\phi}}{1 + 2iQ\frac{\omega - \omega_{\text{cav}}}{\omega_{\text{cav}}}}\right]. \tag{2.36}$$

We use this model for fitting the experimental complex valued S_{21} data of our resonators in order to extract their resonance frequencies and quality factors.

Kerr nonlinearity In our device presented in Chap. 3, we implement the microwave cavity as a flux-tunable resonator (cf. Sec. 2.2.4) containing a SQUID. For such a cavity, the model of a harmonic oscillator with Hamiltonian given in Eq. 2.19 is only a good approximation at sufficiently low input powers. When applying higher input powers, the nonlinear SQUID potential (cf. Sec. 2.2.3) gives rise to nonlinear behavior described by the Hamiltonian [24, 48]

$$\hat{H}_{\mathrm{cav}} = \hbar\omega_{\mathrm{cav}}\hat{a}^\dagger\hat{a} + \frac{\hbar\mathcal{K}}{2}\hat{a}^\dagger\hat{a}^\dagger\hat{a}\hat{a}, \tag{2.37}$$

where the Kerr constant $\mathcal{K}$ quantifies the nonlinearity of the cavity. It can be understood as a shift of the cavity's resonance frequency per photon. For this reason, the nonlinearity becomes evident only for an appreciable occupation of the cavity. In the case of flux-tunable resonators, the resonance frequency decreases with increasing cavity occupation, i.e. $\mathcal{K} < 0$. Naturally, the derivation of the S_{21} parameter for a nonlinear cavity is much more involved than the above presented case of a linear cavity. Nevertheless, we mention that apart from the frequency shift, the Kerr nonlinearity leads to an asymmetric transmission spectrum around the resonance frequency and to bistable behavior for sufficiently large excitation levels [48].

2.2.2. The Josephson junction

A Josephson junction is an important element in superconducting quantum circuits that provides the nonlinearity necessary for superconducting qubits and is part of a SQUID that we introduce in the next section. When two superconductors are weakly coupled to form a Josephson junction, Cooper pairs can coherently tunnel from one superconductor to the other, which is known as the Josephson effect [49]. A sketch of a Josephson junction is shown in Fig. 2.2.3 (a).

The wavefunction $\Psi = |\Psi|e^{i\theta}$ of a superconductor is a macroscopic entity that describes the whole condensate of Cooper pairs. It is described by its modulus $|\Psi|$ that is related to the density n of Cooper pairs via $n = |\Psi|^2$ and its phase θ whose time derivative is related to the energy of the condensate [50]. One way of establishing a weak link between two superconductors are insulating tunnel barriers sufficiently thin to enable the overlap of superconducting states in the leads. For a small but finite overlap, a supercurrent I_{s} of Cooper pairs flows across the barrier. This phenomenon is described by the first Josephson equation:

$$I_{\mathrm{s}} = I_{\mathrm{c}}\sin(\varphi), \tag{2.38}$$

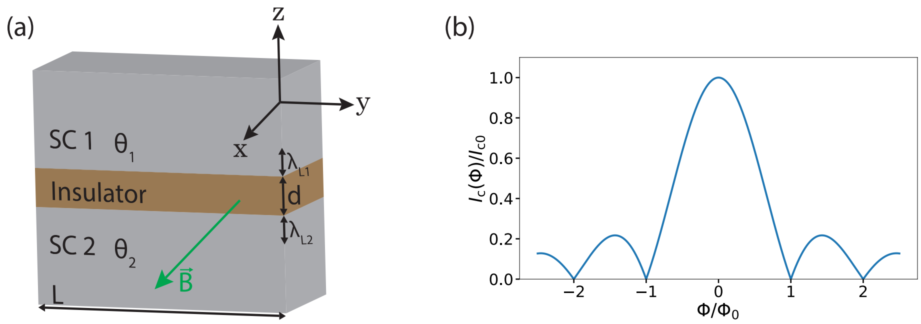

Figure 2.2.3.: (a) Sketch of a Josephson junction that consists of two superconductors (SC 1 and SC 2) with superconducting phases θ_1 and θ_2 that are weakly coupled by an insulating barrier of thickness d. If a finite magnetic field $\vec{B}$ is applied along the x-direction, the critical current modulates with the flux $\Phi = BLt_B$ according to Eq. 2.42. This equation is shown as a function of normalized flux Φ/Φ_0 in (b).

where the critical current I_c is the maximal supercurrent that can flow across the junction and $\varphi = \theta_2 - \theta_1$ is the difference of superconducting phases. If one forces a current larger than I_c across the junction, a part of this current will be carried by quasiparticles and a voltage drop V occurs across the junction due to the dissipative nature of the quasiparticle current. The voltage V governs the temporal evolution of the phase difference via the second Josephson equation:

$$\frac{\partial \varphi}{\partial t} = \frac{2\pi}{\Phi_0} V, \tag{2.39}$$

where we have introduced the flux quantum $\Phi_0 = h/(2\mathrm{e})$. An immediate consequence of the Josephson equations is that a nonlinear inductance, the Josephson inductance L_J, can be associated with a Josephson junction. It is easily obtained from taking the time derivative of the first Josephson equation, inserting the second Josephson equation and making use of the definition of an inductance $V = L\dot{I}$

$$L_\mathrm{J} = \frac{\Phi_0}{2\pi I_\mathrm{c} \cos(\varphi)}. \tag{2.40}$$

Here, the $1/\cos(\varphi)$ term shows the nonlinearity of the inductance. As an inductance is a dissipationless circuit element, one can calculate the energy stored in the Josephson junction as [51]

$$U = \int_{t_0}^{t} V I d\tau = \frac{\Phi_0 I_\mathrm{c}}{2\pi} \int_{t_0}^{t} \sin(\varphi) \frac{\partial \varphi}{\partial \tau} d\tau = E_\mathrm{J}(1 - \cos(\varphi)), \tag{2.41}$$

where we have chosen t_0 such that $\varphi(t_0) = 0$. The characteristic energy $E_\mathrm{J} = \Phi_0 I_\mathrm{c}/2\pi$ that sets the scale of this potential energy is called the Josephson energy. We see that the potential energy of a Josephson junction is nonlinear due to the $\cos(\varphi)$ term. This nonlinearity (together with its negligible dissipation) makes the Josephson junction an essential component of superconducting qubits as it lifts the degeneracy of the energy level spacing [51, 52].

If an external magnetic field B is applied in the plane of the junction (in Fig. 2.2.3 (a) B points along the x-direction), the phase difference and therefore the supercurrent depend on B. For the critical current, one finds the relation [50]

$$I_\mathrm{c}(\Phi) = I_\mathrm{c0}\left|\frac{\sin\frac{\pi\Phi}{\Phi_0}}{\frac{\pi\Phi}{\Phi_0}}\right|, \tag{2.42}$$

where I_c0 is the critical current in the absence of magnetic fields. The magnetic flux that enters this equation is given by $\Phi = BLt_B$, where L is the length of the junction and t_B a magnetic thickness defined by $t_B = d+\lambda_\mathrm{L1}+\lambda_\mathrm{L2}$. We see that apart from the thickness d of the insulating barrier, one needs to take into account the London penetration depths λ_L1 and λ_L2 which are characteristic length scales for each superconducting material. The reason is that the magnetic field penetrates the superconducting electrodes only on a length scale set by the penetration depth and decreases exponentially for increasing distance from the interface. The dependence on magnetic flux of the critical current thus equals a Fraunhofer diffraction pattern of a slit of width L [50]. The normalized critical current is shown in Fig. 2.2.3 (b).

2.2.3. The dc-SQUID

A direct-current superconducting quantum interference device (dc-SQUID) consists of two Josephson junctions that are integrated in parallel in a closed loop of superconducting material. A sketch of such a SQUID is shown in Fig. 2.2.4 (a). The total supercurrent flowing through the SQUID is the sum of the two supercurrents flowing through its arms. For a symmetric SQUID (i.e. identical junctions with identical critical currents I_c), it is given by

$$I_\mathrm{s}^\mathrm{SQUID} = I_\mathrm{c}(\sin(\varphi_1)+\sin(\varphi_2)) = 2I_\mathrm{c}\cos(\varphi_-)\sin(\varphi_+), \tag{2.43}$$

where φ_1 (φ_2) is the phase across the first (second) junction and we have introduced the sum and the difference of the phases $\varphi_\pm = (\varphi_2 \pm \varphi_1)/2$. The difference of phases φ_- is fixed by the total flux Φ threading the SQUID loop via [50]

$$\varphi_- = \pi\frac{\Phi}{\Phi_0}. \tag{2.44}$$

In general, there are two contributions to the total flux, which are the bias flux Φ_b that is due to an external magnetic field and the induced flux $L_\mathrm{loop}J$ that is due to a finite

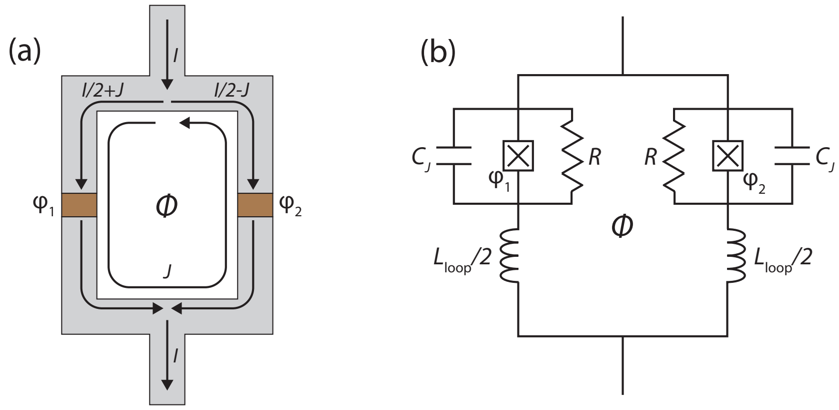

Figure 2.2.4.: (a) Sketch of a dc-SQUID with two Josephson junctions symmetrically incorporated into the SQUID loop. The phases across the junctions are denoted by φ_1 and φ_2. I is the total current flowing through the SQUID with $I/2 \pm J$ the components flowing through the left (right) branch, where J is the circulating current. The total flux threading the SQUID loop is given by Φ. (b) Equivalent circuit of a dc-SQUID where each Josephson junction consists of an ideal junction (represented by a cross), a resistance R and a capacitance C_J. Furthermore, the finite loop inductance L_loop symmetrically distributed over both arms is taken into account.

loop inductance L_loop and circulating currents J [53]

$$\Phi = \Phi_\mathrm{b} + L_\mathrm{loop} J = \Phi_\mathrm{b} + \frac{\beta_L j}{2}\Phi_0. \tag{2.45}$$

Here, $j = J/I_\mathrm{c}$ is the normalized circulating current and we have introduced the screening parameter $\beta_L = 2L_\mathrm{loop}I_\mathrm{c}/\Phi_0$ [54] that is a measure for the maximal magnetic flux $L_\mathrm{loop}I_\mathrm{c}$ the SQUID loop can screen in relation to half a flux quantum $\Phi_0/2$. Only in the limit $\beta_L \ll 1$, the self induced flux is negligible and $\Phi \simeq \Phi_\mathrm{b}$. Then, the critical current of the SQUID, which is the maximal value of the supercurrent in Eq. 2.43, is simply expressed as

$$I_\mathrm{c}^\mathrm{SQUID} = 2I_\mathrm{c}\cos\Big(\pi\frac{\Phi_\mathrm{b}}{\Phi_0}\Big). \tag{2.46}$$

We see that in this case, the SQUID behaves like a Josephson junction with a flux-tunable critical current, where φ_+ plays the role of the phase difference in a single junction. As for a single junction, we can define an inductance L_S of the SQUID as [55]

$$L_\mathrm{S} = \frac{\Phi_0}{4\pi I_\mathrm{c}\Big|\cos\Big(\frac{\pi\Phi_\mathrm{b}}{\Phi_0}\Big)\Big|} \tag{2.47}$$

that depends on the bias flux Φ_b. For finite β_L, the critical current has to be found by maximizing Eq. 2.43 with respect to φ_+ and φ_-, while fulfilling the constraint given by Eq. 2.44 [56]. In general, this cannot be done analytically.

We now turn our attention to the currents flowing through the two Josephson junctions. Of course, they are given by $I_{1/2} = I/2 \pm J$ (see Fig. 2.2.4 (a)), where I is the total current through the SQUID and J the circulating current. In general, not only a supercurrent carried by Cooper pairs contributes to the current through a junction, but also a quasiparticle current and a displacement current need to be taken into account [53]. Therefore, a SQUID behaves like the equivalent circuit shown in Fig. 2.2.4 (b). Each junction consists of an ideal junction that admits only a supercurrent, a capacitance C_J that allows for displacement currents and a resistance R through which a quasiparticle current can flow. For identical junctions, the total currents through the junctions are given by

$$\frac{I}{2} \pm J = I_\mathrm{c} \sin\bigl(\varphi_{1/2}\bigr) + \frac{V_{1/2}}{R} + C_\mathrm{J}\dot{V}_{1/2} = I_\mathrm{c} \sin\bigl(\varphi_{1/2}\bigr) + \frac{\Phi_0}{2\pi R}\dot{\varphi}_{1/2} + \frac{\Phi_0}{2\pi} C_\mathrm{J}\ddot{\varphi}_{1/2}, \quad (2.48)$$

where V_1 (V_2) is the voltage across the first (second) Josephson junction and we have made use of the second Josephson equation Eq. 2.39 in the second equality. We see that in the steady state case ($\dot{\varphi}_1 = \dot{\varphi}_2 = 0$) the total current is given by the supercurrent Eq. 2.43, whereas the circulating current reads

$$J = \frac{I_\mathrm{c}}{2}(\sin(\varphi_1) - \sin(\varphi_2)) = -I_\mathrm{c} \sin(\varphi_-) \cos(\varphi_+). \quad (2.49)$$

It is instructive to rewrite Eq. 2.48 in dimensionless units by normalizing currents to I_c and expressing dimensionless time as $\tau = \omega_\mathrm{c} t$. Here, $\omega_\mathrm{c} = (2\pi I_\mathrm{c} R)/\Phi_0$ is the characteristic frequency of the Josephson junctions [53]. It is the Josephson frequency at the characteristic voltage $I_\mathrm{c}R$. This results in

$$\dot{\varphi}_{1/2} + \beta_\mathrm{c}\ddot{\varphi}_{1/2} = \frac{i}{2} \pm j - \sin\bigl(\varphi_{1/2}\bigr) = \frac{i}{2} - \sin\bigl(\varphi_{1/2}\bigr) \pm \frac{2}{\pi\beta_L}\Bigl(\varphi_- - \pi\frac{\Phi_\mathrm{b}}{\Phi_0}\Bigr), \quad (2.50)$$

where $i = I/I_\mathrm{c}$ and $\beta_c = (2\pi I_\mathrm{c} R^2 C)/\Phi_0$ is called the Stewart-McCumber parameter [53]. In the last equality, we have rewritten j making use of Eq. 2.44 and 2.45. The above equation can be interpreted as the equation of motion of a phase particle moving in a two-dimensional potential U_SQUID given by [53]

$$U_\mathrm{SQUID} = E_\mathrm{J}\Bigl[\frac{2}{\pi\beta_L}\Bigl(\varphi_- - \pi\frac{\Phi_\mathrm{b}}{\Phi_0}\Bigr)^2 - 2\cos(\varphi_-)\cos(\varphi_+) - i\varphi_+\Bigr]. \quad (2.51)$$

The second term in the above equation is the sum of the energies stored in the two Josephson junctions (compare Eq. 2.41) and the first term can be rewritten with Eq. 2.44

and 2.45 as follows

$$\frac{2E_\mathrm{J}}{\pi\beta_L}\Big(\varphi_- - \pi\frac{\Phi_\mathrm{b}}{\Phi_0}\Big)^2 = E_\mathrm{J}\frac{\pi}{2}\beta_L\Big(\frac{J}{I_\mathrm{c}}\Big)^2 = \frac{L_\mathrm{loop}J^2}{2}, \tag{2.52}$$

such that it becomes apparent that it represents the inductive energy due to the circulating current J and the finite loop inductance L_loop. We note that the right hand side of Eq. 2.50 can be obtained via $-1/E_\mathrm{J}(\partial U_\mathrm{SQUID}/\partial\phi_{1/2})$. Therefore, it can be seen as the field of force in which the phase particle moves.
Finally, the Lagrangian of a SQUID is given by [57]

$$\mathcal{L}_\mathrm{S} = \Big(\frac{\Phi_0}{2\pi}\Big)^2 C_\mathrm{J}(\dot\varphi_+^2 + \dot\varphi_-^2) - U_\mathrm{SQUID} = \frac{\hbar^2}{2E_C}(\dot\varphi_+^2 + \dot\varphi_-^2) - U_\mathrm{SQUID}, \tag{2.53}$$

where $E_C = (2e)^2/(2C_\mathrm{J})$ is the typical capacitive energy of a Josephson junction.

2.2.4. Flux-tunable resonators

In this section, we introduce flux-tunable resonators (FTRs) that are essential building blocks for inductively coupled electromechanical devices. They usually contain a dc-SQUID with a flux-dependent inductance given by Eq. 2.47 that makes the resonance frequency of the FTR flux-tunable. First, we briefly touch upon flux-tunable lumped-element LC-resonators and then treat flux-tunable distributed-element resonators in more depth.

Flux tunable LC-resonators The resonance frequency of a lumped-elements LC-circuit is well known to be

$$\omega_\mathrm{c} = \frac{1}{\sqrt{LC}}, \tag{2.54}$$

where L and C are the inductance and capacitance of the circuit, respectively. For the circuit to be flux-tunable, it must contain a SQUID with an inductance of [26]

$$L_\mathrm{J} = \frac{\Phi_0}{4\pi I_0 S_0} = \frac{L_\mathrm{J0}}{S_0}. \tag{2.55}$$

Here, $S_0 = \sqrt{\cos^2(\pi\Phi/\Phi_0) + \alpha^2\sin^2(\pi\Phi/\Phi_0)}$ contains the flux dependence and α accounts for possibe asymmetries of the Josephson junctions. The critical currents of the Josephson junctions are given by $I_\mathrm{c1} = (1-\alpha)I_0$ and $I_\mathrm{c2} = (1+\alpha)I_0$ with I_0 the average critical current. When plugging Eq. 2.55 into Eq. 2.54, one arrives at

$$\omega_\mathrm{c}(\Phi) = \sqrt{\frac{S_0}{L_\mathrm{J0}C}} = \omega_\mathrm{c0}\sqrt{S_0}, \tag{2.56}$$

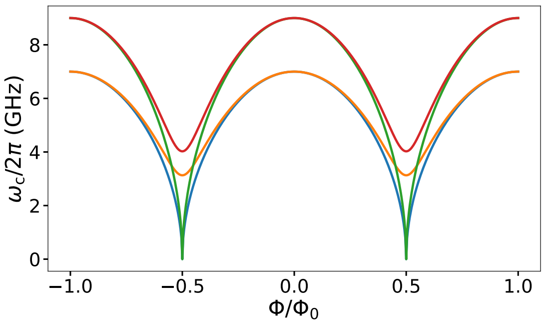

Figure 2.2.5.: Resonance frequency of a flux-tunable LC-resonator as given in Eq. 2.56 for different values of $\omega_{c0}/2\pi$ and α. We have chosen $\omega_{c0}/2\pi = 7\,\mathrm{GHz}$ for the blue and orange curve and $\omega_{c0}/2\pi = 9\,\mathrm{GHz}$ for the green and red curve as well as $\alpha = 0$ for the blue and green curve and $\alpha = 0.2$ for the orange and red curves.

with ω_{c0} the resonance frequency at vanishing flux. This approach is only justified if the Josephson inductance dominates over the loop inductance such that the latter is negligible and $\Phi = \Phi_b$. Figure 2.2.5 shows the resonance frequency as given in Eq. 2.56 for different values of ω_{c0} and α. We note that even relatively large values of $\alpha = 0.2$ do not affect the resonance frequency visibly for fluxes up to $|\Phi_b/\Phi_0| = 0.25$.

Flux-tunable distributed-elements resonators We now consider a distributed-elements resonator that is shunted to ground via a dc-SQUID. A schematic diagram of such a device is shown in Fig. 2.2.6. As we will see, the SQUID makes the resonance frequency of the whole resonator flux-tunable. In order to derive the resonance frequency of the FTR, we closely follow Refs. [58, 59, 60]. The classical Lagrangian of the flux-tunable cavity $\mathcal{L}_{\mathrm{cav}}$ consists of the Lagrangian of the bare cavity $\mathcal{L}_{\mathrm{cav}}^{(0)}$ and the Lagrangian of the SQUID $\mathcal{L}_{\mathrm{S}}$. The authors of Ref. [58] treat the FTR as a series of discrete LC-elements shunted by a SQUID with negligible loop inductance such that $\dot{\varphi}_- = 0$. Moreover, we assume both junctions to be identical as the authors of Ref. [59]. Then, the full cavity Lagrangian takes the form

$$\mathcal{L}_{\mathrm{cav}} = \mathcal{L}_{\mathrm{cav}}^{(0)} + \mathcal{L}_{\mathrm{S}} = \sum_{i=1}^{N-1} \left(\frac{\Phi_0}{2\pi}\right)^2 \left(\frac{C\dot{\phi}_i^2}{2} - \frac{(\phi_{i+1} - \phi_i)^2}{2L}\right) + \left(\frac{\Phi_0}{2\pi}\right)^2 \left(\frac{C\dot{\phi}_N^2}{2} - \frac{(\varphi_1 - \phi_N)^2}{2L}\right) + \frac{\hbar^2}{2E_C}\dot{\varphi}_+^2 + 2E_{\mathrm{J}}\cos(\varphi_-)\cos(\varphi_+) \tag{2.57}$$

Here, ϕ_i represents the phase across the i-th capacitance. Moreover, $C = C_0\,dx$ and $L = L_0\,dx$ are the linear capacitances and inductances of each element of infinitesimal length dx with the inductance L_0 and capacitance C_0 per unit length. We stress that the authors take only the second term of the SQUID potential in Eq. 2.51 into account.

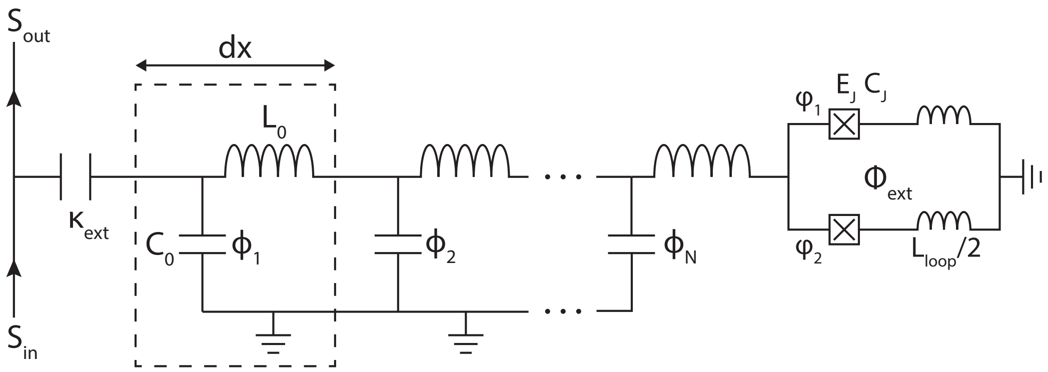

Figure 2.2.6.: Schematic of a distributed-elements flux-tunable resonator shunted to ground by a dc-SQUID. The two Josephson junctions are identical with Josephson energy E_J and capacitance C_J and phases φ_1 and φ_2 across them. Furthermore, the SQUID might have a finite loop inductance L_loop equally distributed over the arms and Φ_ext is the external flux threading the SQUID loop. The bare resonator itself consists of repetitive elements of infinitesimal length dx with inductance L_0 and capacitance C_0, both per unit length. For clarity, the first element is enclosed by a dashed rectangle. The superconducting phases across the capacitances are denoted by ϕ_i. The FTR is capacitively coupled to a microwave feedline with coupling strength κ_ext.

In the continuum limit, Eq. 2.57 becomes

$$\begin{aligned}\mathcal{L}_\mathrm{cav} = \Big(\frac{\Phi_0}{2\pi}\Big)^2 \int_0^d dx \Big(\frac{C_0\dot{\phi}^2}{2} - \frac{(\phi')^2}{2L_0}\Big) \\ + \frac{\hbar^2}{2E_C}\dot{\phi}_d^2 + 2E_\mathrm{J}(\cos(f)\cos(\phi_d))\end{aligned} \tag{2.58}$$

Here, we have introduced the field of the superconducting phase inside the cavity $\phi = \phi(x,t)$. The total length of the cavity is denoted by d and we have changed notation from φ_- to f and from φ_+ to $\phi_d = \phi(d,t)$ in order to be consistent with Refs. [58, 59] and to emphasize that the dynamical phase φ_+ of the SQUID is the boundary value of the cavity phase ϕ. It is important to note that the Langrangian contains ϕ and ϕ_d as dynamical variables.

When varying the action corresponding to the Lagrangian in Eq. 2.58 with respect to ϕ, one obtains a wave equation for the cavity field in the bulk

$$\ddot{\phi} - v^2\phi'' = 0, \tag{2.59}$$

where $v = 1/\sqrt{L_0C_0}$ is the wave velocity. With the boundary condition at the open end, $\phi'(x=0,t) = 0$, the above equation of motion is solved by eigenmodes of the form

$$\phi_n(x,t) \propto e^{\pm i\omega_n t}\cos(k_n x). \tag{2.60}$$

The condition that determines the wave number k_n (or equivalently the angular frequency $\omega_n = vk_n$) of the eigenmodes in Eq. 2.60 is obtained when varying the action corresponding to Eq. 2.58 with respect to the boundary value ϕ_d. It reads

$$\frac{\hbar^2}{E_C}\ddot{\phi}_d + 2E_{\mathrm{J}}\cos(f)\sin(\phi_d) + E_{L,\mathrm{cav}}d\phi_d' = 0, \tag{2.61}$$

with $E_{L,\mathrm{cav}} = (\Phi_0/2\pi)^2/(L_0 d)$ the characteristic inductive energy of the cavity. Note that the last term on the left hand side in the above equation stems from varying the part of the action corresponding to the bare cavity Langrangian at $x = d$. Now, we assume $\phi_d \ll 1$. This central assumption is valid because in the absence of the SQUID $\phi_d = 0$ at the end of the cavity and the SQUID changes the boundary value only slightly. Then, one can make the approximation $\sin(\phi_d) \approx \phi_d$ and plug the bulk solution from Eq. 2.60 into Eq. 2.61, arriving at

$$(k_n d)\tan(k_n d) = \frac{2E_{\mathrm{J}}\cos(f)}{E_{L,\mathrm{cav}}} - \frac{2C_{\mathrm{J}}}{C_0 d}(k_n d)^2. \tag{2.62}$$

In practice, $C_{\mathrm{J}}/(C_0 d) \ll 1$, such that the last term is negligible. From now on, we focus on the fundamental mode of the flux-tunable cavity with resonance frequency ω_{cav}. We replace wavenumbers by frequencies via

$$k_{\mathrm{cav}}d = \frac{\omega_{\mathrm{cav}}}{v}d = \frac{\pi}{2}\frac{\omega_{\mathrm{cav}}}{\frac{\pi v}{2d}} = \frac{\pi}{2}\frac{\omega_{\mathrm{cav}}}{\omega_0},$$

where ω_0 is the angular frequency of the fundamental mode of the bare $\lambda/4$ cavity, and obtain

$$\left(\frac{\pi}{2}\frac{\omega_{\mathrm{cav}}}{\omega_0}\right)\tan\left(\frac{\pi}{2}\frac{\omega_{\mathrm{cav}}}{\omega_0}\right) = \frac{2E_{\mathrm{J}}\cos(f)}{E_{L,\mathrm{cav}}}. \tag{2.63}$$

Usually, $E_{\mathrm{J}} \gg E_{L,\mathrm{cav}}$, such that $\omega_{\mathrm{cav}} \approx \omega_0$ for f close to the sweet spot, which is the applied flux where the frequency curve is flat. Then, one can expand the left hand side of Eq. 2.63 around $\omega_{\mathrm{cav}}/\omega_0 = 1$:

$$\left(\frac{\pi}{2}\frac{\omega_{\mathrm{cav}}}{\omega_0}\right)\tan\left(\frac{\pi}{2}\frac{\omega_{\mathrm{cav}}}{\omega_0}\right) \approx \frac{1}{1-\frac{\omega_{\mathrm{cav}}}{\omega_0}} - 1$$

Finally, one obtains the following expression for the resonance frequency of the FTR

$$\omega_{\mathrm{cav}} = \omega_0\left(1 + \frac{E_{L,\mathrm{cav}}}{2E_{\mathrm{J}}\cos(f)}\right)^{-1} = \omega_0\left(1 + \frac{L_{\mathrm{S}}}{L_{\mathrm{cav}}}\right)^{-1}, \tag{2.64}$$

where the cavity inductance is given by $L_{\mathrm{cav}} = L_0 d$ and the flux-dependent SQUID inductance $L_{\mathrm{S}} = \Phi_0/(4\pi I_{\mathrm{c}}|\cos(\pi\Phi_{\mathrm{b}}/\Phi_0)|)$ contains the bias flux Φ_{b}. We stress again that the validity of this expression is restricted to bias fluxes close to the sweet spot (Φ_b/Φ_0 almost integer) and a SQUID with negligible loop inductance.

For the case of a SQUID with finite loop inductance L_loop, it is suggested [61, 62, 60] to account for L_loop by replacing L_S by $L_\mathrm{S} + L_\mathrm{loop}/4$. This can be justified as follows. From the schematic of the FTR in Fig. 2.2.6 we see that in each arm of the SQUID, there are two inductances in series. Since inductances in series add up, the total inductance in arm 1 is $L_\mathrm{J1} + L_\mathrm{loop}/2$ and accordingly in arm 2. The total inductance of the SQUID is then given by

$$\frac{1}{L_\mathrm{S,total}} = \frac{1}{L_\mathrm{J1} + L_\mathrm{loop}/2} + \frac{1}{L_\mathrm{J2} + L_\mathrm{loop}/2}$$

as the inverse values of inductances in parallel add up. Only for $\phi_d = 0$, the Josephson inductances of the junctions are equal ($L_\mathrm{J1} = L_\mathrm{J2} = L_\mathrm{J}$) and the total inductance of the SQUID is given by

$$L_\mathrm{S,total} = \frac{L_\mathrm{J} + L_\mathrm{loop}/2}{2} = L_\mathrm{S} + \frac{L_\mathrm{loop}}{4},$$

with the SQUID inductance from Eq. 2.47. For a SQUID with finite loop inductance, the resonance frequency of the FTR then reads

$$\omega_\mathrm{cav} = \omega_0 \Big(1 + \frac{L_\mathrm{S} + L_\mathrm{loop}/4}{L_\mathrm{cav}}\Big)^{-1}. \tag{2.65}$$

In Fig. 2.2.7 (a), we show the resonance frequency of a FTR as given in Eq. 2.65 for finite and vanishing loop inductance and two different critical currents for $L_\mathrm{cav} = 1.8\,\mathrm{nH}$ [2]. The resonance frequency exhibits a periodicity of one flux quantum and reaches zero at $\Phi/\Phi_0 = (n + 1/2)$ ($n \in \mathbb{Z}$). However, this drop to zero is only present for perfectly symmetric junctions and therefore suppressed in real devices.

Next, we want to take into account the finite loop inductance in the SQUID potential. The Lagrangian of the SQUID is then given by

$$\mathcal{L}_\mathrm{S} = \frac{\hbar^2}{2E_C}\dot{\phi}_d^2 + 2E_\mathrm{J}(\cos(f)\cos(\phi_d) - \frac{\pi}{4}\beta_L \sin^2(f)\cos^2(\phi_d)). \tag{2.66}$$

While the wave equation for the cavity field in the bulk remains unchanged, one obtains a new boundary condition when varying the action with respect to ϕ_d. It is given by

$$\frac{\hbar^2}{E_C}\ddot{\phi}_d + 2E_\mathrm{J}(\cos(f)\sin(\phi_d) - \frac{\pi}{2}\beta_L \sin^2(f)\cos(\phi_d)\sin(\phi_d)) + E_{L,\mathrm{cav}} d\phi_d' = 0. \tag{2.67}$$

[2] This value corresponds to the cavity inductance of the device investigated in Chap. 6

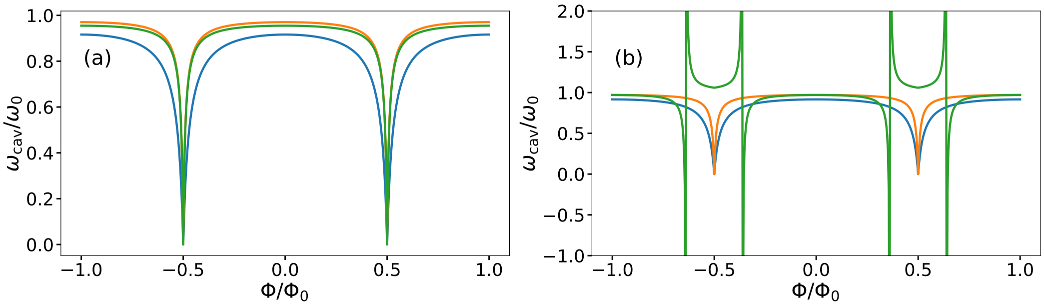

Figure 2.2.7.: Resonance frequency ω_{cav} of a flux-tunable distributed-elements resonator normalized to the resonance frequency of the bare cavity ω_0 as given in Eq. 2.65 (a) and Eq. 2.69 (b). We have chosen $I_0 = 1\,\mu\text{A}$, $L_{\text{loop}} = 0$ for the blue curves, $I_0 = 3\,\mu\text{A}$, $L_{\text{loop}} = 0$ for the orange curves and $I_0 = 3\,\mu\text{A}$, $L_{\text{loop}} = 120\,\text{pH}$ for the green curves. For all curves, $L_{\text{cav}} = 1.8\,\text{nH}$.

As before, we assume $\phi_d \ll 1$, approximate $\sin(\phi_d) \approx \phi_d$ and $\cos(\phi_d) \approx 1$ and plug the bulk solution of the cavity field Eq. 2.60 into the above boundary condition. This yields

$$\left(\frac{\pi}{2}\frac{\omega_{\text{cav}}}{\omega_0}\right)\tan\left(\frac{\pi}{2}\frac{\omega_{\text{cav}}}{\omega_0}\right) = \frac{2E_{\text{J}}(\cos(f) - \frac{\pi}{2}\beta_L \sin^2(f))}{E_{L,\text{cav}}}, \tag{2.68}$$

where we have again neglected the term $C_{\text{J}}/(C_0 d) \ll 1$. Again, we expand the tangent for $\omega_{\text{cav}} \approx \omega_0$ and obtain the final result

$$\omega_{\text{cav}} = \omega_0\left(1 + \frac{E_{L,\text{cav}}}{2E_{\text{J}}(\cos(f) - \frac{\pi}{2}\beta_L \sin^2(f))}\right)^{-1}. \tag{2.69}$$

The resonance frequency of the FTR as predicted by Eq. 2.69 is shown in Fig. 2.2.7 (b). For vanishing loop inductance (blue and orange curves), it is equivalent to Eq. 2.65, but shows a markedly different behavior for finite loop inductance (green curve). For the green curve in Fig. 2.2.7 (b), we have chosen $I_0 = 3\,\mu\text{A}$ and $L_{\text{loop}} = 120\,\text{pH}$ which corresponds to a realistic value of $\beta_L \approx 0.35$. While close to the sweet spot, the resonance frequency does not differ noticeably from the case with vanishing L_{loop}, its zero is now reached when $\cos(f) = \frac{\pi}{2}\beta_L \sin^2(f)$ and thus shifted towards smaller flux values. Furthermore, ω_{cav} exhibits a pole when the term in the brackets in Eq. 2.69 vanishes. As $E_{\text{J}} \gg E_{L,\text{cav}}$, this pole lies in the vicinity of the zero. Both the location of the zero and the pole depend on the precise value of β_L and are shifted further towards $\Phi/\Phi_0 = 0$ with increasing β_L. When approaching $|\Phi/\Phi_0| = 0.5$, the resonance frequency drops to a value slightly above ω_0 that again depends on β_L. We note that frequencies that correspond to fluxes outside of the zeros are not physical. This can be seen seen from Eq. 2.68: as soon as the numerator on the right hand side becomes negative, there is no solution for ω_{cav}. This indicates that Eq. 2.69 is not a sensible relation for the resonance frequency of the

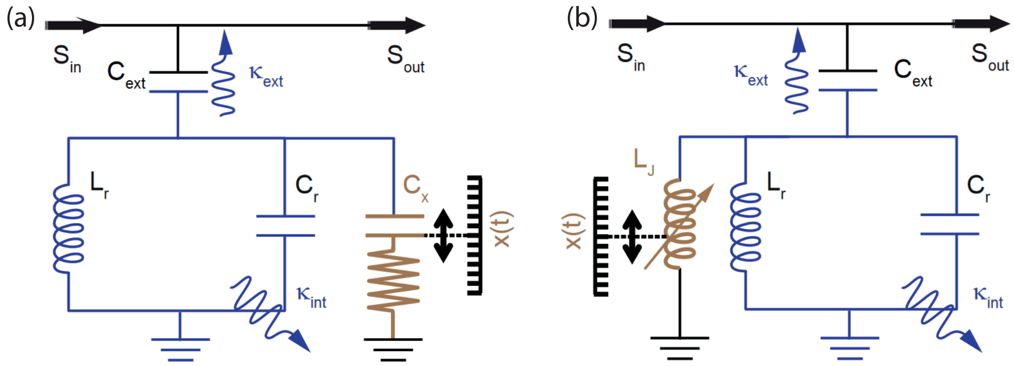

Figure 2.3.1.: Capacitive and inductive coupling schemes in electromechanics. In both cases, a lumped-element resonator with capacitance C_r and inductance L_r is coupled to a microwave feedline via a capacitance C_ext. In (a) the resonator's frequency is modulated mechanically via the displacement dependent capacitance C_x, resulting in capacitive coupling. In (b) the resonator's frequency depends on the Josephson inductance L_J. The magnetic flux threading the Josephson inductance is modulated mechanically, leading to inductive coupling. Taken from [60].

FTR. For completeness, we mention that it is in principle possible to fit experimental data close to the sweet spot with Eq. 2.69. However, one obtains unreasonable values for the loop inductance from this fit that are many orders of magnitude smaller than usual values.

2.3. Inductive coupling in electromechanics

The first demonstrations of light-matter coupling in electromechanics were achieved on systems where the mechanical motion modulates the capacitance $C = C(x)$ of a microwave cavity and therefore its resonance frequency $\omega_\mathrm{cav} = 1/\sqrt{LC(x)}$ [3, 11, 63, 64]. A schematic of a microwave resonator with a capacitively coupled mechanical oscillator is shown in Fig. 2.3.1 (a). After considerable optimization efforts, these capacitive coupling schemes were able to reach single-photon coupling rates of a few 100 Hz [11, 19]. As the internal damping rate κ_int of the microwave cavity is usually on the order of at least a few tens of kHz, these systems are however far away from the single-photon strong coupling regime. The disadvantage of devices implementing the optomechanical interaction by capacitive coupling is that the single-photon coupling rate g_0 is fundamentally limited by the geometry. For a plate capacitor with displacement dependent plate gap $d = d_0 + x$, it is easy to see that g_0 is bound by [27]

$$g_0 = \frac{\partial \omega_\mathrm{cav}}{\partial x} x_0 \leq \frac{\omega_\mathrm{cav}}{2} \frac{x_0}{d}. \tag{2.70}$$

Thus, the only way to increase g_0 in these devices is by optimizing the ratio x_0/d and minimizing all stray capacitances not participating in the modulation of C. However, the fabrication of devices with plate gaps below a few 10 nm becomes almost impossible, even with the most advanced methods of nanofabrication. Therefore, increasing g_0 beyond 300 Hz is extremely challenging with the approach of capacitive coupling [27].

In order to circumvent this limitation, inductive coupling schemes have been proposed [23, 24, 25, 26], where the single-photon coupling rate might reach values on the order of several tens of kHz [26]. With this enhancement by two orders of magnitude compared to capacitive coupling schemes, a realization of the single-photon strong coupling regime seems feasible. In the approach of inductive coupling, a displacement dependent inductance $L = L(x)$ needs to be integrated into the microwave resonator, such that the resonance frequency is modulated by the mechanical displacement. A schematic of a circuit with displacement dependent inductance in shown in Fig. 2.3.1 (b). In recent years, this approach has been demonstrated experimentally [28, 27, 29, 30], yielding single-photon coupling rates of a few kHz. Most implementations feature a flux-tunable resonator based on a dc-SQUID (see Sec. 2.2.4) whose inductance becomes displacement dependent by mechanically modulating the total flux threading the SQUID loop. In general, there are two ways of achieving this. Either, one modulates the external magnetic field while keeping the cross section of the SQUID loop constant. This can be accomplished by placing a cantilever with a magnetic specimen above the SQUID loop such that the motion of the cantilever changes the distance between SQUID and magnetic specimen, which was realized in Ref. [29]. Or, one keeps the external magnetic field constant and instead integrates a mechanically compliant string into the SQUID loop whose motion modulates the cross section of the loop. The latter approach was realized in Refs. [28, 27, 30] and will be the one we focus on in this work.

The single-photon coupling rate g_0 in the case of inductive coupling with vibrating strings is given by [23, 26]

$$g_0 = \frac{\partial \omega_{\mathrm{cav}}}{\partial x} x_0 = \frac{\partial \omega_{\mathrm{cav}}}{\partial \Phi} \frac{\partial \Phi}{\partial x} x_0 = \frac{\partial \omega_{\mathrm{cav}}}{\partial \Phi} \lambda B l x_0. \tag{2.71}$$

Here, λ is a dimensionless geometry factor that accounts for the shape of the mechanical mode coupling to the cavity [65], B an external magnetic field, l the length of the vibrating string and Φ the total external flux threading the SQUID loop. The derivative $\partial\omega_{\mathrm{cav}}/\partial\Phi$ of the cavity resonance frequency with respect to the total external flux is called the flux responsivity. As schematically illustrated in Fig. 2.3.2, the flux responsivity allows for an in-situ tunability of g_0 since it depends on the flux bias applied to the SQUID. This is a major advantage over capacitive coupling schemes where g_0 is determined by the geometry only. By an appropriate choice of the bias flux, it is possible to effectively

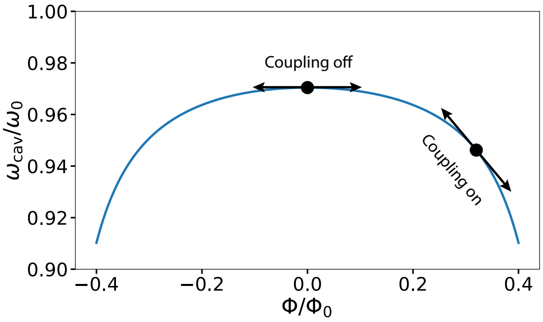

Figure 2.3.2.: Tunability of the single-photon coupling rate in Eq. 2.71. Shown is the resonance frequency of a FTR as given in Eq. 2.65. When operating the device at external fluxes where the flux responsivity $\partial\omega_{\mathrm{cav}}/\partial\Phi$ vanishes, the coupling can be turned off. In contrast, choosing a working point with a large flux responsivity allows for enhancing the coupling rate.

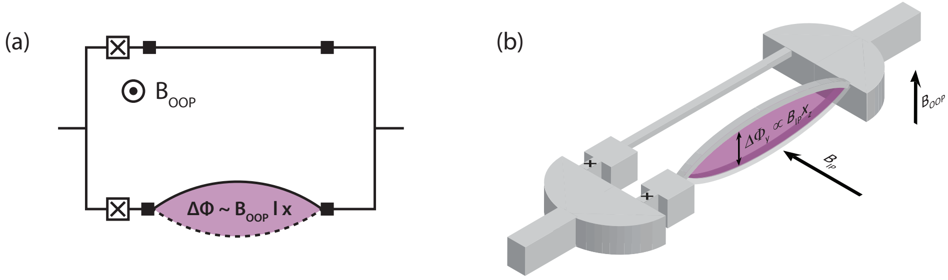

Figure 2.3.3.: Illustration of a mechanically compliant nanostring embedded into a SQUID that is part of a FTR. The out-of-plane magnetic field B_{OOP} generates a bias flux that allows for tuning the resonance frequency of the FTR. The mechanical motion is transduced to a change of the flux threading the loop by a magnetic field, which is the out-of-plane field B_{OOP} in the case of an in-plane mode (a). (b) In order to couple the out-of-plane mode to the FTR, an additional in-plane field B_{IP} is needed for the transduction. Taken from [31].

turn off or enhance the coupling. The bias flux is the part of the total external flux that is due to an out-of-plane magnetic field and it is the flux that determines the resonance frequency of the cavity. Operating the device at bias fluxes where the flux responsivity is large enables the previously mentioned single-photon coupling rates in the kHz range.

Finally, we want to distinguish between the interaction of an in-plane (IP) and an out-of-plane (OOP) mechanical mode with the microwave cavity. In the case of an IP mechanical mode, the relevant magnetic field B in Eq. 2.71 is just the external OOP field generating the bias flux, as depicted in Fig. 2.3.3 (a). When considering an OOP mode, B is the additional IP field B_{IP} needed to transduce the mechanical motion to a change of the flux threading the SQUID loop. An illustration of this case is shown in Fig. 2.3.3 (b). Although B_{IP} lies in the plane of the SQUID loop, it nevertheless contributes to the total magnetic flux as the OOP motion of the string corresponds to effectively canting the loop area. One advantage of this configuration is that one has access to two independent control parameters for tuning g_0 which are the bias flux and B_{IP}. Moreover, as g_0 scales linearly with B and superconducting thin films support larger IP than OOP fields until superconductivity breaks down, this configuration allows for significantly larger g_0.

2.4. Impact of a SQUID on the mechanical resonance frequency

2.4.1. Lorentz force induced mechanical frequency shift

In the previous chapter, we presented the concept of inductive coupling in electromechanics. Now, we focus on the influence of the microwave cavity on the mechanical resonator. In general, the coupling via the optomechanical interaction of a cavity to a mechanical resonator alters both the mechanical frequency and linewidth, which is known as backaction [1, 7, 65]. Here, we focus on the mechanical frequency and discuss different models of a mechanical resonator embedded in the loop of a dc-SQUID. We will see that in all models, the Lorentz force that acts on the resonator in the presence of an external magnetic field alters the resonator's stiffness which leads to a shift of the resonance frequency of the mechanical resonator.

Asymmetric SQUID with negligible loop inductance First, we consider a SQUID with negligible loop inductance and asymmetric Josephson junctions (i.e. with different critical currents). This case was treated in Ref. [26] and here, we closely follow this reference. The two Josephson junctions have critical currents of $I_{c1} = (1-\alpha)I_0$ and $I_{c2} = (1+\alpha)I_0$, where I_0 is the average critical current of the junctions and α a parameter quantifying the asymmetry. The gauge-invariant phase differences across the junctions are given by φ_1 and φ_2. Their sum $\varphi_+ = (\varphi_1 + \varphi_2)/2$ governs the dynamics of the SQUID, whereas the difference $\varphi_- = (\varphi_1 - \varphi_2)/2$ is fixed by the total magnetic flux Φ penetrating the SQUID loop

$$\varphi_- = \pi \frac{\Phi}{\Phi_0}. \tag{2.72}$$

It is convenient to split Φ into two different contributions. The first contribution is called the bias flux Φ_b and it is the flux penetrating the loop when the mechanical resonator is at $x = 0$. The second contribution stems from the resonator's oscillatory motion that modulates the cross section of the SQUID loop and therefore the total flux Φ, as we have seen in Sec. 2.3. It is given by λBlx, where l is the length of the mechanical resonator, λ the dimensionless geometry factor and B the component of the external magnetic field perpendicular to the plane of mechanical motion. In our experiments, B is the field in the plane of the SQUID loop, as we measure the mechanical motion perpendicular to the SQUID loop. Hence, the total flux Φ can be expressed as

$$\Phi = \Phi_\mathrm{b} + \lambda Blx. \tag{2.73}$$

Inserting this expression for Φ into Eq. 2.72 yields

$$\varphi_- = \pi\frac{\Phi_\mathrm{b}}{\Phi_0} + \pi\frac{\lambda Blx}{\Phi_0} = \pi\phi_\mathrm{b} + \xi x. \tag{2.74}$$

We now consider the classical Hamiltonian that describes the system of mechanical resonator and dc-SQUID in order to derive the shift of the mechanical resonance frequency. The Hamiltonian reads [26]

$$H = \frac{M_\mathrm{r}\dot{x}^2}{2} + \frac{M_\mathrm{r}\Omega_0^2 x^2}{2} + \frac{C_\mathrm{J}\Phi_0^2}{2(2\pi)^2}\dot{\varphi}_+^2 + E(\varphi_+, x), \tag{2.75}$$

where M_r is the effective mass of the resonator and Ω_0 its angular frequency. Throughout this work, we consider the fundamental mechanical mode, whose resonance frequency in the limit of highly tensile-stressed strings is given by [66]

$$\frac{\Omega_0}{2\pi} = \frac{1}{2l}\sqrt{\frac{\sigma_0}{\rho}}. \tag{2.76}$$

Here, l is the length, σ_0 the prestress and ρ the density of the string. It is crucial to note that $\Omega_0/2\pi$ is the resonance frequency of the uncoupled resonator, i.e. not subject to the influence of the SQUID. In contrast, the frequency of the resonator coupled to the SQUID is denoted by $\Omega_\mathrm{m}/2\pi$ and differs from $\Omega_0/2\pi$ due to backaction.
The last term in Eq. 2.75 represents the potential energy of the SQUID that gives rise to the coupling between the mechanical motion and the SQUID's dynamics. An important consequence of this coupling is that the Lorentz force $F_\mathrm{L} = BlI(\Phi)$ that the mechanical resonator experiences becomes displacement-dependent. This is because the mechanical displacement changes the total flux $\Phi = \Phi(x)$ and thus $F_\mathrm{L} = F_\mathrm{L}(\Phi(x))$. Consequently, this displacement-dependent Lorentz force alters the stiffness of the resonator and gives rise to a mechanical frequency shift. A schematic representation of a Lorentz force acting on a nanostring is given in Fig. 2.4.1. When the cavity frequency is much larger than the mechanical frequency, the potential energy of the SQUID takes the form

$$E(\varphi_+, x) = -2E_\mathrm{J}S(\varphi_-)\cos(\varphi_+), \tag{2.77}$$

where $S(\varphi_-) = \sqrt{\cos^2(\varphi_-) + \alpha^2\sin^2(\varphi_-)}$ takes into account the asymmetry of the junctions and $E_\mathrm{J} = \Phi_0 I_0/2\pi$ is the average Josephson energy. This is safely fulfilled in our case, as we operate with cavity frequencies in the GHz regime and mechanical frequencies in the MHz regime.

We can now treat the SQUID as a linear harmonic oscillator by expanding $\cos(\varphi_+) = 1 - \varphi_+^2/2 + \mathcal{O}(\varphi_+^4)$ and expand $S(\varphi_-)$ up to second order around zero displacement,

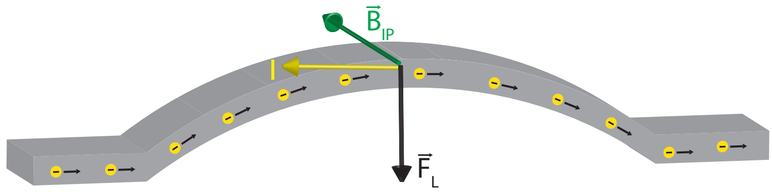

Figure 2.4.1.: A doubly-clamped nanostring subject to a Lorentz force $\vec{F}_{\mathrm{L}}$. The Lorentz force arises because the nanostring is part of a SQUID such that an electronic current I flows through it while an external in-plane field $\vec{B}_{\mathrm{IP}}$ is applied. The Lorentz force contributes to the stiffness of the nanostring and consequently changes the frequency of the out-of-plane mode.

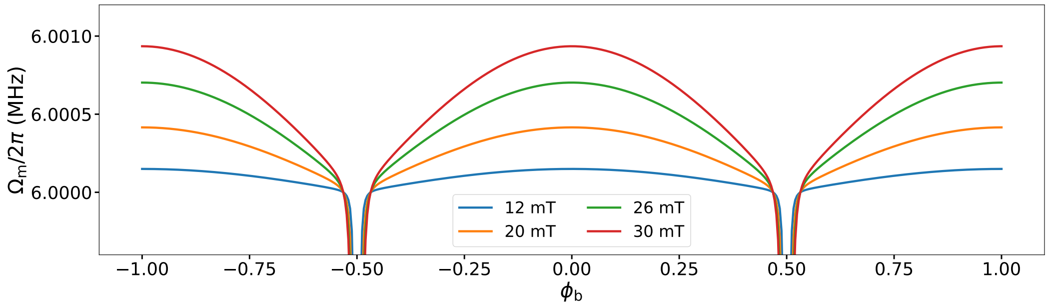

Figure 2.4.2.: Plot of the mechanical frequency $\Omega_{\mathrm{m}}/2\pi$ given in Eq. 2.78 as a function of normalized bias flux $\phi_{\mathrm{b}} = \Phi_{\mathrm{b}}/\Phi_0$ for external magnetic fields from 12 mT to 30 mT. We have fixed the other parameters to the following values: $\Omega_0/2\pi = 6\,\mathrm{MHz}$, $I_0 = 200\,\mathrm{nA}$, $l = 30\,\mu\mathrm{m}$, $M_{\mathrm{r}} = 0.9\,\mathrm{pg}$, $\lambda = 0.9$ and $\alpha = 0.01$.

leading to

$$E(\varphi_+, x) \approx -2E_{\mathrm{J}}\Big(S_0 + \frac{\partial S}{\partial \varphi_-}\big|_{\varphi_-=\pi\phi_{\mathrm{b}}}\xi x + \frac{1}{2}\frac{\partial^2 S}{\partial \varphi_-^2}\big|_{\varphi_-=\pi\phi_{\mathrm{b}}}\xi^2 x^2\Big)\Big(1 - \frac{\varphi_+^2}{2}\Big),$$

where $S_0 = S(\varphi_- = \pi\phi_{\mathrm{b}})$. The term quadratic in φ_+ gives rise to a radiation pressure interaction of the usual form $\hat{H}_{\mathrm{int}} = \hbar g_0 \hat{a}^\dagger \hat{a}(\hat{b}^\dagger + \hat{b})$. The term independent of φ_+ leads to a new equilibrium position x_0 due to the term linear in x and contributes to the potential energy via the term quadratic in x. This additional contribution to the resonator's potential energy results in a shifted mechanical frequency Ω_{m} expressed as [26]

$$\Omega_{\mathrm{m}} = \sqrt{\Omega_0^2 + \frac{2E_{\mathrm{J}}\pi^2\lambda^2 B^2 l^2(1-\alpha^2)(\cos^4(\pi\phi_{\mathrm{b}}) - \alpha^2\sin^4(\pi\phi_{\mathrm{b}}))}{M_{\mathrm{r}}\Phi_0^2 S_0^3}}. \tag{2.78}$$

The mechanical frequency of the coupled resonator as given in Eq. 2.78 is displayed in Fig. 2.4.2 for different values of B as a function of normalized bias flux ϕ_{b}. For the other parameters, we take the following values matching the device parameters discussed in Sec. 6.2: $\Omega_0/2\pi = 6\,\mathrm{MHz}$, $I_0 = 200\,\mathrm{nA}$, $l = 30\,\mu\mathrm{m}$, $M_\mathrm{r} = 0.9\,\mathrm{pg}$, $\lambda = 0.9$ and $\alpha = 0.01$. We see that the mechanical frequency is symmetric around vanishing bias flux and periodic in bias flux with a periodicity of Φ_0. The shift from the uncoupled frequency $(\Omega_\mathrm{m} - \Omega_0)/2\pi$ is maximal at $\phi_\mathrm{b} = 0$ and increases quadratically with B as can be seen from an expansion of Eq. 2.78 to first order in B.

Symmetric SQUID with finite loop inductance We now consider a symmetric SQUID with finite loop inductance L_loop. The reason we assume a symmetric SQUID is that the asymmetry between the junctions is usually very small when the junctions are fabricated in a single process [67], as the fabrication of Josephson junctions is a well-established and reliable process by now. Also, we have seen that even for quite large asymmetry of 0.2, the resonance frequency of the FTR does not differ significantly from the symmetric case close to the sweet spot where one usually operates (cf. Fig. 2.2.5). In the presence of a circulating current J, the loop inductance leads to a self-induced flux $L_\mathrm{loop}J$ that contributes to the total flux. Therefore, the phase difference φ_- now reads

$$\varphi_- = \pi\frac{\Phi_\mathrm{b}}{\Phi_0} + \pi\frac{\lambda Blx}{\Phi_0} + \pi\frac{L_\mathrm{loop}J}{\Phi_0} = \pi\phi_\mathrm{b} + \xi x + \pi\beta_L\frac{J}{2I_\mathrm{c}}, \tag{2.79}$$

As the circulating current J in the above equation depends on the total flux itself, it is usually not possible to find an analytical expression for φ_-. However, $\beta_L < 1$ in most cases, such that the last term in Eq. 2.79 can be omitted for $J/I_\mathrm{c} \ll 1$.
The classical Hamiltonian is still given by Eq. 2.75, but for the potential energy we now take

$$E(\varphi_+, x) = -E_\mathrm{S}(\varphi_-)\cos(\varphi_+), \tag{2.80}$$

where E_S denotes the Josephson energy of the SQUID. For a symmetric SQUID with finite loop inductance, it reads [61, 62]

$$E_\mathrm{S} = \frac{\Phi_0^2}{(2\pi)^2}\frac{1}{L_\mathrm{S} + L_\mathrm{loop}/4}, \tag{2.81}$$

where the SQUID inductance is given by

$$L_\mathrm{S} = \frac{\Phi_0}{4\pi I_0|\cos(\varphi_-)|}. \tag{2.82}$$

As before, we make the approximation $\cos(\varphi_+) = 1 + \mathcal{O}(\varphi_+^2)$ in order to derive the shift of the mechanical frequency due to a static external magnetic field. Again, all higher order terms in this expansion describe the interaction between the mechanical motion and the dynamics of the SQUID. In analogy to the previous approach, we expand $-E_\mathrm{S}(\varphi_-)$ to

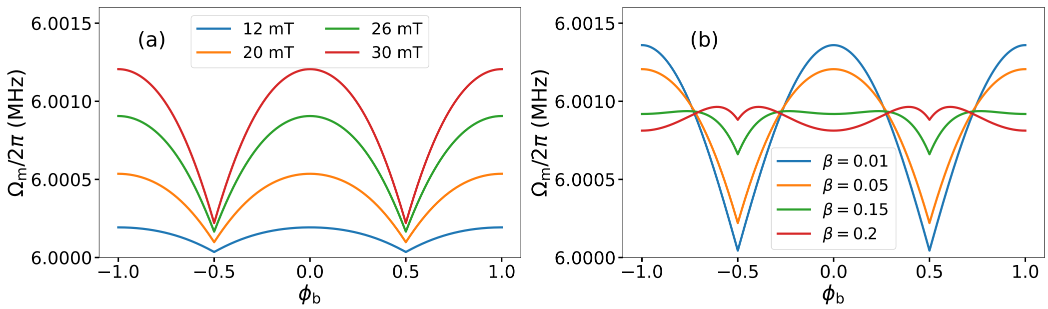

Figure 2.4.3.: Plot of the mechanical frequency $\Omega_\mathrm{m}/2\pi$ given in Eq. 2.83 as a function of normalized bias flux $\phi_\mathrm{b} = \Phi_\mathrm{b}/\Phi_0$ for constant $\beta = 0.05$ and different B (a) as well as for constant $B = 30\,\mathrm{mT}$ and various β (b). The other parameters are fixed to the following values: $\Omega_0/2\pi = 6\,\mathrm{MHz}$, $I_0 = 600\,\mathrm{nA}$, $l = 30\,\mathrm{\mu m}$, $M_\mathrm{r} = 0.9\,\mathrm{pg}$ and $\lambda = 0.9$.

second order in the mechanical displacement x. The term linear in x shifts the equilibrium position of the resonator and the term quadratic in x contributes to its potential energy. The corresponding shifted mechanical frequency Ω_m now reads

$$\Omega_\mathrm{m} = \sqrt{\Omega_0^2 + \frac{2E_\mathrm{J}\pi^2\lambda^2B^2l^2(|\cos(\pi\phi_\mathrm{b})| + \frac{\pi}{2}\beta(1+\sin^2(\pi\phi_\mathrm{b})))}{M_\mathrm{r}\Phi_0^2(1+\frac{\pi}{2}\beta|\cos(\pi\phi_\mathrm{b})|)^3}}. \tag{2.83}$$

We note that for $\beta = 0$ (negligible loop inductance) this expression for Ω_m coincides with the formula given in Eq. 2.78 for symmetric junctions ($\alpha = 0$).

In Fig. 2.4.3, we show the mechanical frequency as given in Eq. 2.83 for constant $\beta = 0.05$ and different B (Fig. 2.4.3 (a)) as well as for constant $B = 30\,\mathrm{mT}$ and various β (Fig. 2.4.3 (b)). We take the following values for the other parameters: $\Omega_0/2\pi = 6\,\mathrm{MHz}$, $I_0 = 600\,\mathrm{nA}$, $l = 30\,\mathrm{\mu m}$, $M_\mathrm{r} = 0.9\,\mathrm{pg}$ and $\lambda = 0.9$. As in Fig. 2.4.2, $\Omega_\mathrm{m}/2\pi$ is symmetric around $\phi_\mathrm{b} = 0$ and possesses a periodicity of Φ_0. In contrast to the model in Eq. 2.78, Ω_m is always higher than the uncoupled frequency Ω_0. For constant $\beta = 0.05$, the mechanical frequency is maximal at $\phi_\mathrm{b} = 0$ and the frequency tunability increases in first approximation quadratically with the applied field B. For constant B, the frequency tunability decreases with increasing β. At a certain value of β (for the parameters chosen here close to $\beta = 0.15$) the mechanical frequency becomes very flat around $\phi_\mathrm{b} = 0$ and finally develops a valley around vanishing bias flux such that Ω_m is minimal there for sufficiently large β. To our knowledge, such a behaviour has not been oberved experimentally yet.

2.4.2. Residual mechanical frequency shift

The models for the mechanical frequency of a nanostring presented in the previous section do not predict a change of the uncoupled mechanical frequency $\Omega_0/(2\pi)$. However, such a change was found in the experiments presented in [31]. There, the mechanical frequency

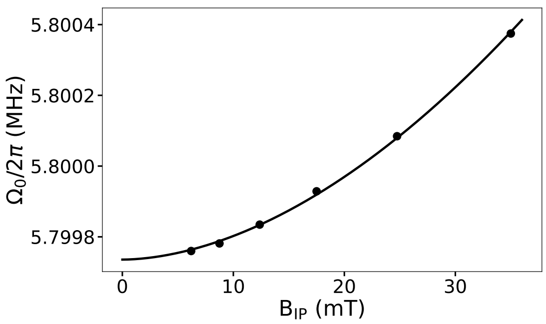

Figure 2.4.4.: Uncoupled mechanical frequency $\Omega_0/(2\pi)$ as a function of in-plane field B_{IP}. The data was published in Ref. [31] and obtained from measurements on the device presented in Chap. 3. The solid black line is a fit to Eq. 2.85 with $\alpha \propto B^{1.81}$.

of a nanostring integrated into the SQUID loop of a FTR was evaluated with the model from Eq. 2.78 as a function of bias flux and in-plane field B_{IP}. The dependence of $\Omega_0/(2\pi)$ on B_{IP} obtained in that work is shown in Fig. 2.4.4. One sees that the residual shift $\Delta\Omega_0/(2\pi)$ of the uncoupled mechanical frequency is on the order of several 100 Hz.

The authors ruled out several potential origins of this residual frequency shift that we want to briefly recapitulate here. First, the volume increase of the superconducting Al nanostring for in-plane fields close to the critical field was considered. The relative volume increase for Al is stated in literature to be on the order of $\Delta V/V \approx 1 \times 10^{-8}$ [68]. The mechanical frequency of a highly tensile-stressed nanobeam is given by Eq. 2.76, such that the frequency change due to a length increase of Δl is given by

$$\frac{\Delta\Omega_0}{2\pi} = -\frac{\Omega_0}{2\pi}\frac{\Delta l}{l}, \tag{2.84}$$

which is negative and on the order of 1×10^{-8} as well. This does not fit the experimental observation of a frequency increase on the order of 1×10^{-4}.

Next, they thought about the possibility of second order contributions to the optomechanical interaction giving rise to the observed frequency increase [33]. The second order contribution would result in an increase of the mechanical frequency with B_{IP}^2, which is in good agreement with the experimental data in Fig. 2.4.4. However, the expected frequency shift would be on the order of a few Hz for the parameters of the measured device and thus substantially smaller than the observed shift of a few 100 Hz.

Also, they were able to disprove by means of an additional measurement the hypothesis that a magnetic torque acting on the nanostring causes the observed frequency shift. This magnetic torque would be a consequence of a magnetic moment of the SQUID loop due to trapped flux and a small misalignment between this magnetic moment and the in-plane field. Hence, it would be proportional to the number of trapped flux quanta in the loop. However, no difference in the mechanical frequency was found for different numbers of flux quanta in the experiment.

Instead, experiments with superconducting vibrating reeds in external static magnetic fields provide a possible explanation for the residual frequency shift [69, 70, 71]. When a type-II superconductor is placed in an external magnetic field B that is sufficiently large, magnetic flux in the form of flux lines penetrates the sample [72]. This behavior is present for external fields $B_{\mathrm{c1}} < B < B_{\mathrm{c2}}$, where B_{c1} is the lower and B_{c2} the upper critical field. Although we deal with a nanostring made of Al, it is known that sufficiently thin Al films behave as type-II superconductors [73] and thus allow for the penetration of flux lines. Each flux line comprises a normal conducting core that is surrounded by circulating currents and carries precisely one flux quantum $\Phi_0 = h/(2e)$. The flux lines in the sample are pinned at pinning sites such as impurities or defects in the crystal lattice and arrange in a flux line lattice. When the reed moves in the external field, the flux lines follow the reed due to the pinning and therefore bend. This bending results in elongated field lines and therefore an increase in the magnetic energy, which can be described in terms of a magnetic line tension (energy per unit length). As a consequence, an additional restoring force arises, leading to an increase of the mechanical resonance frequency. For rigidly pinned flux lines, the line tension and therefore the frequency increase are proportional to B^2 [71]. When there is a finite displacement of the flux lines relative to the pinning centers, the frequency increase is smaller than for rigidly pinned flux lines. The coupling strength between the flux lines and the atomic lattice is quantified by the Labusch parameter (also called elastic constant) $\alpha = \alpha(B, T)$ that can be thought of as the spring constant of a system composed of flux line and pinning site. For very small pinning forces, the resonance frequency Ω of a reed in an external field reads [69]

$$\Omega^2 = \Omega_0^2 + \frac{\alpha(B,T)}{\rho}, \tag{2.85}$$

where Ω_0 is the resonance frequency in the absence of external field and ρ the density of the material. This equation shows that the frequency shift with B is only due to the dependence of the Labusch parameter on B, such that it allows to determine the pinning forces the flux lines experience [71]. This dependence follows a power law $\alpha(B,T) \propto B^k$, where the exponent k differs between materials. The solid black line in Fig. 2.4.4 is a fit of the data points to the above equation, yielding $k \approx 1.81$ and a Labusch paramter of $7.88 \times 10^{14}\mathrm{N/m^4}$ at $35\,\mathrm{mT}$ [31]. This is in good agreement with values of $k = 2 \pm 0.2$ and Labusch parameter between $10^{10}\mathrm{N/m^4}$ and $10^{15}\mathrm{N/m^4}$ found in other experiments [69, 71, 74]. Hence, these findings are quantitatively compatible with the interpretation that the pinning of flux lines underlies the residual mechanical frequency shift. If that is the case, the mechanical frequency should increase in a discontinuous, step-like manner whenever an additional flux line is created in the nanostring, thus revealing the quantization of magnetic flux. We will further investigate this hypothesis in Chap. 6.

Chapter 3.

The device layout

Our device is inspired by a sample made by Philip Schmidt at the WMI, about which detailed information can be found in Ref. [28]. It consists of superconducting coplanar waveguide $\lambda/4$-microwave resonators that are capacitively coupled to a feedline and shorted to ground by a dc-SQUID that makes the resonance frequency flux-tunable. Panel (a) of Fig. 3.0.1 shows a flux-tunable microwave resonator and panel (b) of Fig. 3.0.1 the SQUID. Both the microwave resonators and the SQUID are made of Al on top of a Si substrate. The flux-tunable resonator that was investigated in Ref. [28] has a resonance frequency of $\omega_\mathrm{c} = 7.445\,\mathrm{GHz}$, a total linewidth of $\kappa/2\pi = 2.5\,\mathrm{MHz}$ and an internal linewidth of $\kappa_\mathrm{int}/2\pi = 2\,\mathrm{MHz}$, all at the sweet spot where the flux responsivity $\partial\omega_\mathrm{c}/\partial\Phi$ vanishes. This corresponds to an internal quality factor of the FTR of roughly $Q_\mathrm{int} = 3700$. In practice, the internal linewidth of the microwave resonator would be even larger than $2\,\mathrm{MHz}$ as one would typically operate the device at working points with finite flux responsivity where the resonator becomes more susceptible to flux noise. The SQUID loop features two nanostrings with a length of $30\,\mathrm{\mu m}$, a width of $200\,\mathrm{nm}$ and a thickness of $110\,\mathrm{nm}$. With the density of Al of $2700\,\mathrm{kg/m^3}$ [50], this amounts to a mass of $m = 1.8\,\mathrm{pg}$ and an effective mass of $m_\mathrm{eff} = m/2 = 0.9\,\mathrm{pg}$ for the fundamental mode that we focus on [60]. In order to establish inductive coupling between the mechanical motion and the electromagnetic fields of the resonator, both nanostrings are released from the substrate and therefore able to move. A SEM image of the nanostrings can be seen in panel (c) of Fig. 3.0.1. The nanostrings exhibit an in-plane (IP) and out-of-plane (OOP) mode that can both couple to the resonator, depending on the direction of the applied external magnetic field. In the case of an OOP (IP) external field, the IP (OOP) mode modulates the total flux threading the loop and thereby changes the flux-dependent Josephson inductance of the SQUID (cf. Sec. 2.3). Due to tensile prestress, the nanostrings have a comparatively high mechanical resonance frequency of $\omega_\mathrm{m}^\mathrm{IP} \approx 6.3\,\mathrm{MHz}$ for the IP mode [28] and $\omega_\mathrm{m}^\mathrm{OOP} \approx 5.8\,\mathrm{MHz}$ for the OOP mode [31]. As these frequencies exceed the total cavity linewidth, the device resides in the resolved-sideband regime (cf. Sec. 2.1). This regime had been realized in both optomechanical [75] and electromechanical systems [76].

When operating the device at mK temperatures as we do in our experiments, the thermal occupation of the mechanical modes amounts to a few hundred phonons. This relatively large thermal occupation results in a noticeable mechanical motion that can be measured without further driving the mechanical mode. In order to obtain a large participation ratio, the loop area of the SQUID is chosen to be as small as possible, in this case $44.6\,\mu m^2$. This way, the mechanical motion modulates a large part of the total flux, which enhances the vacuum optomechanical coupling strength. Indeed, a vacuum coupling strength of up to $g_0/2\pi = 1.62\,\mathrm{kHz}$ was reported for the OOP field configuration [28] and even up to 55 kHz for the IP field configuration that allows for larger magnetic fields [31]. These coupling strengths are substantially larger than typical coupling strengths in capacitively coupled systems, as we have discussed in Sec. 2.3. However, the ratio $g_0/\kappa_{\mathrm{int}}$ is on the order of 10^{-3}, meaning that the device is far from the single-photon strong coupling regime. We suspect that the main reason for the low internal quality factors is the choice of materials and the fabrication process. Both microwave resonators and SQUIDs were fabricated in a single lift-off procedure and therefore consist of an Al/AlOx/Al trilayer. The oxide layer in between the Al layers is crucial for the formation of the Josephson junctions in the SQUID. The disadvantage of this trilayer structure is that interfaces between Al and the oxide host a significant amount of two-level systems (TLS) that can absorb microwave photons and hence introduce losses [77]. In addition, the trilayer can lead to the formation of parasitic Josephson junctions away from the intended locations of junctions. However, this was not observed in this device.

An obvious approach for reaching the single-photon strong coupling regime would thus be to increase Q_{int} while maintaining a similarly large vacuum coupling strength g_0 in the kHz range. To do so, we have chosen different materials for the components of our electromechanical system and come up with a more sophisticated fabrication process. The overall geometry of our device is the same as for the device of Philip Schmidt, i.e. $\lambda/4$-microwave resonators that are capacitively coupled to a microwave feedline. The microwave resonators have different lengths and therefore different resonance frequencies. Half of the resonators is flux-tunable as they are shunted to ground by a dc-SQUID. An overview of the whole chip with microwave feedline and resonators is shown in Fig. 3.0.2 (a). In contrast to the previous device generation, we fabricate the microwave resonators from thin films made of Nb instead of Al. A flux-tunable microwave resonator with a SQUID at its end can be seen in Fig. 3.0.2 (b). This is a reasonable choice as standard CPW resonators made from Nb have been demonstrated to reach quality factors exceeding 10^6 and their fabrication has been heavily optimized at the WMI [78]. One reason for these enhanced quality factors is that Nb has a critical temperature of 9.25 K, whereas that of Al is only 1.19 K [50]. As a consequence, the number of quasiparticles in Nb is smaller than that in Al at the same temperature, which leads to lower resistive

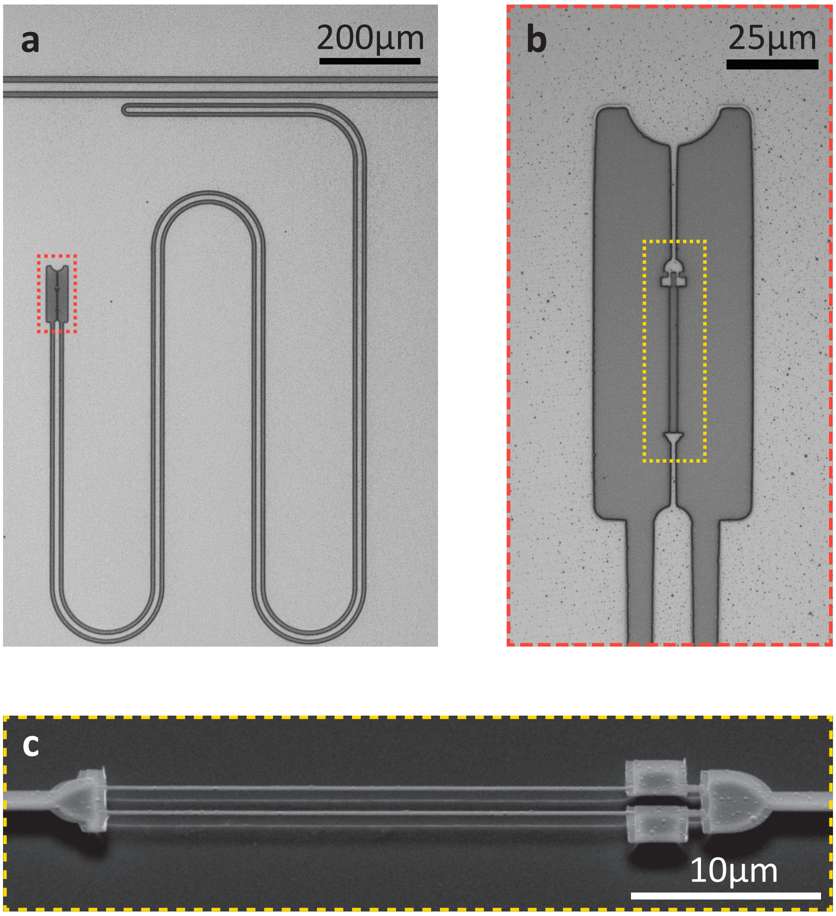

Figure 3.0.1.: Images of the previous device generation fabricated in a single lift-off step. Panel (a) shows a flux-tunable $\lambda/4$-microwave resonator capacitively coupled to a microwave feedline. In panel (b), a zoom-in on the Al SQUID can be seen. Panel (c) shows a SEM image of the two mechanically compliant nanostrings integrated into the SQUID loop. The two Josephson junctions are located to the right of the nanostrings. The images shown here have been published in [31].

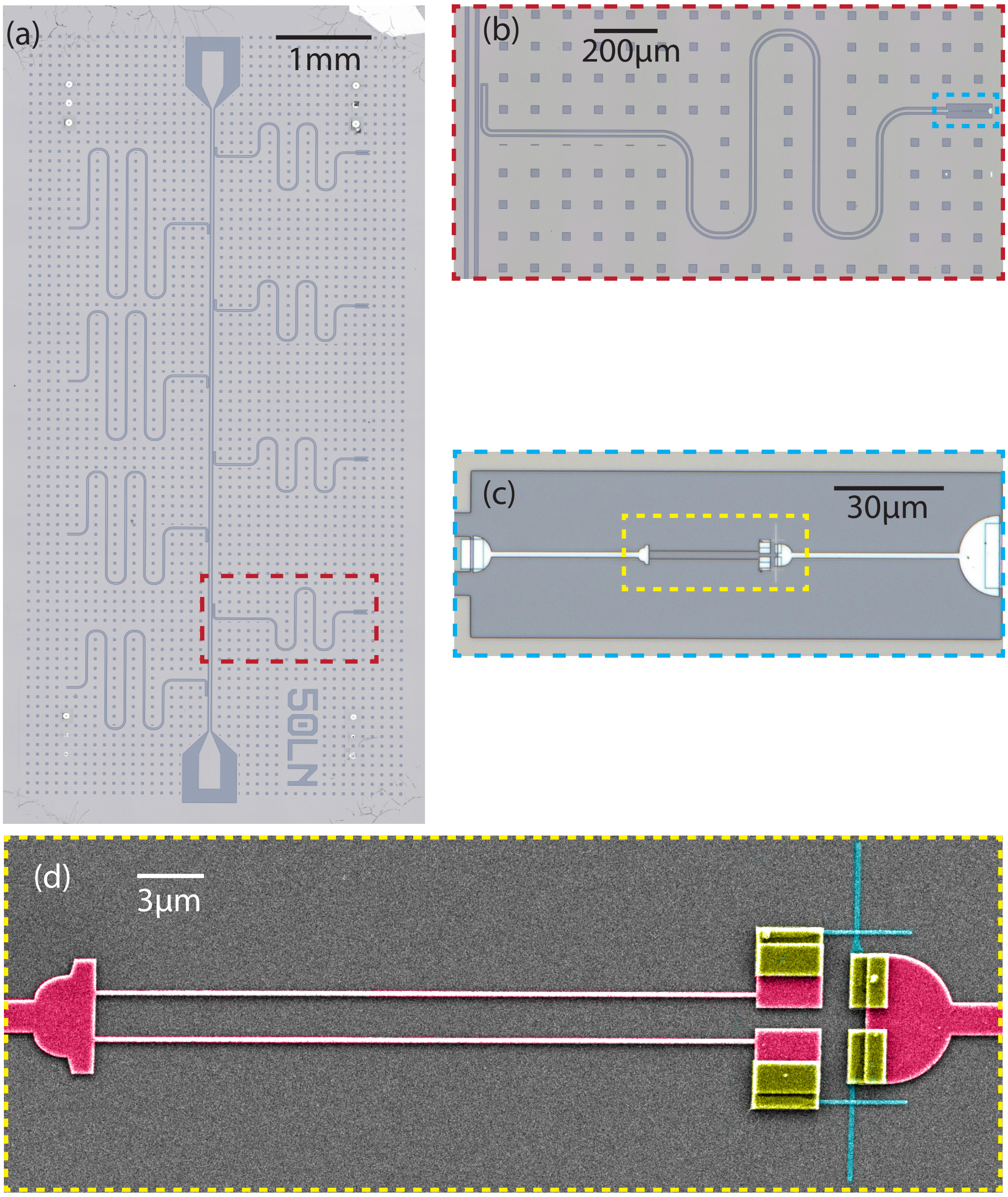

Figure 3.0.2.: Images of one of the devices fabricated for this work using the new multi-step process. Panel (a) shows the whole sample with microwave feedline and eight microwave resonators, of which the four to the right are flux-tunable. Panel (b) shows a flux-tunable microwave resonator that is capacitively coupled to the feedline at one end and shunted to ground by a SQUID at the other end. A zoom-in on the SQUID is depicted in panel (c), where the two thin nanostrings are visible. A false-colored scanning electron micrograph can be seen in panel (d), where the SQUID is pink, the two Manhattan type Josephson junctions are turquois, the bandages are yellow and the two nanostrings are visible as white thin lines.

losses and contributes to a higher quality factor [44]. For the nanostrings as well as the SQUID, we still choose Al due to its well-studied mechanical properties [66] and the ease of fabricating Josephson junctions with Al. However, the SQUID is now made in three consecutive steps, which ensures that the oxide layer is only present in the Josephson junctions and not in the rest of the SQUID. By avoiding these unwanted Al/AlOx interfaces, the number of TLS and therefore the loss rate is greatly reduced. Panel (c) of Fig. 3.0.2 shows a SQUID with integrated nanostrings and a SEM image of the nanostring and the Josephson junctions can be seen in panel (d). The Manhattan-type Josephson junctions (false-colored in turquoise) consist of two arms that are perpendicular to each other. The overlap of these two arms constitutes the junction area through which charge carriers have to flow. A galvanic contact between the SQUID (false-colored in pink) and the Josephson junctions is established by bandages (false-colored in yellow). Further details on the fabrication process of our samples are given in Sec. 4.1.

Under the assumption that in our device vacuum coupling strengths around 50 kHz are within reach as well, a linewidth of the FTR not larger than this value would be required for the single-photon strong coupling regime. With a typical resonance frequency of 10 GHz of the FTR, this would correspond to an internal quality factor on the order of 2×10^5, which seems realistic with our modifications.

Chapter 4.

Methods

4.1. Fabrication of flux-tunable resonators

4.1.1. Fabrication procedure

In the following, we explain in detail the fabrication of our flux-tunable resonators (FTRs) that were introduced in Chap. 3. An overview of the fabrication process is given in Fig. 4.1.1 and detailed fabrication recipes are provided in Sec. B.

In a first process step shown in panel (a) of Fig. 4.1.1, we pattern microwave resonators into 150 nm thick Nb thin-films that were previously sputtered onto Si substrates of size $6\times10\,\mathrm{mm}^2$. To do so, we spin-coat a blank Nb chip with AZ MIR 701 positive photoresist. After a pre-exposure bake, the resonators are written in a PicoMaster 200 direct laser writer. A subsequent post-exposure bake is crucial in order to increase the etch stability of the photoresist. As we write with a positive photoresist, the resist that was exposed to laserlight gets removed during the development with AZ MIF 726, such that the resist forms a mask for the following step of reactive ion etching (RIE). During that process, a mixture of SF_6 and Ar^+-ions, that are accelerated towards the surface of the sample, etch away the metal that is not protected by photoresist. As the accelerated Ar^+-ions cause a surface roughening of the underlying Si substrate and both Ar^+-ions and SF_6 etch Si, the right duration of the RIE process is important in order to avoid unnecessary damage of the substrate. For that reason, we later resorted to etching only with SF_6 as it has an etching rate of Si that is smaller than that of Ar^+ and furthermore leads to smoother Si surfaces. However, the etching process only with SF_6 is less anisotropic and can lead to larger under-etching and rounded edges. Therefore, process paramters have to be chosen with care. After the RIE process, the remaining photoresist is removed with Technistrip P1331.

In a second process step shown in panel (b) of Fig. 4.1.1, we fabricate the main part of the SQUID in the pocket at the end of the FTR. The main part consists of the nanostrings with a nominal width of 200 nm and the leads to ground and to the microwave resonator with a width of 1.5 µm. (The Josephson junctions as well as the bandages that

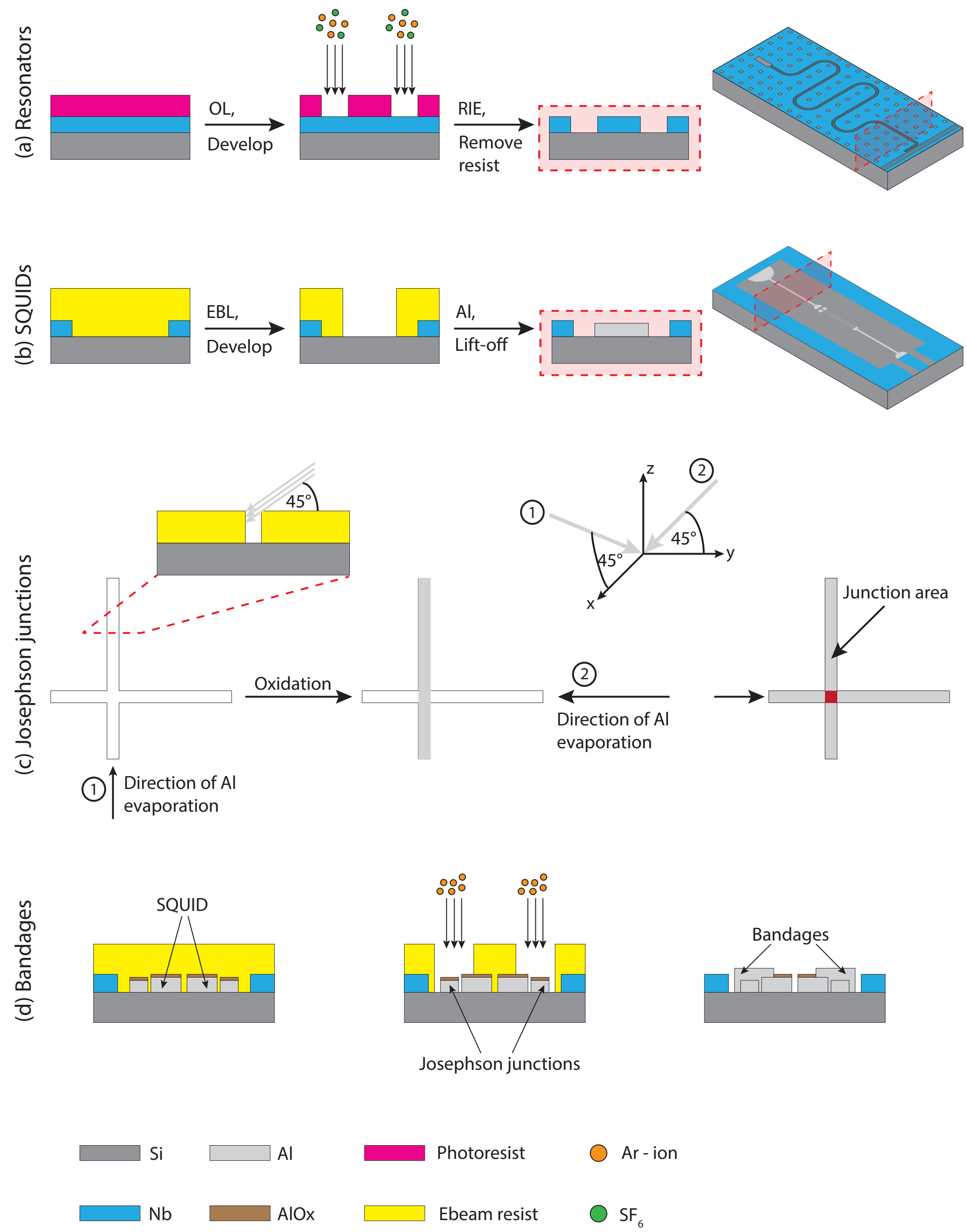

Figure 4.1.1.: Overview of the fabrication process. The fabrication process consists of four different steps. (a) Microwave resonators are patterned into Nb thin films by a standard optical lithography (OL) process followed by RIE. (b) SQUIDs are fabricated in the pockets at the end of the FTRs by means of electron-beam lithography (EBL), Al evaporation and lift-off. (c) The Manhattan-type Josephson junctions are fabricated in a shadow-evaporation process. (d) A galvanic contact between all previously fabricated components is established by Ar ion milling and a bandaging technique.

establish a galvanic contact will be fabricated in subsequent process steps.) Due to the small feature sizes of these elements, we make use of our in-house nanobeam electron beam lithography system. We first spin-coat our sample with a double-layer stack of two different electron beam lithography resists (e-beam resists): CSAR 62 at the bottom and PMMA 950K at the top. This results in a total resist height of 1 µm. After the electron-beam lithography process and development of the double-layer stack with AR 600-56 and AR 600-546, we evaporate 150 nm of Al for the SQUIDs in a Plassys electron beam evaporator. Before the evaporation of the SQUID's main part, we remove organic resist residues by an ozone descumming process which is expected to improve the internal quality factor of the FTR. The descumming results in a slight enlargement of structure sizes, which can be in principle compensated for in the design file. Finally, lift-off with AR600-71 removes the resist and the Al on top of it such that only the main part of the SQUID remains.

In a third process step shown in panel (c) of Fig. 4.1.1, two Manhattan-type Josephson junctions (JJs) [79, 80] are fabricated to complete each SQUID. As for the main part of the SQUID, we define the junctions using the double-layer resist stack described above in combination with e-beam lithography, patterning, development and an ozone descumming step. The shadow-evaporation of the junctions then happens in two steps. In the first step of Al evaporation, the sample is tilted by 45° around the y-axis. This way, only one arm of the junction is evaporated. The reason for the other arm not being evaporated is that the width of the junction is 170 nm, whereas the height of the resist is 1 µm. As the evaporation occurs under an angle of 45°, the Al is deposited only onto the top-layer resist and not on the Si substrate. In this first step, we evaporate 30 nm of Al. Then, the evaporated arm of the JJ is oxidized in a controlled manner using dynamic oxidation at 5 mTorr in order to form an AlOx layer that constitutes a tunneling barrier between the two superconducting Al arms of the JJ. For the second evaporation step, the direction of evaporation is rotated by 90° while maintaining a tilt angle of 45°. This way, the second arm of the JJ is evaporated onto the Si substrate. In this second step, we evaporate 70 nm of Al. The junction area is the region where the two arms overlap.

In a forth and final process step shown in panel (d) of Fig. 4.1.1, we establish a galvanic contact from the microwave resonator to the SQUID to ground and between the SQUID's main part and the JJs by a bandaging process. The bandaging requires removing the native oxide layers on top of Nb and Al by Ar-ion milling before the evaporation of the bandages in order to avoid the formation of parasitic Josephson junctions. Moreover, it was shown in Ref. [81] that oxide layers between Nb/Al interfaces are a source of TLS losses when they are located at antinodes of the current, as it is the case in our device. The advantage of this bandaging technique is that the substrate underneath the metals is not damaged by Ar-ions during the process of Ar-ion milling, leading to enhanced internal quality factors compared to a simpler process where oxide removal by milling is done prior to junction evaporation [82]. For the Ar-ion milling, we use a Kaufman ion source that is connected to the load lock of the Plassys system.

4.1.2. Process optimization

Now, we report on major challenges identified during the fabrication of FTRs using this multi-step process.

Junction yield We were facing the problem of JJs tearing off during the lift-off process. A corresponding example is shown in panel (a) of Fig. 4.1.2. We speculate that there are two main reasons for the junctions tearing off. First, we suppose that the surface roughness of the Si substrate introduced by the RIE process reduces the adhesion of the junctions to the substrate. This assumption is supported by the observation that JJs did not tear off on test Si samples where RIE was not performed. Second, we lack a pronounced undercut in the lower resist of the double-layer stack, as can be seen in the SEM-image in panel (b) of Fig. 4.1.2. Therefore, the deposited JJs stick to the lower resist and tear off during lift-off. In order to circumvent this problem, we put an additional ghostlayer around the junction where we were going to deposit a dose that would develop the lower CSAR resist only, which clears at lower doses than PMMA 950K. However, this approach was not successful and led to a broadening of the structure in both the upper and the lower resist. We suspect this happens because the two resists are sensitive to both the AR 600-56 and the AR 600-546 developer. As a workaround, we made the arms of the junctions longer and added Dolan bridges at the end of each arm, which are narrow bridges in the resist suspended from the substrate [83]. Panel (c) of Fig. 4.1.2 shows a schematic of a JJ with longer arms and Dolan bridges. Since we observed that the JJs always tore off from their ends, we were hoping the increased length would avoid that the junction area tears off as well. In addition, the Dolan bridge should decrease the probability of junctions tearing off, although we do not know for certain whether the lower resist under the bridge is fully removed during development. Finally, we made a lift-off test chip only with JJs and Dolan bridges of different widths (and without SQUIDs) in order to find the optimal values for these parameters. We obtained decent results for a nominal width of 170 nm for the junctions and 150 nm for the Dolan bridges. We used these values for the fabrication of all further samples. With these values, JJs still tear off in our samples where they are part of a SQUID, but less frequently than before. This indicates that the geometry surrounding the JJs also plays a role in the stability of the JJs. In order to minimize the frequency of junctions tearing off, we resort to a very smooth lift-off process, where we put the chip at 40 °C for at least two hours

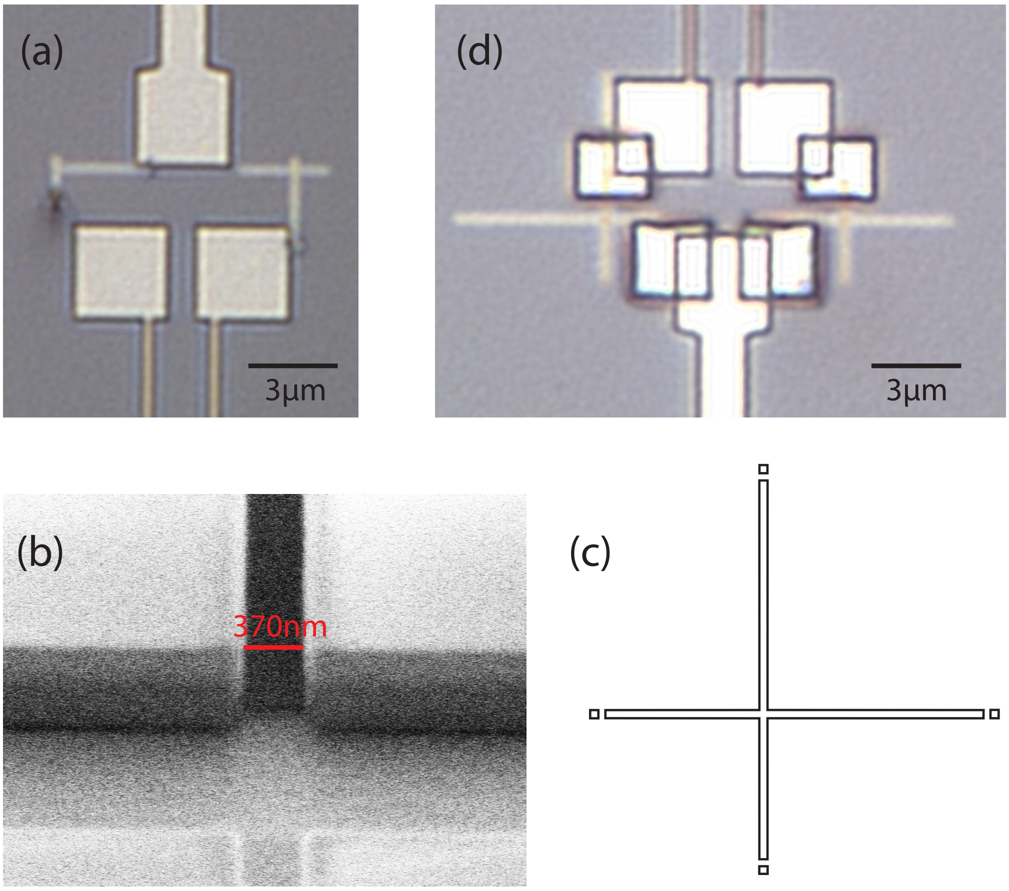

Figure 4.1.2.: Challenges in the fabrication of FTRs. Panel (a) shows an optical micrograph image of the junction region of a FTR, where one arm of the left junction tore off during lift-off. Panel (b) shows a SEM-image of the double-layer resist stack used for the fabrication of JJs. In contrast to our expectation, no undercut is visible in the lower resist, which seems to be one reason for junctions tearing off during lift-off. Panel (c) shows a schematic of a JJ with longer arms and Dolan bridges at the end of the arms. With these modifications, JJ should be less likely to tear off during lift-off. Panel (d) shows an optical micrograph image of the junction region of a FTR after bandaging. Due to misalignment, there is no galvanic contact between the lower bandages and the JJs.

in AR600-71 remover, then carefully blow away the Al with a pipette and rinse with isopropanol at the end.

Finally, we note that advances in the fabrication of superconducting qubits on wafer-scale at the WMI recently showed that a HF dip prior to junction evaporation fully solved the problem of junctions tearing off. This confirms that the surface roughness of the substrate is a main cause for the observed tear-off of JJs. However, this workaround is not applicable in our case, as a HF dip would damage the nanostrings of the SQUID.

Multi-step alignment An additional problem we had to cope with concerns the relative alignment of the various layers used for the fabrication of our devices. As the feature size of these structures is of the order of 100 nm, a precise relative alignment is crucial. Unfortunately, we initially found that the alignment accuracy between subsequent e-beam lithography steps was insufficient; especially the bandages showed a substantial misalignment in many cases. Moreover, the misalignment was not reproducible between different samples and could be as large as 1 µm, which results in a lack of galvanic contact between parts of the device. An example of such a device is shown in panel (d) of Fig. 4.1.2. We observed alignment errors to become increasingly large with subsequent steps, and realized that repeated use of the same markers (which are covered by aluminum in every evaporation step) can introduce focus offsets due to the added metal. We think that the deposited Al on the markers makes accurate focussing more difficult. To mitigate this problem, we tried using multiple sets of markers for the focussing during the e-beam lithography. For example, we put markers in one column in a distance of 200 µm and used a new marker for each step in the nanobeam. While the focus offsets can be avoided this way, and it is generally advisable to use multiple sets of markers, it did not solve the problem of larger non-reproducible alignment errors. Alternatively, we suspected that the lack of nm-scale accuracy in the optical lithography step could lead to the observed misalignment. As the exposure of a single chip in the direct laser writer takes several hours, it is possible that drifts in the operating conditions over time lead to deviations between the target layout and the final exposed resonator structures. To investigate this hypothesis, we put marker systems close to each pocket, such that markers and pocket are within close proximity and should suffer less from any time-dependent drifts. As that did not solve the problem either, we fabricated an entire chip, including the resonators, using e-beam lithography and lift-off. However, this resulted in a considerable misalignment between resonators and SQUIDs as well. Finally, we learned about the registration writing mode of the nanobeam that was previously unknown to us. This mode compares the actual location of markers on the chip to their expected location according to the layout and is able to correct for any distortions of the layout that occur during laser lithography by performing appropriate scale, shear and rotate operations on the layout before exposure. This way, we manage to achieve a sufficient and reproducible alignment between the different fabrication steps.

4.2. Experimental setup

The measurements of (flux-tunable) microwave resonators presented in Chap. 5 were done using standard continuous wave (CW) excitation schemes with a vector network analyzer (VNA). These measurements were performed in either a commercial TRITON dilution refrigerator by Oxford Instruments or a commercial Fast Sample Exchange dilution refrigerator by Bluefors at temperatures in the mK range. As both setups are conceptually the same regarding the measurements of microwave resonators, we are only going to explain in detail the setup in the TRITON refrigerator.

The measurements of the resonance frequency of a nanostring discussed in Chap. 6 require a more elaborate microwave spectroscopy scheme in addition to the continuous wave excitation with a VNA and were performed in the TRITON refrigerator as well. A schematic overview of the measurement setup is shown in Fig. 4.2.1. The sample (device under test, DUT) is mounted inside a sample box that is attached to the mixing chamber of the dilution refrigerator. An image of a sample inside a sample box is shown in Fig. 4.2.2. The input and output ports of the DUT are connected to the output and input of the VNA respectively via microwave cables. The signal path for the continuous wave microwave spectroscopy with the VNA is shown in blue in Fig. 4.2.1. The attenuation of in total $-70\,\mathrm{dB}$ on the input line, distributed over the various temperature stages of the cryostat, ensures that we can reach input powers equivalent to a few microwave photons and that no thermal photons from the parts of the setup at room temperature enter the device. Moreover, there is an additional attenuation due to cable losses of $-9.2\,\mathrm{dB}$ (not shown in Fig. 4.2.1). For the amplification of the outgoing microwave signal, we employ a low-noise cryogenic HEMT-amplifier with a gain of $40\,\mathrm{dB}$. After leaving the cryostat, the outgoing signal passes a circulator that prevents thermal noise from entering the cryostat via the output line. It is then amplified by a room-temperature amplifier with a gain of $28\,\mathrm{dB}$. After passing a directional coupler that becomes important for measuring the mechanical motion of the nanostring, it returns to the input port of the VNA. For each input frequency, the VNA measures the complex scattering parameter S_{21} (cf. Sec. 2.2.1) that contains information about the magnitude and phase of the transmitted output signal relative to the input signal. From this information, characteristic quantities of microwave resonators such as the resonance frequency, spectral linewidth and quality factors can be determined.

In order to exploit the flux tunability of the FTRs, we mount a coil, that is made from superconducting wire and generates an OOP bias flux Φ_{b}, on top of the sample

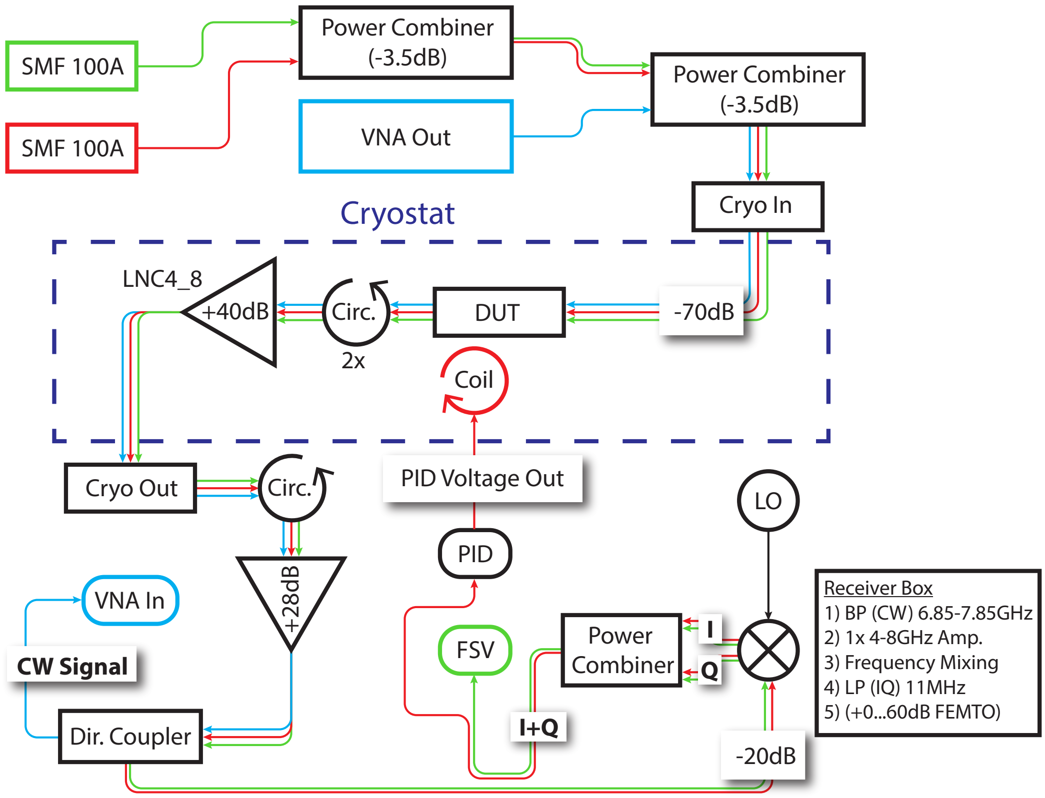

Figure 4.2.1.: Overview of the measurement setup. The complex transmission through the sample (device under test, DUT) is measured with a VNA (blue signal path). If the sample is a FTR, its resonance frequency can be tuned with a coil. For the measurement of the mechanical frequency of the nanostring, a microwave spectroscopy scheme is implemented (green signal path). A SMF100A microwave signal source probes the FTR on resonance and a spectrum analyzer (FSV) measures the sidebands generated by the mechanical motion. Prior to the measurement with the FSV, the signal is downconverted from GHz to MHz frequencies by heterodyne downconversion. The FTR is stabilized against flux noise by an active feedback control loop (red signal path).

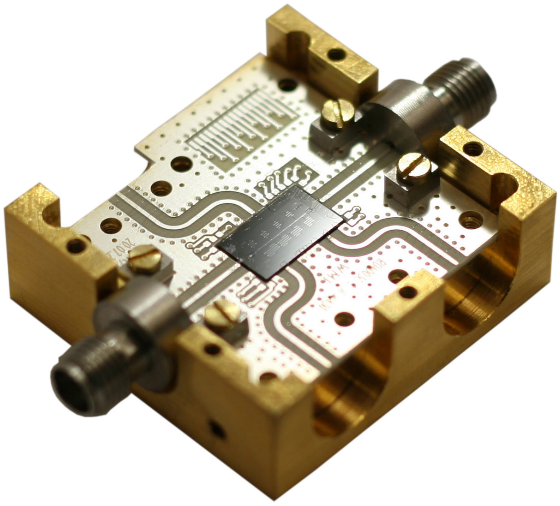

Figure 4.2.2.: Sample (rectangular chip in the middle) mounted inside a copper sample box. Microwave cables connect the VNA to the sample and are screwed onto microwave connectors. The pins of the microwave connectors lie on top of coplanar waveguides that are connected to the feedline of the device by wire bonds.

box. The applied OOP flux can then be controlled by the current sent through the coil. Furthermore, the sample is hosted inside a 3D-vector magnet that is used to apply the larger in-plane magnetic fields B_{IP}.

We implement a microwave spectroscopy scheme for the readout of the mechanical displacement noise spectral density by the following steps. An overview of the microwave tones and frequencies used in this spectroscopy scheme is given in Fig. 4.2.3. First, we determine the resonance frequency of the flux-tunable cavity $\omega_{\mathrm{c}}(\Phi_{\mathrm{b}})$ with a VNA as described above. With a SMF100A microwave signal source, we then apply a weak probe tone of frequency ω_{p} that is on resonance with the microwave cavity ($\omega_{\mathrm{p}} = \omega_{\mathrm{c}}(\Phi_{\mathrm{b}})$, green in Fig. 4.2.3). The probe tone must be resonant with the cavity in order to avoid unintended heating or cooling of the mechanics (cf. Sec. 2.1) and is incident on the sample sharing the same input line as the signal from the VNA. The corresponding signal path is shown in green in Fig. 4.2.1. When photons from the probe tone enter the microwave resonator and interact with the nanostring via the optomechanical interaction discussed in Sec. 2.1, they can scatter into the Stokes field at $\omega_{\mathrm{p}} - \Omega_{\mathrm{m}}$ and into the anti-Stokes field at $\omega_{\mathrm{p}} + \Omega_{\mathrm{m}}$. These scattering processes are schematically shown in Fig. 4.2.3. As explained below, we experimentally record the anti-Stokes field, which is indicated by the data acquisition window in Fig. 4.2.3.

After the interaction with the nanostring, the outgoing probe signal is coupled out by a directional coupler with an attenuation of $-20\,\mathrm{dB}$ and fed into the receiver box where a bandpass (BP) filter admits only frequency components from 6.85 GHz to 7.85 GHz that

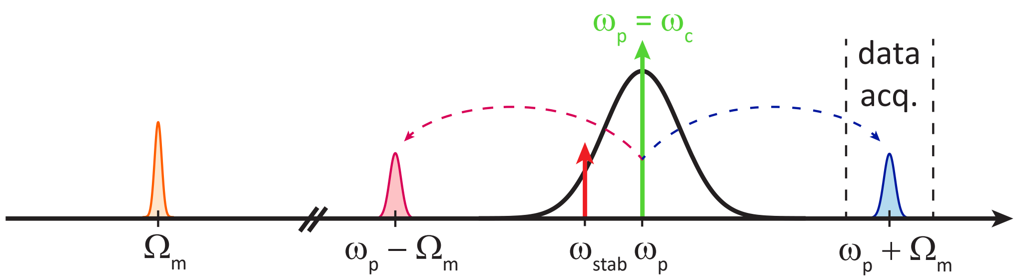

Figure 4.2.3.: Overview of the microwave tones and frequencies used in the spectroscopy scheme for the readout of the mechanical noise spectral density. A probe tone on resonance with the cavity ($\omega_\mathrm{p} = \omega_\mathrm{c}$) is sent into the device. Via Stokes (dashed arrow in magenta) and anti-Stokes processes (dashed arrow in blue), the mechanical motion generates two sidebands above and below the probe tone that are detuned by the mechanical frequency Ω_m. For the analysis of the mechanical properties, we record data of the blue-detuned sideband at $\omega_\mathrm{p} + \Omega_\mathrm{m}$. Moreover, a stabilizer tone is applied at ω_stab with the purpose to stabilize the cavity frequency against flux noise. Adapted from [31].

are subsequently amplified. Then, the Stokes and anti-Stokes fields are shifted from GHz to MHz frequencies by heterodyne downconversion. In this frequency mixing technique, the sidebands are mixed with a local oscillator (LO) at frequency $\omega_\mathrm{LO} = \omega_\mathrm{p} + \omega_\mathrm{IF}$ offset from the probe frequency ω_p by the intermediate frequency ω_IF [84]. Here, we choose an intermediate frequency of $\omega_\mathrm{IF}/2\pi = -3.5\,\mathrm{MHz}$. This results in an in-phase I and a quadrature Q signal that contain components at the sum (i.e. at $\omega_\mathrm{p} \pm \Omega_\mathrm{m} + \omega_\mathrm{LO}$) and the difference (i.e. at $\omega_\mathrm{p} \pm \Omega_\mathrm{m} - \omega_\mathrm{LO}$) of the sideband frequencies and the frequency of the LO. A low pass (LP) filter with a cut-off frequency at 11 MHz then suppresses the high frequency components in I and Q, such that only the low frequency components are left. Before being fed into the spectrum analyzer (FSV), the quadratures are amplified and added in a power combiner, which essentially returns the original Stokes and anti-Stokes fields, but now downconverted in frequency. Although the FSV is in principle able to measure signals in the GHz range, we make use of downconversion as it reduces the amount of data one needs to record and simplifies the LP filtering. With the FSV, we selectively measure the power spectral density (PSD) of the anti-Stokes field. The PSD indicates how much power the signal contains per 1 Hz around each frequency. The analysis of the frequency position of the anti-Stokes field with respect to the probe frequency allows to determine Ω_m. More detailed information on the frequency downconversion setup that we used in our measurements can be found in Ref. [85].

Furthermore, we have to implement an active feedback control loop in order to stabilize the flux-tunable cavity against flux noise. The corresponding signal path is shown in red in Fig. 4.2.1. This feedback loop is necessary because it is not possible to host the sample inside a magnetic shielding that protects it from magnetic field noise, as that would screen the external magnetic fields necessary for our experiments as well. We realize the feedback loop by applying a stabilizer tone at a frequency of $\omega_{\mathrm{stab}}/2\pi = \omega_{\mathrm{p}}/2\pi - 500\,\mathrm{kHz}$ (red in Fig. 4.2.3) with the second SMF100A power source. The stabilizer frequency is chosen such that it is located where the resonance dip of the cavity is steepest. Therefore, a relatively small change of the cavity frequency due to magnetic field noise leads to a relatively large change in the transmission of the stabilizer tone. The transmitted stabilizer tone is the input error signal for a PID controller that tries to keep the transmission of the stabilizer tone, and therefore the cavity frequency, constant. This is accomplished by generating a DC voltage output signal which controls a DC current source connected to the OOP flux coil on top of the sample.

Chapter 5.

Characterization of fixed-frequency and flux-tunable CPW resonators

This chapter is devoted to measurements of fixed-frequency and flux-tunable superconducting $\lambda/4$ CPW resonators. In Sec. 5.1, we first characterize fixed-frequency resonators on Tantalum (Ta) and Niobium (Nb) thin films in terms of their internal quality factors with and without external magnetic fields applied in the plane of the thin films. High quality superconducting thin films are an essential requirement for the fabrication of FTRs with internal quality factors on the order of 2×10^5, which is a necessary condition for reaching the single-photon strong coupling regime (cf. Chap. 3). In Sec. 5.2, we report on the optimization of the bandaging process with the aim of enhancing the internal quality factors of FTRs. In Sec. 5.3, we present measurements of FTRs patterned on Nb thin films. We compare their performance in terms of internal quality factors with fixed-frequency resonators, estimate the Kerr shift and investigate the frequency-tuning behavior.

5.1. In-plane field stability of CPW resonators on Ta and Nb

In this section, we report on measurements of fixed-frequency $\lambda/4$ superconducting CPW resonators on either Tantalum (Ta) or Niobium (Nb) thin films. The resonators' response to an external continuous excitation is probed with a VNA as explained in Sec. 4.2. From the complex S_{21} parameter, we extract quality factors for various input powers as well as for externally applied magnetic fields. The goal of these investigations is to find out whether our Ta and Nb thin films are suitable for the fabrication of FTRs and - by extension - inductively coupled nano-electromechanical devices, which require finite magnetic fields for their operation (see Sec. 2.3). In order to characterize the film quality of both the Ta and Nb films, we fabricate an identical layout with eight $\lambda/4$ CPW resonators on both of the substrates. All resonators are coupled capacitively to a shared feedline (cf. Fig. 3.0.2 (a)) and characterized using a standard microwave transmission spectroscopy

Table 5.1.1.: Resonance frequencies of CPW resonators made of Ta

Resonator	Resonance frequency (GHz)
R1	5.16
R2	5.40
R3	5.64
R4	5.89
R5	6.13
R6	6.62

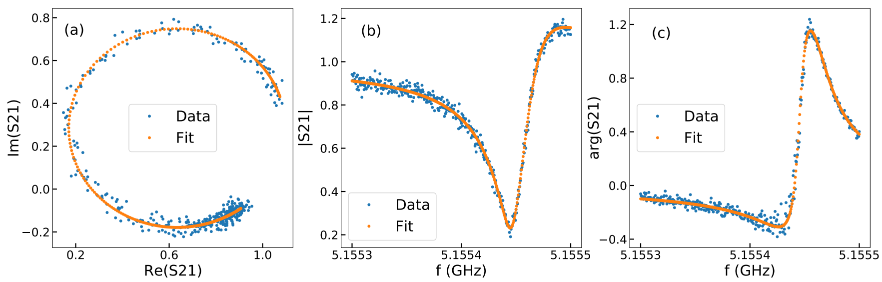

Figure 5.1.1.: Fit of transmission data of resonator 1 to the model for the complex S_{21} parameter given in Eq. 2.35. The input power at the sample was $-130.2\,\mathrm{dBm}$, corresponding to an average occupation of 290 microwave photons in the cavity. A fit of the resonance circle (a), the absolute value $|S_{21}|$ (b) and the phase of S_{21} (c) as a function of excitation frequency f are shown.

setup as described in Sec. 4.2. The resonators have different lengths, corresponding to nominal frequencies ranging from 5 GHz to 6.75 GHz in steps of 0.25 GHz.

CPW resonators on Tantalum In the experiment investigating the Ta thin film, only six of eight resonators could be identified as such using microwave spectroscopy. Their frequencies are given in Tab. 5.1.1. We note that while the spacing in frequency between the resonators is consistent with the designed value of 0.25 GHz, the absolute resonance frequencies deviate considerably from the designed values. This deviation probably stems from the Tantalum Nitride (TaN) seed layer on which the Ta film is grown, as it impacts the dielectric constant and therefore the resonance frequency according to Eq. 2.12.

The circle fit method presented in [47] allows us to determine the resonance frequencies and quality factors by fitting the complex S_{21} scattering parameter to the model given in Eq. 2.36. Plotting the imaginary versus the real part of Eq. 2.35 in the complex plane yields a circle known as the resonance circle. As the circle fit method takes into account the full complex transmission data, it is able to determine the resonator parameters more accurately than methods that make use of the absolute value of S_{21} only. A fit of the resonance circle, the absolute value $|S_{21}|$ and the phase of S_{21} as a function of frequency

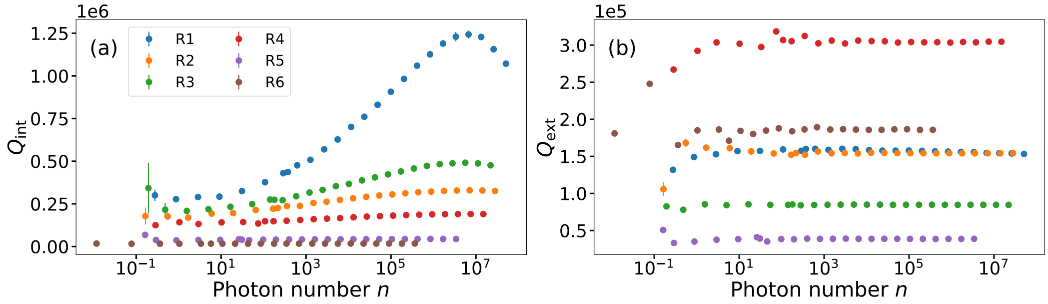

Figure 5.1.2.: Internal (a) and external (b) quality factors in zero external magnetic field for all six Ta microwave resonators as a function of the average photon number in the resonator.

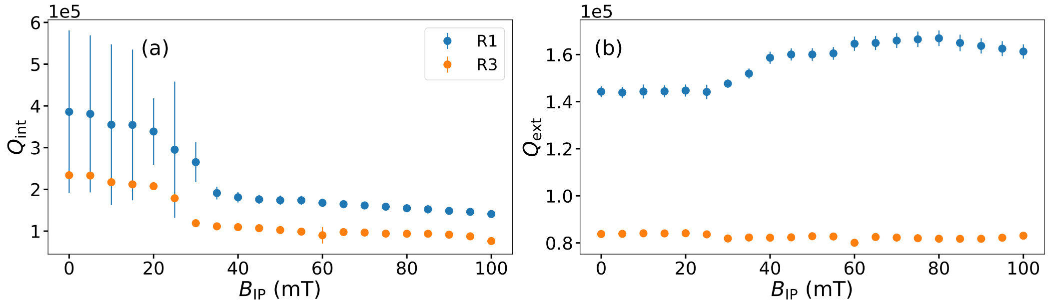

Figure 5.1.3.: Internal (a) and external (b) quality factor of resonator 1 and 3 in an external magnetic field $B_{\rm IP}$ applied in the thin film plane for constant input power at the sample of $-79.2\,$dBm corresponding to an average photon number of 2.2×10^7 for resonator 1 and 1.1×10^7 for resonator 3.

to Eq. 2.35 is shown in Fig. 5.1.1. There, the data was normalized in the sense that the influence of the environment onto the transmission was removed. We measured the microwave resonators for input powers at the sample from $-79.2\,$dBm to $-159.2\,$dBm in zero external magnetic field. The external and internal quality factors can be seen in Fig. 5.1.2, where the input power was converted into the mean number of photons in the resonator using Eq. 2.34. The internal quality factors show a different behaviour for the different resonators. While $Q_{\rm int}$ of R1 strongly increases with photon number, $Q_{\rm int}$ of R2 and R3 show a much weaker dependency on photon number and for the remaining three resonators $Q_{\rm int}$ barely changes with photon number. As discussed in Refs. [44, 77] and Sec. 5.2, this suggests that for R1 TLS are the dominant source of losses, whereas for resonators with higher frequency other loss mechanisms that do not saturate at high powers become more important. Such a significant frequency dependence of $Q_{\rm int}$ in Ta thin films has been repeatedly observed at the WMI.

We then went on to investigate the evolution of quality factors in an external magnetic field that we applied in the plane of the thin film using the 3D vector magnet surrounding the sample in the cryostat (cf. Sec. 4.2). The results for R1 and R3, the resonators with highest Q_{int} in zero field, can be seen in Fig. 5.1.3. These measurements were done at constant power of 0 dBm at the VNA output, corresponding to an average photon number of 2.2×10^7 for R1 and 1.1×10^7 for R3. Furthermore, the data was recorded in decreasing external field, such that at 0 mT, Q_{int} does not recover its value from the measurements in zero field due to the trapping of flux lines. While Q_{int} overall decreases with increasing field, a pronounced drop is visible around 30 mT. We suppose that this is a threshold field above which additional loss mechanisms play a role.

The above measurements show that our Ta thin films allow for CPW resonators with Q_{int} on the order of 3×10^5 in the single photon regime in zero external field. Also, they possess a decent field stability, as Q_{int} above 1.5×10^5 can be achieved in external in-plane fields up to 100 mT. Therefore, one might envisage fabricating FTRs with Q_{int} on the order of 2×10^5 on these films. As discussed in Chap. 3, this might be sufficient for realizing single photon strong coupling in our device. However, CPW resonators at frequencies above 6 GHz exhibit significantly lower Q_{int}, which would drastically limit the operating range of the FTR. We are not aware of the nature of the losses in our Ta thin films; but we suppose that the TaN seed layer on which the Ta films are grown contributes to them. Also, the losses might depend on the crystallographic phase of the thin films which is presently unknown to us. While in principle it is possible to fabricate superconducting qubits with coherence times exceeding 300 µs on Ta thin films [86], it is not trivial - and perhaps even impossible with our films - to fabricate CPW resonators with internal quality factors above 1×10^6 on Ta. In contrast, internal quality factors of CPW resonators on Nb thin films can reach values above 10^6 [78] and their fabrication has been heavily optimized at the WMI. For this reason, we focus from now on on resonators made from Nb thin films.

CPW resonators on Niobium Five CPW resonators on Nb thin films were measured in detail whose frequencies can be found in Tab. 5.1.2. In contrast to the resonators on Ta, the actual resonance frequencies agree well with the nominal values. As the Si substrate was cleaned by a HF dip before the sputtering of the Nb thin film, the interfaces between Si and Nb are supposedly very clean, which we think to be the reason for this good agreement.

As before, we make use of the circle fit routine for extracting internal and external quality factors from the complex S_{21} data. These are displayed for all five resonators as a function of photon number in zero external field in Fig. 5.1.4. Apparently, Q_{int} is substantially larger for the resonators on the Nb chip than on the Ta chip. In the single photon regime, Q_{int} of all resonators are comparable, ranging from 4.6×10^5 (R3) to 7.5×10^5 (R5). With increasing photon number, Q_{int} of R1 and R2 increase almost identically to 8.5×10^6 (R1) and 7.2×10^6 (R2) and show no sign of saturation. The

Table 5.1.2.: Resonance frequencies of CPW resonators made of Nb

Resonator	Resonance frequency (GHz)
1	4.99
2	5.23
3	5.48
5	5.98
6	6.23

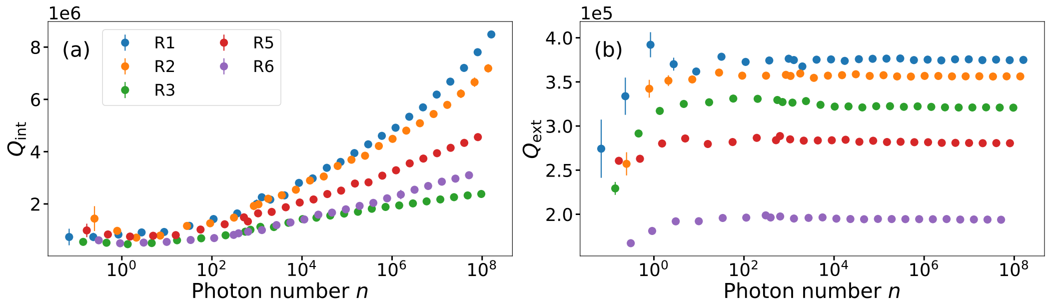

Figure 5.1.4.: Quality factors of standard microwave resonators patterned on Nb thin films as a function of the average photon number n inside the resonator.

other three resonators reach smaller Q_{int} at highest photon numbers of 2.4×10^6 (R3) 4.6×10^6 (R5) and 3.1×10^6 (R6). This indicates that Q_{int} of R1 and R2 is mainly dominated by TLS, whereas for the other resonators additional loss mechanisms seem to be of importance. For instance, the box in which we measured the resonator chip possesses a box mode at 7 GHz that might constitute such an additional loss channel for the resonators with higher frequencies.

Next, we investigated resonator 1, 2 and 3 in an external in-plane magnetic field of up to 75 mT. Each resonator was measured both in increasing and decreasing external field at a constant input power at the sample of −149.2 dBm that corresponds to an average resonator occupation of 4 to 10 photons, i.e. not too far away from the single photon regime we are ultimately interested in. Figure 5.1.5 shows Q_{int} of the three resonators for both increasing and decreasing external field. We find that Q_{int} is relatively stable over the whole field range and comparable to the value obtained from the measurements in zero external field. Moreover, Q_{int} deteriorates - if at all - only slightly when decreasing the field from 75 mT down to 0 mT. This remarkable field stability in combination with the inherently high Q_{int} at small photon numbers is very promising for the fabrication of FTRs and nano-electromechanical devices. As pointed out in Chap. 3, Q_{int} on the order of 2×10^5 would be necessary for the realization of the single-photon strong coupling regime in our previous devices. With the here presented Q_{int} of roughly 7.5×10^5 for the bare resonator in the single photon regime, $Q_{\mathrm{int}} = 2 \times 10^5$ seems to be reachable after the

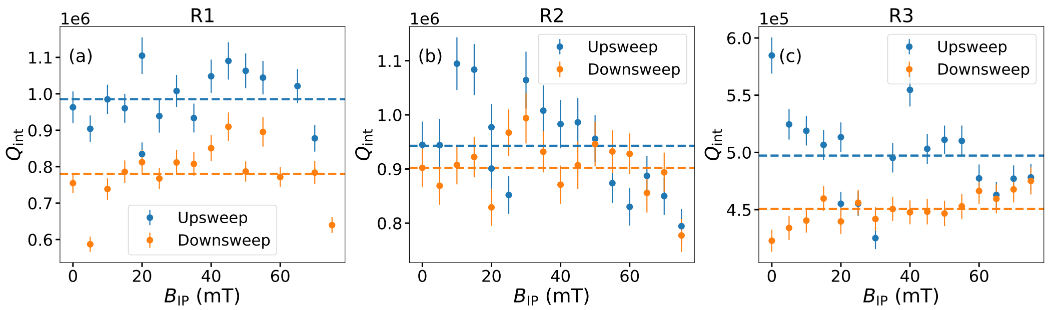

Figure 5.1.5.: Internal quality factor Q_{int} as a function of an external in-plane magnetic field B_{IP} for the three Nb resonators lowest in frequency. Q_{int} was measured for both increasing field (Upsweep) and decreasing field (Downsweep) at a constant input power of $-149.2\,\mathrm{dBm}$ at the sample, corresponding to an average cavity occupation of 4 to 10 photons. The horizontal dashed line indicates the average internal quality factor.

integration of the SQUID. For this reason, we choose to optimize design and fabrication of future devices based on Nb thin films.

5.2. Optimization of the bandaging process

As we will show in the next section, the internal quality factors of the first fabricated FTR are unexpectedly low. We suppose that the reason for this lies in the way we mill away the oxide on Al and Nb before the evaporation of bandages in order to establish galvanic contact between the components of the SQUID. If the Ar-ion milling is done too aggressively, Ar-ions might roughen the metal surfaces and be implanted into the metal. These defects might act as scattering centers for charge carriers or pinning centers for vortices. Since each vortex carries a magnetic flux of a flux quantum, a Lorentz force acts on the vortices when a current flows through the superconductor. This force induces dissipative vortex motion that constitutes an additional loss channel and hence reduces Q_{int} [87]. We expect substantial currents to flow close to the pinned vortices because the surfaces we treat with milling are located at the current antinode of the fundamental mode. Also, the fact that the same milling recipes work well for our in-house fabrication of superconducting qubits suggests that the given current distribution in FTRs makes them more susceptible to damages introduced by milling.

In order to optimize the milling recipe, we systematically vary relevant parameters of the Kaufman source that we use for Ar-ion milling (cf. Sec. 4.1). Comprehensive information on the functionality of a Kaufman source and its parameters can be found in Ref. [88]. Here, we fabricated a test chip with ten resonators that is shown in Fig. 5.2.1. Six of these resonators are initially $\lambda/2$ resonators with two open ends. We then bridge the gap at one of the ends by an Al bandage that is evaporated after milling with differ-

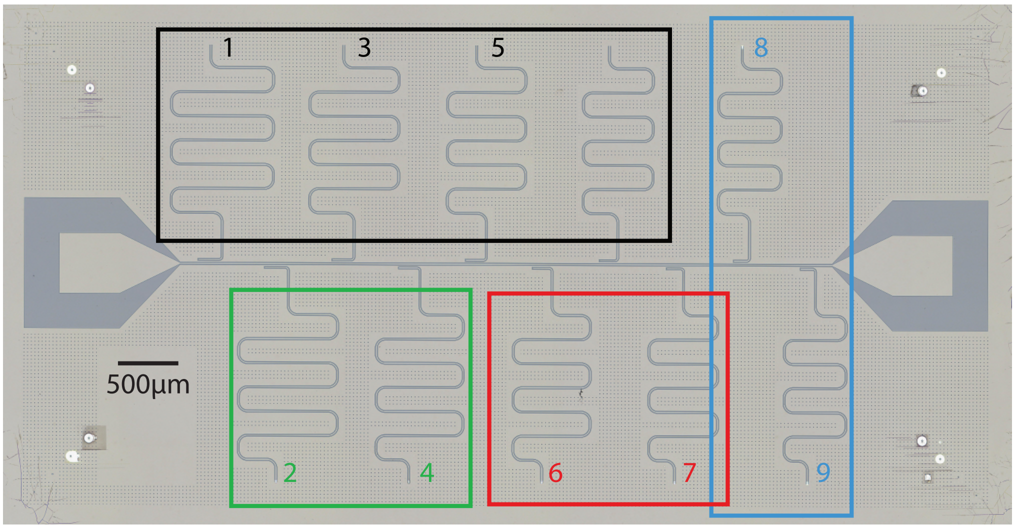

Figure 5.2.1.: Test chip for the optimization of the Ar-ion milling parameters for the bandaging process. The four resonators in the black box are standard $\lambda/4$ resonators. The other six resonators are shunted to ground at one of their ends by an Al bandage. Resonators in the same box were fabricated with the same milling recipe, given in Tab. 5.2.1.

ent parameters, turning the resonators into $\lambda/4$ resonators. Two adjacent resonators are fabricated using the same milling parameters, such that we are able to compare three different sets of milling parameters on one chip, given in Tab. 5.2.1. For comparison, the remaining four resonators on the chip are standard $\lambda/4$ resonators. In all three recipes, the beam voltage V_{beam} defining the beam energy and the acceleration voltage that forms the beam are kept constant. We vary the beam current I_{beam}, that is a measure for the number of Ar ions arriving at the target per second, from $I_{\text{beam}} = 15\,\text{mA}$ in recipe 1 and 2 to $I_{\text{beam}} = 30\,\text{mA}$ in recipe 3 and the milling time from 3 min in recipe 1 and 3 to 6 min in recipe 2.

For each resonator, we measure the complex microwave transmission parameter S_{21} defined in Eq. 2.36 as a function of excitation frequency at base temperature in a commercial cryostat for different input powers. The circle fit routine [47] allows us to extract the relevant resonator properties from the complex transmission data. The internal quality factors as well as the resonance frequencies for the nine resonators that were measured are shown in Fig. 5.2.2, where the input power was converted into the average number of photons inside the cavity using Eq. 2.34. As expected, the reference resonators without a bandage (resonators 1, 3 and 5, black symbols in Fig. 5.2.2) exhibit the highest internal quality factors, ranging from about 1.5×10^5 to 4×10^5. The observed increase of Q_{int} with increasing photon number n is characteristic for losses arising from the coupling to a bath of two-level systems (TLS), which get saturated at high input powers [77, 44]. This suggests that TLS are the main loss channel for the standard resonators.

Table 5.2.1.: Ar ion milling recipes for the test chip shown in Fig. 5.2.1. The numbering of resonators coincides with the numbers given therein.

Recipe	Resonator	V_{beam} (V)	I_{beam} (mA)	V_{acc} (V)	Milling time (min)
1	2, 4	400	15	90	3
2	6, 7	400	15	90	6
3	8, 9	400	30	90	3

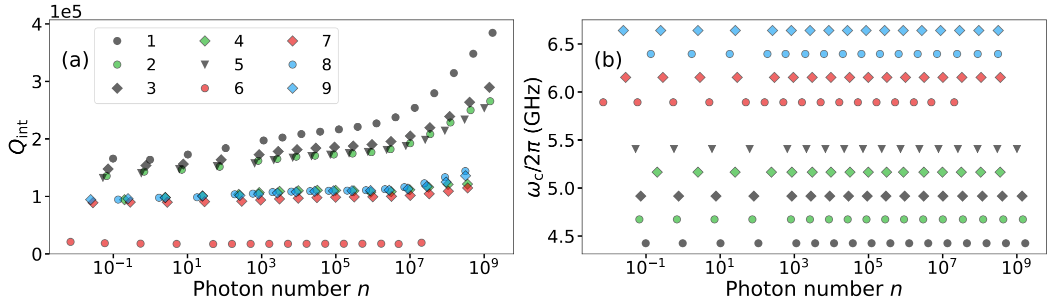

Figure 5.2.2.: (a) Internal quality factors Q_{int} and (b) resonance frequencies $\omega_{\mathrm{c}}/2\pi$ of the $\lambda/4$ microwave cavities fabricated using the milling recipes given in Tab. 5.2.1 as a function of the average number of photons n. Error bars are smaller than the symbol size.

Interestingly, resonator 2 features high Q_{int} as well that are comparable to those of the standard resonator 5. Again, we see an increase of Q_{int} with increasing photon number, indicating that the quality factor is limited by TLS as for the reference resonators. Resonator 4, which was fabricated with the same parameters as resonator 2, shows significantly smaller Q_{int} than resonator 2. We attribute this decline in Q_{int} to dirt (possibly resist residues) in the vicinity of the bandage. Resonators 8 and 9, for which I_{beam} was twice as large as for the other resonators, exhibit smaller Q_{int} on the order of 10^5 that are relatively constant over the range of applied input powers. This suggests that the dominant loss mechanism are no longer TLS but rather defects related to the milling process such as implanted Ar ions or missing metal atoms. Resonator 7, that was fabricated with a doubled milling time compared to the other resonators, shows similar Q_{int} to resonators 8 and 9, which means that once again the milling process limits Q_{int}. Resonator 6 however shows much smaller Q_{int} that are most likely due to a grain of dirt directly next to it. We see that for recipes 2 and 3 the product of beam current and milling time and therefore the number of ions that hit the target is the same. In contrast, for recipe 1 only half the number of ions hit the target. This means that for constant beam voltage (and therefore ion energy) the number of ions that reach the sample seems to be the relevant parameter that needs to be optimized.

The result of this milling optimization study can be understood intuitively as follows. After the optimal milling of the oxide layer, additional ions hitting the structures lead to a degradation of the metal surface and hereby to a decrease in Q_{int}. Therefore, a milling recipe with a lower number of ions reaching the surface seems to be favorable. However, we need to make sure that the milling process implemented within recipe 1 is sufficient to fully remove the oxide layer. An indication for such an incomplete milling process would be a power dependent shift of the microwave resonator's resonance frequency, as a residual oxide layer can be understood as a Josephson junction resulting in a microwave resonator with a Kerr nonlinearity (cf. Sec. 2.2.1). However, in Fig. 5.2.2 (b) we see that the resonance frequencies of all resonators stay constant over many orders of magnitude. This indicates that no oxide layer remains after the milling process and the devices still behave like linear harmonic oscillators. Hence, we conclude that for the study conducted here, a beam current of 15 mA and a milling time of 3 min lead to the highest internal quality factors.

Of course, these results leave room for a further optimization towards a shorter milling time until one observes a nonlinear behavior of the microwave resonators. Also, the optimization of other parameters such as the beam voltage might lead to improved internal quality factors as well.

5.3. Measurements of FTRs on Nb

We fabricated flux-tunable resonators (FTRs) on Nb thin films as explained in Sec. 4.1. In the following, we are going to present measurement results of two FTRs that we call sample 1 and sample 2. The samples are almost identical, with only minor differences in the device geometry and fabrication process.

Sample 1 For this sample, the RIE process was performed with a mixture of SF_6 and Ar^+-ions for a duration of 65 s. The Josephson junctions have a nominal width of 200 nm and the Dolan bridges of 50 nm. We let the JJ oxidize for 30 min and milled away the native oxide before bandaging for 6 min using recipe 2 from Tab. 5.2.1.

As with the measurements of the standard microwave resonators presented in the previous section, we measured the complex S_{21} parameter with a VNA. A color map of $|S_{21}|$ as a function of excitation frequency and different input powers at the sample is shown in Fig. 5.3.1 (a). The resonance signature of the FTR is visible as a dark blue curve. For increasing input powers, the resonance frequency of the FTR decreases. This is known as the Kerr shift (cf Sec. 2.2.1) and a characteristic of a nonlinear resonator. In our case, the nonlinear behaviour is due to the nonlinear inductance of the SQUID which gives rise to a nonlinear Duffing term in the equation of motion of the resonator's phase [24]. The shift of the resonance frequency becomes also apparent in the two linecuts taken at input powers of -120 dBm and -84 dBm and shown in Fig. 5.3.1 (b). In addition to

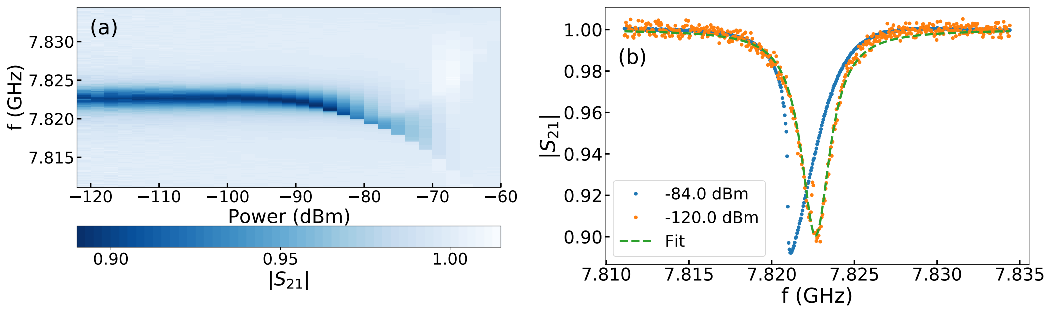

Figure 5.3.1.: (a) Microwave transmission spectroscopy of the FTR in zero external field. Shown is a color map of the absolute value of the scattering parameter $|S_{21}|$ as a function of excitation frequency f and different input powers at the sample. The resonance signature of the FTR is visible in darker blue. (b) Two line cuts at input powers of $-120\,\mathrm{dBm}$ and $-84\,\mathrm{dBm}$. At $-120\,\mathrm{dBm}$, the transmission data is fitted to Eq. 5.1. At $-84\,\mathrm{dBm}$, the Kerr shift of the resonance frequency and the asymmetry of the transmission around it become apparent.

the shift in resonance frequency, the transmission spectrum becomes asymmetric around the resonance frequency for increasing input powers. Again, this is a characteristic of a nonlinear Duffing oscillator [89]. This asymmetry increases with input power until eventually, the resonator becomes bistable and behaves hysteretically in the sense that the resonator's response is different for upsweeps and downsweeps of the excitation frequency. However, the hysteretic behaviour was not further investigated as the frequency was always swept in the same direction. More information on the Kerr nonlinearity in inductive nano-electromechanical systems can be found in Refs. [48, 90].

In the regime where the transmission spectrum of the FTR is still sufficiently symmetric, we fit the experimental $|S_{21}|$ data to a Lorentzian of the form

$$|S_{21}| = \left|1 - \frac{2\eta}{1 + 2i(f_{\mathrm{cav}}/\kappa)(f/f_{\mathrm{cav}} - 1)}\right|. \tag{5.1}$$

This is nothing but the absolute value of the complex transmission given in Eq. 2.35 for an ideal resonator without influence from the environment and without impedance mismatch (i.e. $\phi = 0$), where $2\eta = Q/Q_{\mathrm{ext}}$ and $f_{\mathrm{cav}}/\kappa = Q$. Here, it is justified to neglect the influence from the environment as we have normalized the data such that $|S_{21}| = 1$ far away from the resonance. The reason we do not make use of the circle fit routine is that the resonator operates in the strongly undercoupled regime due to its low internal quality factor. In this regime, the circle fit routine does not yield robust fit results due to convergence issues. With the relation $Q^{-1} = Q_{\mathrm{int}}^{-1} + Q_{\mathrm{ext}}^{-1}$, we can calculate Q_{int} of the FTR from the fitting results. Q_{int} of the FTR as a function of the average number of photons in the cavity is shown in Fig. 5.3.2 (b) and Q_{int} of the standard microwave

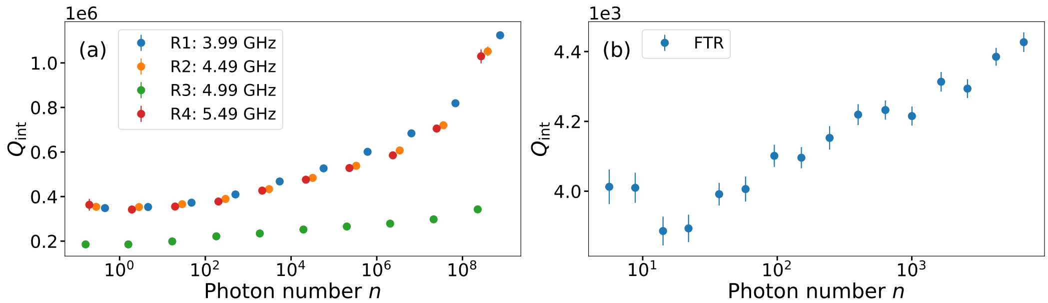

Figure 5.3.2.: Internal quality factors Q_{int} of the four standard resonators (a) and the FTR (b) on sample 1 as a function of average photon number n.

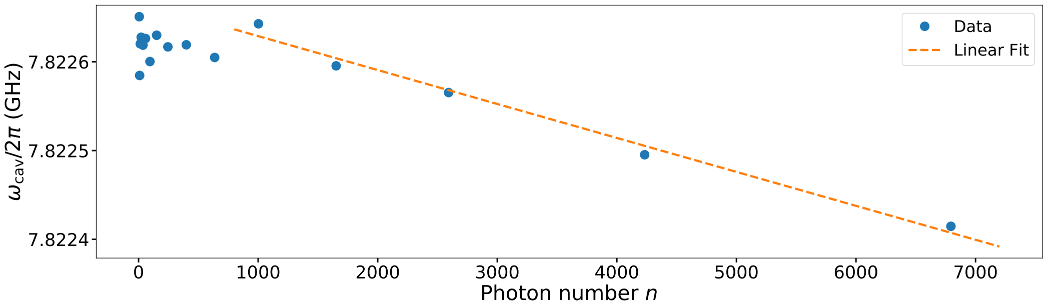

Figure 5.3.3.: Resonance frequency $\omega_{\text{cav}}/2\pi$ of the FTR on sample 1 as a function of the average number of photons n. The linear fit takes only the five data points to the right into account. Errorbars are smaller than the symbol size.

resonators Fig. 5.3.2 (a). As before, we have made use of the circle fit routine for the fitting of the standard resonators. They have good quality factors and show the expected behavior. With $Q_{\text{int}} \approx 4000$, the FTR has much lower quality factors than the standard resonators that have a Q_{int} of at least 1.8×10^5. We attribute these low internal quality factors to defects in the bandaged area introduced by the milling process (cf. Sec. 5.2). After the conversion of input powers to number of photons in the cavity with Eq. 2.34, we can quantify the Kerr shift per photon. The resonance frequency of the FTR as a function of photon number is shown in Fig. 5.3.3. By fitting a straight line to the five data points on the right, we get an estimate for the Kerr shift of -38 Hz per photon. In comparison to other reported values [28, 48], this is extremely small.

Now, we investigate the flux-tuning behavior of the FTR. To this end, we measure the complex transmission through the FTR with a VNA, while sending a current I of a few mA through the coil mounted on top of the sample box (cf. Fig. 4.2.1). In Fig. 5.3.4 (a), the absolute value of the scattering parameter $|S_{21}|$ is color coded as a function of excitation frequency and coil current. The resonance frequency of the FTR does change with coil current and therefore with the flux through the SQUID. Instead of continuous

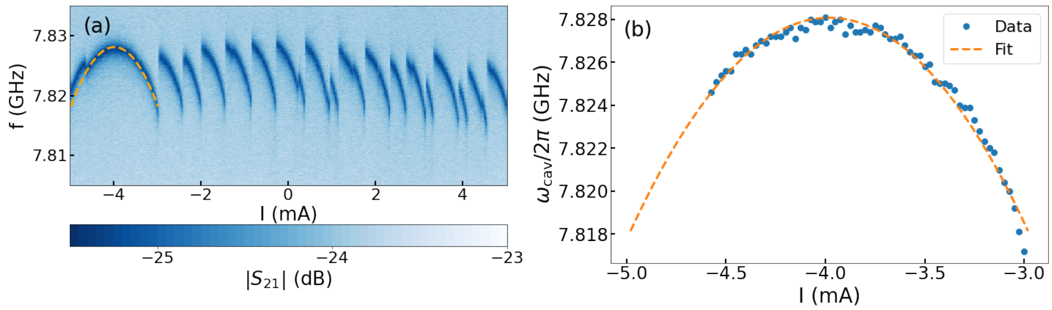

Figure 5.3.4.: Frequency tuning of the FTR on sample 1. Panel (a) shows the absolute value of the scattering parameter $|S_{21}|$ as a function of excitation frequency f and coil current I. The resonance frequency is met whenever the transmission is lowest (dark blue arcs). The dashed orange curve is the same as in the right panel. In panel (b), the resonance frequency $\omega_{\mathrm{cav}}/2\pi$ is plotted for coil currents around $-4\,\mathrm{mA}$. The dashed orange curve is a fit to Eq. 2.65 with the SQUID inductance from Eq. 5.2.

arcs as predicted by Eq. 2.65, the resonance frequency features jumps at certain values of the coil current. These jumps are a consequence of discontinuous transitions of the phase φ_- from one local minimum to an adjacent local minimum at certain values of the external flux and can only be seen in SQUIDs with sufficiently large screening parameter β_L [62]. Also, such a SQUID would show hysteresis, meaning that the flux values where the jumps occur differ for up- and downsweeps. Since rather large nonlinearity is to some degree desirable for electromechanical devices, hysteretic FTRs are common and in principle useable [27]. From the almost complete arc centered around $-4\,\mathrm{mA}$, we extract the critical current I_{c} by fitting to Eq. 2.65. Due to the discontinuities of the resonance frequency, an easy conversion from coil current to bias flux is not possible such that we use the following expression for the SQUID inductance

$$L_{\mathrm{S}} = \frac{\Phi_0}{4\pi I_{\mathrm{c}}\left|\cos\left(\pi\frac{k(I-I_0)}{\Phi_0}\right)\right|} = \frac{L_{\mathrm{s0}}}{\left|\cos\left(\pi\frac{k(I-I_0)}{\Phi_0}\right)\right|}. \tag{5.2}$$

Here, I_0 denotes the coil current where the bias flux vanishes (this is not necessarily the case at $I = 0\,\mathrm{mA}$) and k is a factor proportional to the ratio of bias flux and coil current. It is important to note that k is not equal to this ratio, as the inductance of a hysteretic SQUID for fluxes around zero bias flux reads [27]

$$L_{\mathrm{S}} = \frac{L_{\mathrm{s0}}}{\left|\cos\left(\pi\gamma\frac{\Phi}{\Phi_0}\right)\right|},$$

with a phenomenological parameter γ that accounts for a widening of the central flux arc beyond $\pm\Phi_0/2$. However, it is clear that when $k(I - I_0) = \pm\Phi_0/2$, the resonance frequency of the FTR reaches zero. This allows us to get an initial estimate for k by fitting the central arc of the resonance frequency to a quartic polynomial and determine its zeros. We then fit the central arc to Eq. 2.65 with the SQUID inductance as given in Eq. 5.2 for values of k in a range around the initial estimate with only I_c as free fit parameter (see the orange curve in Fig. 5.3.4). Finally, we take that value of k for which the deviation between fit and experimental data is minimal. The cavity inductance L_c of the CPW resonator, the loop inductance L_{loop} of the SQUID loop as well as the resonance frequency of the microwave cavity of $f_0 = 9\,\mathrm{GHz}$ are fixed by the geometry of the FTR in a first approximation. With a width of 10 µm and a gap of 6 µm for the CPW resonator, we obtain a line inductance of 430 nH/m using the software presented in Ref. [91]. Then, the cavity inductance equals 1.42 nH, as the length of the cavity is $l_c = 3.3\,\mathrm{mm}$. The loop inductance of the SQUID consists of two contributions, which are the geometric and the kinetic inductance. For the geometric inductance, we take a value of 19 pH from Ref. [28], as the geometry of our SQUID is very similar to the one used in this work. The kinetic inductance is due to the inertia of the Cooper pairs and therefore dominated by the long and thin nanostrings. It is proportional to the ratio l/A, where $l = 30\,\mu\mathrm{m}$ is the length of the nanostrings and $A = 200 \times 150\mathrm{nm}^2$ their cross section. The proportionality constant was found to be $4.5 \times 10^{-8}\mathrm{pH\,m}$ [28]. Thus, the kinetic inductance is $L_{kin} = 45\,\mathrm{pH}$ and the loop inductance $L_{loop} = 64\,\mathrm{pH}$.

With these values, the fit shown in Fig. 5.3.4 (b) yields a critical current of $I_c = 838\,\mathrm{nA}$, which corresponds to a critical current density of $2095\,\mathrm{A/cm}^2$. The critical current is comparable to the value found in [28], but much smaller than the value reported in [27]. Also, the screening parameter takes a value of $\beta_L = 0.05$, meaning that the FTR should not behave hysteretically and therefore the resonance frequency should not exhibit jumps. Of course, this is in clear contradiction to what we observe in the experiment. We believe that this unexpected behavior might be due to additional parasitic inductances that might form between bandages and Josephson junctions. As the overlap region is quite small, patches of oxide might remain after the milling that act as a Josephson junction introducing an additional inductance.

Sample 2 In contrast to sample 1, we performed the RIE process only with SF_6 for a duration of 165 s as this results in smoother Si surfaces (cf. Sec. 4.1). The nominal width of the Josephson junctions is 170 nm and of the Dolan bridges 150 nm. For these values, JJs were least likely to tear off during lift-off (cf. Sec. 4.1.2.) The oxidation time of the JJs was 75 min. For the milling step prior to bandaging, we used recipe 1 from Tab. 5.2.1, as this led to the highest Q_{int} on the test chip (cf. Sec. 5.2).

In the experiment, three standard resonators at 4.48 GHz, 4.97 GHz and 5.47 GHz and a FTR close to 7.1 GHz were found. The resonators' internal quality factors extracted

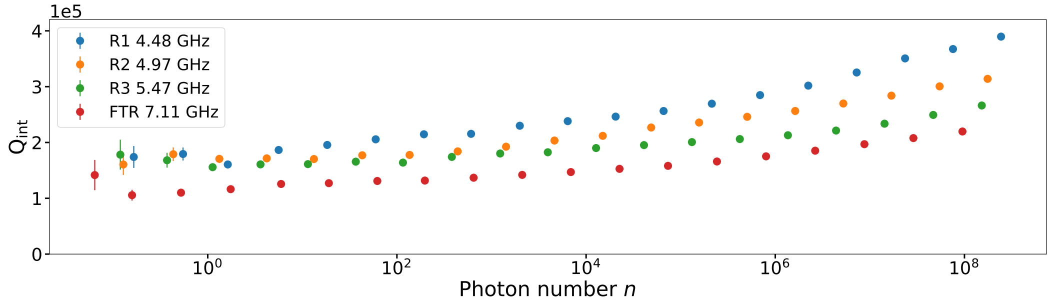

Figure 5.3.5.: Internal quality factors Q_{int} of three standard microwave resonators (R1 to R3) and the FTR on sample 2 as a function of photon number n.

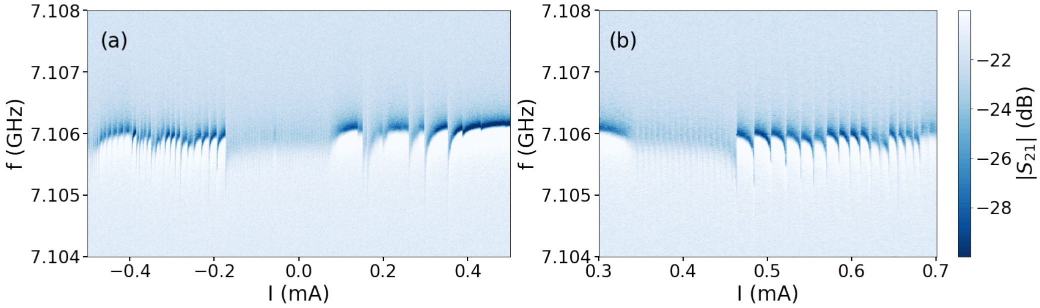

Figure 5.3.6.: Frequency tuning of the FTR on sample 2. The transmission $|S_{21}|$ as a function of excitation frequency f and coil current I is shown for downsweeps (left) and upsweeps (right) of the coil current. The resonance of the FTR is met at lowest transmission (dark blue arcs).

from the measurement of S_{21} are displayed in Fig. 5.3.5 as a function of photon number. The quality factors of the standard resonators depend only weakly on photon number and range from 1.5×10^5 to 3.9×10^5. They are therefore comparable to the ones of resonator 3 of sample 1 (cf. Fig. 5.3.2). The internal quality factor of the FTR lies between 1.0×10^5 and 2.2×10^5 and is thus only slightly below the quality factors of the standard resonators. Also, it is roughly 20 times larger than Q_{int} of the FTR on sample 1. We attribute this improvement of Q_{int} partly to the different milling recipe used for this sample. But as one can see from Fig. 5.2.2 (a), milling recipe 1 is expected to improve Q_{int} only by a factor of 1.5 to 2.5 over milling recipe 2. Therefore, there must be an additional cause for the greatly enhanced Q_{int} of the FTR. We note that these quality factors correspond to an internal loss rate of at most $\kappa_{\mathrm{int}} = 71\,\mathrm{kHz}$. In a device with released strings, this loss rate would bring us quite close to the single-photon strong coupling regime if $g_0 = 55\,\mathrm{kHz}$ demonstrated in the previous device generation can be reproduced.

We now turn our attention to the frequency tuning behaviour of the FTR in Fig. 5.3.6, where the absolute value of the transmission $|S_{21}|$ is shown as a function of excitation frequency and coil current. As for the FTR on sample 1, the resonance frequency exhibits a series of jumps. Interestingly, the distance between neighbouring jumps is not constant. Instead, there are current ranges where the jumps have a rather large spacing (e.g. for coil currents above 0.5 mA in Fig. 5.3.6(b)) or a rather small spacing (e.g. for coil currents around 0.4 mA in Fig. 5.3.6(b)). The tuning depth of the FTR of about 1 MHz is roughly 10 times smaller than for the FTR on sample 1. We think that this reduced tuning depth renders the FTR more insensitive to flux noise, which might contribute to the enhanced internal quality factor. Furthermore, we observe that the FTR behaves hysteretically as the orientation of the truncated resonance frequency arcs inverts from a downsweep in Fig. 5.3.6 (a) to an upsweep in Fig. 5.3.6 (b) of the current.

Outlook We conclude that we were able to achieve a major improvement of the internal quality factors of the FTRs from sample 1 to sample 2 by optimizing the milling recipe for the bandages. The FTR on sample 2 exhibits an internal quality factor close to the target value that would be necessary for reaching the single-photon strong coupling regime. However, the frequency tuning behavior showing signatures of hysteresis in spite of a sufficiently small critical current for the FTR on sample 1 as well as the unusually small Kerr shift of that FTR suggest that the current design needs to be further optimized. The complex frequency tuning behavior of the FTR on sample 2, which is even in the context of hysteretic FTRs not fully understood, seems to confirm this assumption. As we believe that the hysteretic behaviour might be due to parasitic inductances forming between bandages and JJs, a reasonable modification would be to significantly enlarge the overlap between them. Once the fabrication of a FTR with a suitable frequency tuning behavior succeeds, the next step would be to release the nanostrings and investigate the interplay of mechanical motion and microwaves in this nano-electromechanical device.

Chapter 6.

Measurement of mechanical frequency shift

In this chapter, we present measurements of the mechanical frequency of a nanostring embedded into the SQUID-loop of a flux-tunable superconducting microwave resonator. The device on which these measurements were performed was made by Philip Schmidt and introduced in Chap. 3. Here, we investigate the fundamental out-of-plane mechanical mode whose motion is transduced to a flux change by an in-plane (IP) magnetic field B_{IP} (see Sec. 2.3). In a previous study [31], it was found that the resonance frequency of the nanostring can be tuned via the backaction mediated by the Lorentz force. This behavior is theoretically well understood [26] and the corresponding theory was presented in Sec. 2.4.1. In addition to this expected evolution of the mechanical frequency Ω_{m} with bias flux Φ_{b} and in-plane field B_{IP}, a residual shift of the uncoupled mechanical frequency Ω_0 with B_{IP} was observed. As mentioned in Sec. 2.4.2, the most likely origin of this residual frequency shift seems to be the coupling between the flux lines penetrating the nanostring and the mechanical motion of the nanostring. Here, we are going to further investigate this hypothesis. In Sec. 6.1, we describe how we acquire the data for the mechanical frequency Ω_{m} as a function of bias flux Φ_{b} for a given B_{IP}. In Sec. 6.2, we analyze this data in terms of the two models for the mechanical frequency presented in Sec. 2.4.1 and explain how we extract the uncoupled mechanical frequency Ω_0. We close this chapter with a discussion of the results for Ω_0 as a function of B_{IP} in Sec. 6.3.

6.1. Data acquisition

The measurements of the mechanical frequency of a nanostring inductively coupled to a FTR were performed using the heterodyne downconversion spectroscopy scheme described in Sec. 4.2. We measure the mechanical frequency for different B_{IP} that contribute to the coupling strength g_0 between FTR and nanostring according to Eq. 2.71. For each B_{IP}, we first record the transmission S_{21} through the FTR as a function of excitation

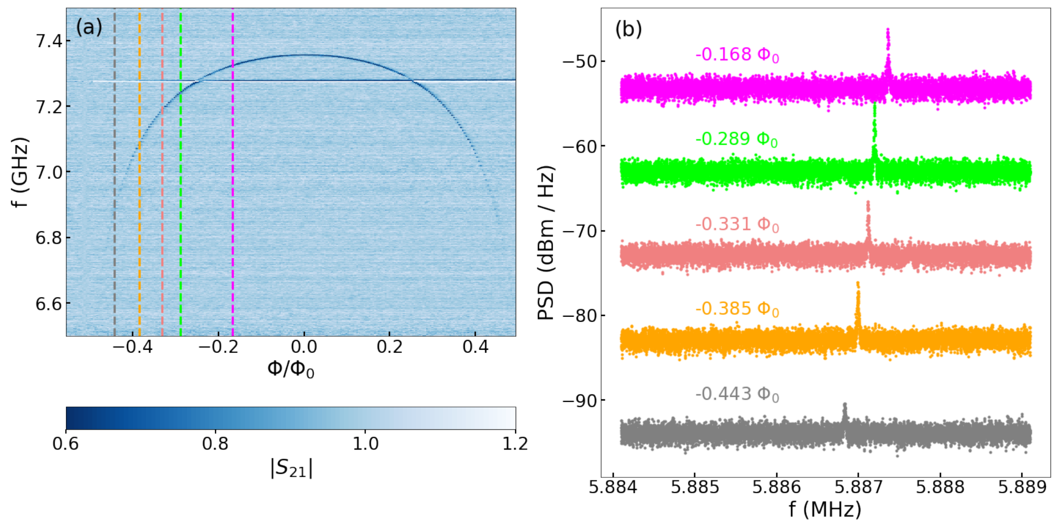

Figure 6.1.1.: Panel (a) shows a color map of $|S_{21}|$ as a function of excitation frequency f and normalized bias flux Φ/Φ_0 at $B_{\mathrm{IP}} = 28\,\mathrm{mT}$. The resonance frequency of the FTR is met when $|S_{21}|$ is minimal (dark blue arc) and is tunable via the bias flux in a range from 6.80 GHz to 7.36 GHz. Close to 7.30 GHz a parasitic mode is present that probably stems from a non-tunable resonator on the chip. For the measurement of the mechanical frequency, we operate the FTR at different bias flux working points indicated by the dashed colored lines. At each working point, we measure the PSD of the outgoing microwave signal, shown in panel (b). The sideband created by the mechanical motion is visible as a peak in the PSD. For clarity, each PSD is offset from the previous one by 10 dBm/Hz. The colors correspond to the ones in panel (a).

frequency and current flowing through the coil that is mounted on top of the sample. The coil current generates an out-of-plane magnetic field and therefore a bias flux Φ_{b}. The conversion from coil current to bias flux is easily done since we know that the periodicity of the FTR's resonance frequency is given by Φ_0. A color map of $|S_{21}|$ (the so-called frequency tuning map) is shown in panel (a) of Fig. 6.1.1. The excitation frequency equals the resonance frequency of the cavity when $|S_{21}|$ is minimal, indicated by the dark blue arc. As this frequency changes with Φ_{b}, we can confirm that the microwave resonator is flux-tunable. For the microwave spectroscopy, we choose different working points (i.e. different resonance frequencies of the FTR) by setting the coil on top of the sample box to the corresponding current. In panel (a) of Fig. 6.1.1, five different working points are denoted by dashed colored lines. Unlike shown in this figure, we usually measure at at least one working point to the right of the maximal FTR frequency. This is important for more reliable fits when analyzing the data. At each working point, we send a probe tone of varying input power on resonance with the FTR into the system and measure the voltage power spectral density (PSD) of the outgoing microwave signal with a spectrum analyzer (cf. Sec. 4.2). We do not drive the mechanical mode under investigation such that the sideband in the PSD is due to the thermal motion of the nanostring. Before measuring the PSD, the transmission of the FTR is probed again in order to know its resonance frequency precisely. The precise knowledge of the FTR's resonance frequency is needed in order to determine the exact bias flux corresponding to this resonance frequency. To this end, we remove the background signal from the recorded frequency tuning map by dividing the raw S_{21} data for each coil current by a S_{21} data set at a coil current where the FTR resonance is not visible and remove noise by a simple moving average filter. After converting coil current to bias flux, this yields a frequency tuning map like the one shown in Fig. 6.1.1 (a). For each bias flux, we then search for the frequency where $|S_{21}|$ becomes minimal and take this frequency as the resonance frequency of the FTR. Finally, we interpolate between the data points obtained like this with cubic splines. The resulting interpolation function allows us to convert a given resonance frequency of the FTR to the corresponding bias flux.

For the data analysis, we select an input power where the sideband that is created by the mechanical motion is clearly visible. However, the selected power must not be too high in order to ensure that the mechanical frequency is not affected by unwanted sideband cooling or heating. Such a shift of the mechanical frequency due to the optomechanical interaction is known as the optical spring effect [1]. Panel (b) of Fig. 6.1.1 shows the PSD when operating the device at the working points indicated in Fig. 6.1.1 (a). From the working point at $\Phi_\mathrm{b}/\Phi_0 = -0.443$ to the working point at $\Phi_\mathrm{b}/\Phi_0 = -0.168$, the mechanical frequency shifts by 600 Hz, which corresponds to about 38 times the mechanical linewidth. This frequency shift is a consequence of backaction based on the Lorentz force and was studied in detail in [31]. In order to extract the mechanical resonance frequency Ω_m and the mechanical damping rate Γ_m, we fit the PSD S_{VV} for each working point to a Lorentzian of the form

$$S_{VV}(\Omega) = a\frac{2\Gamma_\mathrm{m}}{(\Omega^2 - \Omega_\mathrm{m}^2)^2 + \Gamma_\mathrm{m}^2\Omega^2} + b. \tag{6.1}$$

The parameter b accounts for the noise floor and a is the proportionality constant between the displacement noise spectral density and the PSD of the microwave signal. A fit of the PSD at $B_\mathrm{IP} = 28\,\mathrm{mT}$ and $\Phi_\mathrm{b}/\Phi_0 = -0.331$ to this equation is shown in Fig. 6.1.2 (a). Panel (b) of Fig. 6.1.2 displays the mechanical resonance frequency as a function of normalized bias flux Φ_b/Φ_0 for three different B_IP. We observe that $\Omega_\mathrm{m}/2\pi$ changes with bias flux and increases with increasing in-plane field. This behaviour is qualitatively predicted by Eq. 2.78 and by Eq. 2.83 for sufficiently small β.

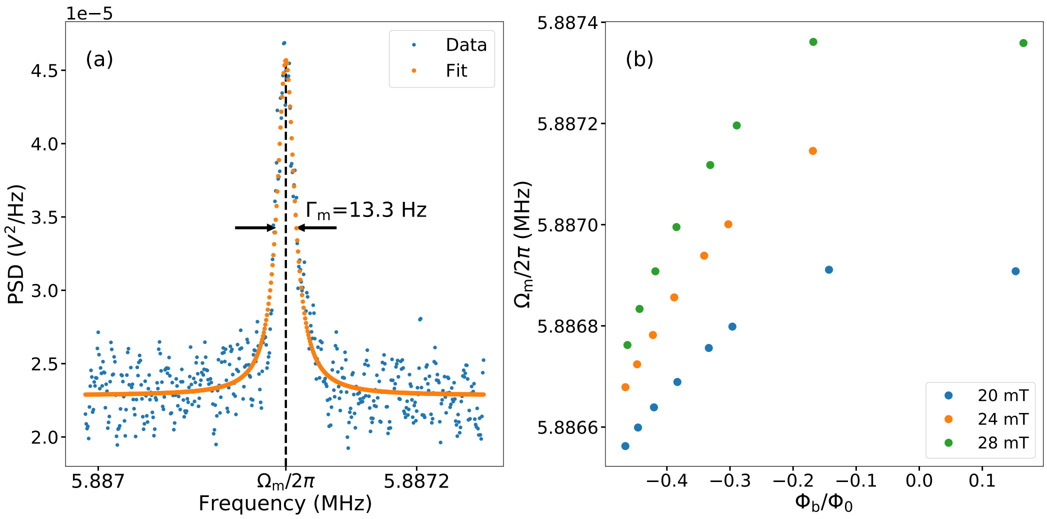

Figure 6.1.2.: (a) A fit of the PSD at $B_{\mathrm{IP}} = 28\,\mathrm{mT}$ and $\Phi_b/\Phi_0 = -0.331$ to Eq. 6.1. From the fit, we obtain a mechanical resonance frequency of $\Omega_m/2\pi = 5.887\,12\,\mathrm{MHz}$ and a mechanical damping rate of $\Gamma_m/2\pi = 13.3\,\mathrm{Hz}$. (b) The mechanical resonance frequency at different bias fluxes and in-plane fields of 20 mT, 24 mT and 28 mT. We see that the tuning range increases with increasing B_{IP} from 350 Hz at 20 mT to 600 Hz at 28 mT. Errorbars are smaller than the symbol size.

6.2. Data analysis

We performed measurements of the mechanical resonance frequency at in-plane fields from $B_{\mathrm{IP}} = 12\,\mathrm{mT}$ to $B_{\mathrm{IP}} = 30\,\mathrm{mT}$ at various flux bias points. We extracted the mechanical resonance frequency $\Omega_m/2\pi$ from the measured data as explained in Sec. 6.1. It is then possible to fit this experimental data to the models introduced in Sec. 2.4.1. For all fits shown in this section, we made use of *lmfit*, a *Python* package for nonlinear optimization and curve fitting.

Figure 6.2.1 shows a fit of experimental data at in-plane fields of 20 mT, 26 mT and 30 mT to Eq. 2.78 (panel (a)) and Eq. 2.83 (panel (b)). We see that both models are in principle able to reproduce the experimentally observed shift of $\Omega_m/2\pi$, as all fits agree well with the experimental data. Concerning the fitting itself, we note that Eq. 2.78 and Eq. 2.83 contain parameters that we know and therefore can fix in the fit and parameters that we do not know precisely and therefore leave as free fit parameters. For the latter, we can make a reasonable guess and set boundaries, such that in the fitting process, the values of the fit parameters are optimized within these boundaries. For both models, parameters we fix in the fit are the external field $B = B_{\mathrm{IP}}$, the geometry factor $\lambda = 0.9$, the length of the nanostring $l = 30\,\mu\mathrm{m}$ and its effective mass $M_r = 0.9\,\mathrm{pg}$. For the model in Eq. 2.78 that considers an asymmetric SQUID, we additionally fix the asymmetry $\alpha = 0.01$, although it is in principle not known to us. However, $\alpha = 0.01$ is

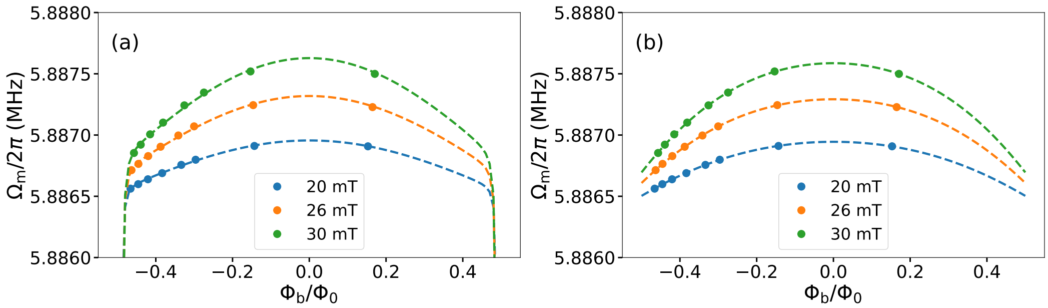

Figure 6.2.1.: Experimental data (dots) of the mechanical frequency at three different in-plane fields versus bias flux and fits (dashed lines) to the model from Ref. [26] given in Eq. 2.78 (panel (a)) and our model given in Eq. 2.83 (panel (b)). Errorbars are smaller than the symbol size.

Table 6.2.1.: Results of the fits shown in Fig. 6.2.1. The first value corresponds to the fit to Eq. 2.78 and the second value to the fit to Eq. 2.83. The following parameters were fixed in the fit: $l = 30\,\mu\text{m}$, $M_\text{r} = 0.9\,\text{pg}$, $\lambda = 0.9$, $\alpha = 0.01$.

Fit Parameter	$B_\text{IP} = 20\,\text{mT}$		$B_\text{IP} = 26\,\text{mT}$		$B_\text{IP} = 30\,\text{mT}$	
$\Omega_0/2\pi$ (MHz)	5.88655	5.88642	5.88668	5.88644	5.88678	5.88646
I_0 (nA)	194	565	178	561	177	557
L_loop (pH)	-	80	-	99	-	103

a reasonable value to account for small deviations in fabrication and worked well for the analysis of data measured on the same sample in Ref. [31]. Then, only Ω_0 and the critical current I_0 remain as free fit parameters. For these, we make inital guesses of $\Omega_0^\text{init}/2\pi = 5.887\,\text{MHz}$ and $I_0^\text{init} = 200\,\text{nA}$. The model in Eq. 2.83 considering a SQUID with finite loop inductance takes one additional free fit parameter, which is the loop inductance L_loop. For the free fit parameters, we make initial guesses of $\Omega_0^\text{init}/2\pi = 5.887\,\text{MHz}$, $I_0^\text{init} = 600\,\text{nA}$ and $L_\text{loop}^\text{init} = 100\,\text{pH}$. The best values for the fit parameters corresponding to the fits in Fig. 6.2.1 can be found in Tab. 6.2.1.

Although it would be possible to determine the uncoupled mechanical frequency $\Omega_0/2\pi$ this way for all in-plane fields, this is not the approach we pursue here. The reason is that we want to determine $\Omega_0/2\pi$ as accurately as possible in order to verify whether it shows discontinuous, step-like evolution with B_IP. To this end, we try to determine I_0 (and L_loop for our model) independently from a fit of the resonance frequency of the flux-tunable cavity as a function of bias flux and plug the resulting values into the fit of the mechanical frequency.

Lumped-element model We start by fitting the resonance frequency of the FTR to the lumped-element model given in Eq. 2.56, where we assume $\alpha = 0.01$ and ω_{c0} is the only fit parameter. Since this model is derived under the same assumptions that led to Eq. 2.78,

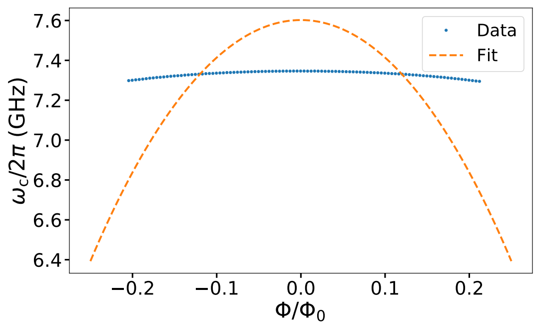

Figure 6.2.2.: Resonance frequency of the flux-tunable cavity as function of bias flux Φ/Φ_0 at $B_{\mathrm{IP}} = 30\,\mathrm{mT}$ and fit to Eq. 2.56. Clearly, this fit does not converge to a useful representation of the experimental data.

it should be consistent with that equation for the mechanical frequency. An exemplary fit to this model at $B_{\mathrm{IP}} = 30\,\mathrm{mT}$ is shown in Fig. 6.2.2. As the fit does not at all converge to a result matching the experimental data, we conclude that the lumped-element model does not describe our device correctly. The fundamental problem with this model is that it neglects the cavity inductance of the CPW as well as the loop inductance of the SQUID. Instead, the only fit parameter ω_{c0} (the maximal frequency of the cavity) does not affect the curvature of the fit which depends only on S_0. Therefore, it is impossible to fit this model to our data.

Distributed-element model Next, we fit the resonance frequency of the FTR for all in-plane fields to the distributed-element model given in Eq. 2.65. For the geometry of the FTR under investigation, we obtain a line inductance of $L_0 = 468\,\mathrm{nH/m}$ with the software presented in [91]. Given the physical length of the CPW of $d = 3.95\,\mathrm{mm}$, this results in a cavity inductance of $L_{\mathrm{cav}} = L_0 d = 1.8486\,\mathrm{nH}$. We obtain a resonance frequency of the bare cavity of $\omega_0/2\pi = 7.5985\,\mathrm{GHz}$ using the same software. The loop inductance of the SQUID is the sum of the geometric and the kinetic inductance: $L_{\mathrm{loop}} = L_{\mathrm{geo}} + L_{\mathrm{kin}}$. For the geometric inductance, we take a value of $L_{\mathrm{geo}} = 28\,\mathrm{pH}$ [60]. The kinetic inductance is dominated by the long and thin nanostrings of length $l = 30\,\mu\mathrm{m}$ and is proportional to l/A, where $A = 200 \times 110\mathrm{nm}^2$ is the cross section of the nanostrings. The proportionality constant was found to be $4.5 \times 10^{-8}\mathrm{pH\,m}$ [28], leading to a kinetic inductance of $61.3\,\mathrm{pH}$ and thus a total loop inductance of $L_{\mathrm{loop}} = 89.3\,\mathrm{pH}$. In general, the kinetic inductance depends on the current flowing through the device. According to [42], it can be expanded to lowest order as

$$L_{\mathrm{kin}}(I) = L_{\mathrm{kin}}(0)\Big(1 + \frac{I^2}{I_2^2} + \dots\Big), \tag{6.2}$$

where $L_{\mathrm{kin}}(0)$ is the kinetic inductance for vanishing current and I_2 a parameter on the order of the critical current. This means that in an external magnetic field, the kinetic inductance is expected to increase quadratically with B due to the presence of screening currents proportional to B [85]. However, we do not know the parameter I_2 and the above value for L_{loop} is merely a rough estimate, as it takes only the contribution of the nanostrings to the kinetic inductance into account. Therefore, we do not fix L_{loop} but leave it as a fitting parameter for all in-plane fields. In principle, the cavity inductance L_{cav} increases with external magnetic field as well due to a kinetic contribution. However, this effect should be negligible in comparison to the geometric contribution to L_{cav}. More specifically, the relative change of the resonance frequency of the bare cavity when applying an external magnetic field B is

$$\frac{\omega_0(B)}{\omega_0(0)} \approx 1 - \frac{1}{2}\frac{\Delta L_{\mathrm{cav}}}{L_{\mathrm{cav}}} \approx 1 - k(T)B^2,$$

where L_{cav} is the cavity inductance at zero field and ΔL_{cav} the change in cavity inductance due to an external field [92, 85]. The temperature-dependent proportionality factor $k(T)$ was found to be smaller than $0.1\,\mathrm{T}^{-2}$ at the temperatures where we perform our experiments [85]. With applied fields between $12\,\mathrm{mT}$ and $30\,\mathrm{mT}$, the correction to the bare cavity frequency as well as the relative change in cavity inductance is on the order of 10^{-5} and therefore negligible.

In order to fit the resonance frequency of the FTR to Eq. 2.65, we proceed as follows. For each B_{IP}, we fix L_{cav} to the above value and leave L_{loop} and the critical current I_0 as free fit parameters. In a fit to the resonance frequency in zero external field, we also leave the bare cavity frequency $\omega_0/2\pi$ as a free fit parameter and then fix it for all finite B_{IP} to the value obtained from the fit at zero field. A fit of the FTR resonance frequency at $B_{\mathrm{IP}} = 0\,\mathrm{mT}$ and $B_{\mathrm{IP}} = 30\,\mathrm{mT}$ is shown in Fig. 6.2.3. We see that the model reproduces the experimental data accurately for both fields. The corresponding values for the fit parameters are given in Tab. 6.2.2. This means that our flux-tunable cavity is well described by the model of a flux-tunable distributed-element resonator given in Eq. 2.65. In particular, it is essential to take the cavity inductance L_{cav} into account in order to reproduce the experimental data.

From these fits, we can then extract the values of the critical current I_0 and the loop inductance L_{loop} for all in-plane fields. From Eq. 2.42 and Eq. 6.2 we expect a quadratic decrease of I_0 and a quadratic increase of L_{loop} for small B_{IP}. I_0 and L_{loop} as a function of B_{IP} together with quadratic fits are shown in Fig. 6.2.4. We observe an overall decrease of I_0 with B_{IP} that agrees quite well with the expected quadratic behavior. In contrast, the evolution of the loop inductance shows a slightly decreasing trend from zero field to $12\,\mathrm{mT}$ and then increases for larger B_{IP}. For the data presented here, we

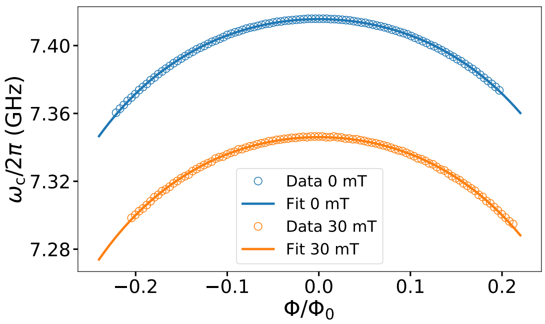

Figure 6.2.3.: Extracted resonance frequency of the flux-tunable cavity $\omega_c/2\pi$ as function of bias flux $\Phi_/\Phi_0$ for in-plane fields of 0 mT and 30 mT. Solid lines are fits to Eq. 2.65.

Table 6.2.2.: Parameters for the fits to the model Eq. 2.65 shown in Fig. 6.2.3. The resonance frequency of the bare cavity $\omega_0/2\pi$ is a free fit parameter at vanishing in-plane field only and fixed for finite in-plane fields. For both fits, we fixed L_{cav}, as it is given by the geometry in a first approximation.

Fit Parameter	$B_{IP} = 0\,\mathrm{mT}$	$B_{IP} = 30\,\mathrm{mT}$
$\omega_0/2\pi$ (GHz)	7.6686	7.6686
L_{cav} (nH)	1.8486	1.8486
L_{loop} (pH)	59.0	118.6
I_0 (µA)	3.406	3.196

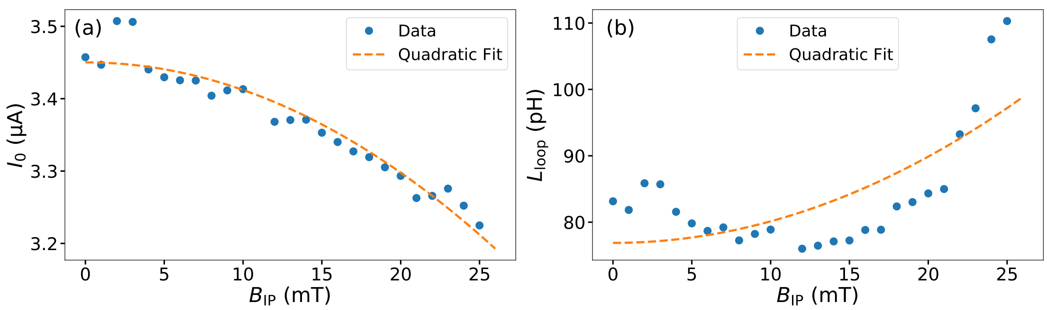

Figure 6.2.4.: (a) Critical current I_0 and (b) loop inductance L_{loop} versus magnetic in-plane field B_{IP}. I_0 and L_{loop} were extracted from fits of resonance frequency of the flux-tunable cavity to Eq. 2.65 (see Fig. 6.2.3). Dashed lines are a quadratic fit to the data as expected from Eq. 2.42 for I_0 and Eq. 6.2 for L_{loop}. Error bars due to statistical fit uncertainties are smaller than the symbol size.

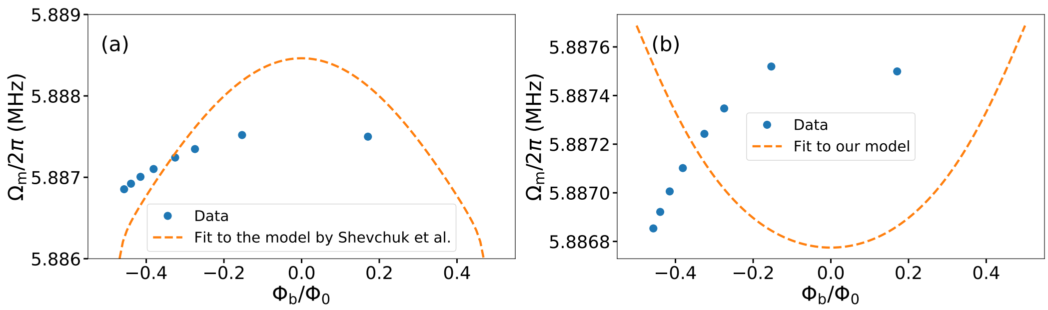

Figure 6.2.5.: (a) Fit of the mechanical frequency $\Omega_\mathrm{m}/2\pi$ to the model from from Ref. [26] given in Eq. 2.78 and (b) to our model given in Eq. 2.83. For both fits, the critical current I_0 as well as L_loop for the fit to our model were fixed to the values obtained from fitting the resonance frequency of the FTR to Eq. 2.65. The mechanical frequency was extracted from measurements at $B_\mathrm{IP} = 30\,\mathrm{mT}$.

measured the frequency tuning curves in decreasing in-plane field and observed shifts of the resonance frequency arcs with respect to zero coil current at certain in-plane field values. These shifts indicate a trapping or sudden release of flux quanta, which might lead to the observed behavior of L_loop. Moreover, we note that the correlations between the fit results for I_0 and L_loop are close to unity, such that the total uncertainty on L_loop might be quite large.

As we have now determined I_0 and L_loop from a fit to the FTR resonance frequency, we can fit the mechanical frequency $\Omega_\mathrm{m}/2\pi$ to the model from Ref. [26] (Eq. 2.78) while fixing I_0. In addition, we fit $\Omega_\mathrm{m}/2\pi$ to our model (Eq. 2.83) while fixing I_0 and L_loop. These fits are shown in Fig. 6.2.5 for an in-plane field of $B_\mathrm{IP} = 30\,\mathrm{mT}$. Surprisingly, the fits do not reproduce the experimental data at all. From the fit to the model in Eq. 2.78, we see that the curvature of the fit is too large to match the data. As the curvature depends on the critical current, we conclude that I_0 extracted from the fit to the flux tuning curve is too large. For the fit to our model, we see that we are in the regime where the valley around $\phi_\mathrm{b} = 0$ is present, meaning that the screening parameter β is quite large (see Sec. 2.4.1). Again, this confirms that the value to which we fix I_0 is too large. The fact that this fitting procedure does not reproduce the experimental data means that the models of the mechanical frequency of a nanostring embedded into a SQUID (Eq. 2.78 and Eq. 2.83) are not consistent with the model of a distributed-element FTR given in Eq. 2.65. In contrast to that latter model, the models of the mechanical frequency consider only a SQUID as the flux-tunable cavity. We suspect that for a consistent fitting routine, a model of the mechanical frequency that considers a distributed-element resonator shunted to ground by a SQUID with integrated nanostring would be needed.

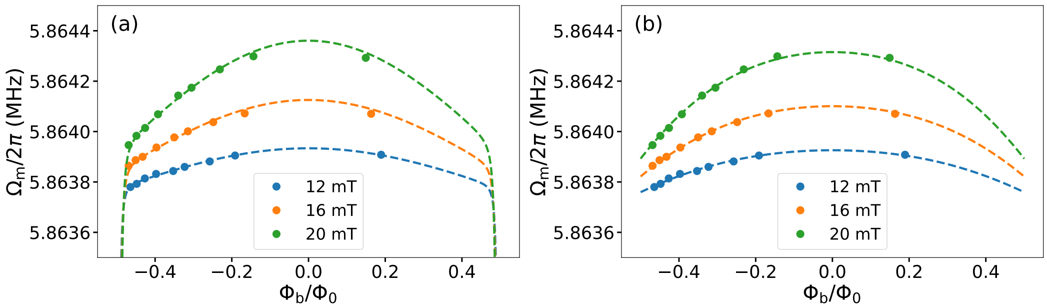

Figure 6.2.6.: Fit of the mechanical frequency $\Omega_m/2\pi$ (a) to the model from Ref. [26] given in Eq. 2.78 and (b) to our model given in Eq. 2.83 at 12 mT, 16 mT and 20 mT. At 12 mT, both $\Omega_0/2\pi$ and I_0 are free fit parameters. At the other in-plane fields, we calculate I_0 based on the value at 12 mT with Eq. 2.42 and retain only $\Omega_0/2\pi$ as free fit parameter. For the fits to our model, we also fix L_{loop} via the fit to the FTR resonance frequency.

Final analysis routine As our approach to fix I_0 to the value obtained from fitting the FTR resonance frequency to Eq. 2.65 did not work out, we decided to analyze the mechanical frequency data using an alternative approach. At the lowest in-plane field (here $B_{\text{IP}} = 12\,\text{mT}$), we fit the mechanical frequency to the model from Ref. [26] (Eq. 2.78) with both Ω_0 and I_0 as free fit parameters. For all subsequent in-plane fields, we extrapolate the critical current $I_0(B_{\text{IP}})$ based on the value at $B_{\text{IP}} = 12\,\text{mT}$ with Eq. 2.42 such that Ω_0 is the only free fit parameter. To do so, we assume a London penetration depth of 16 nm for Al [93], an oxide layer thickness of 4 nm and the length of the JJ perpendicular to the in-plane field is 200 nm. For comparison, we fit the mechanical frequency to our model in Eq. 2.83 as well. Again, we leave Ω_0 and I_0 as free fit parameters at $B_{\text{IP}} = 12\,\text{mT}$ and fix I_0 for the other in-plane fields to the value calculated using Eq. 2.42 taking the same lengths as above. We also fix the loop inductance to the value obtained from fitting the cavity resonance frequency to Eq. 2.65. This is necessary because we do not have a formula that allows us to calculate the loop inductance based on an initial value and we think that having more than one free fit parameter results in a less accurate fit result for Ω_0. Figure 6.2.6 shows fits that were performed this way to the model from Ref. [26] (see panel (a)) and to our model (see panel (b)). In contrast to the previous approach, the fits now match the data well. At $B_{\text{IP}} = 12\,\text{mT}$, we obtain a critical current of $I_0 = 207\,\text{nA}$ when fitting with the model from Ref. [26] and $I_0 = 618\,\text{nA}$ when fitting with our model. These values of I_0 are one order of magnitude smaller than the ones that a fit of the FTR resonance frequency to Eq. 2.65 yields (cf. Tab. 6.2.2).

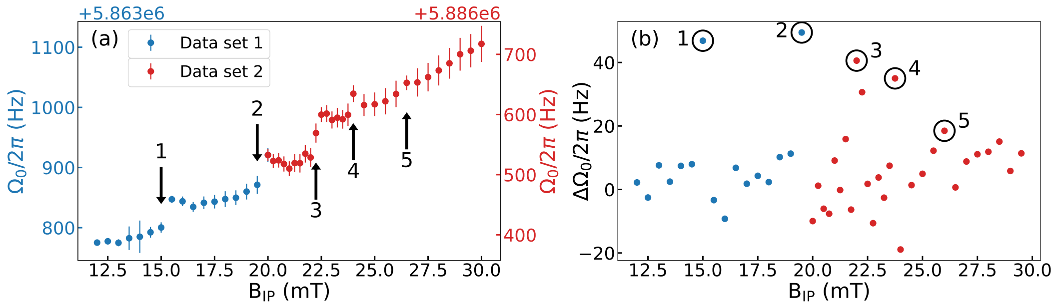

Figure 6.3.1.: First measurement run. (a) Uncoupled mechanical frequency $\Omega_0/2\pi$ as a function of in-plane magnetic field $B_{\rm IP}$. At each $B_{\rm IP}$, $\Omega_0/2\pi$ was extracted from fits of the mechanical frequency as a function of bias flux to Eq. 2.78 (see Sec. 6.2). Black arrows indicate the locations of discontinuities in $\Omega_0/2\pi$. The errorbars capture the statistical uncertainty from the fit to Eq. 2.78 and the uncertainty that is due to the fact that we calculate $I_{\rm c}$ based on the value at 12 mT (see Chap. A for more details). Panel (b) shows the change in the uncoupled mechanical frequency $\Delta\Omega_0/2\pi$ between subsequent in-plane fields. The changes that correspond to the discontinuities in the left panel are encircled and numbered correspondingly. The data is composite from two measurement runs and the axes are aligned based on the mechanical frequency at $B_{\rm IP} = 20$ mT that was determined in both runs.

6.3. Discussion

After having determined the uncoupled mechanical frequency $\Omega_0/2\pi$ for in-plane fields $B_{\rm IP}$ between 12 mT and 30 mT as explained in Sec. 6.2, we can plot $\Omega_0/2\pi$ as a function of $B_{\rm IP}$, shown in Fig. 6.3.1 for the evaluation with the model from Ref. [26] and in Fig. 6.3.3 for the evaluation with our model. The results consist of two data sets that were taken in two independent measurement runs at in-plane fields from 12 mT to 20 mT and from 20 mT to 30 mT. As the sample was warmed up between these two runs, $\Omega_0/2\pi$ shifted from approximately 5.864 MHz to approximately 5.887 MHz. We align the axes in such a way that the data points for the mechanical frequency at $B_{\rm IP} = 20$ mT, that was measured in both runs, coincide.

First, we discuss the results obtained from the evaluation with the model from Ref. [26]. We observe an overall increase of the uncoupled mechanical frequency $\Omega_0/2\pi$ with in-plane field $B_{\rm IP}$ (panel (a) in Fig. 6.3.1). Within the range of $B_{\rm IP}$ probed in the experiments, four clearly visible discontinuities are present at 15.0 mT, 19.5 mT, 22.0 mT and 23.75 mT and a fifth discontinuity might be identified at 26 mT. We note that the fields at which discontinuities are visible do not show an exact periodicity but rather have intervals of the order of 2 mT to 5 mT that seem to decrease with increasing applied field. In panel (b) in Fig. 6.3.1, we show the change in uncoupled mechanical frequency between subsequent in-plane fields $\Delta\Omega_0/2\pi$. (For instance, $\Delta\Omega_0/2\pi\,(12\,\text{mT}) = \Omega_0/2\pi\,(12.5\,\text{mT}) - \Omega_0/2\pi\,(12\,\text{mT})$.) Except for the last one, all discontinuities are associated with frequency changes of the order of 40 Hz, whereas the

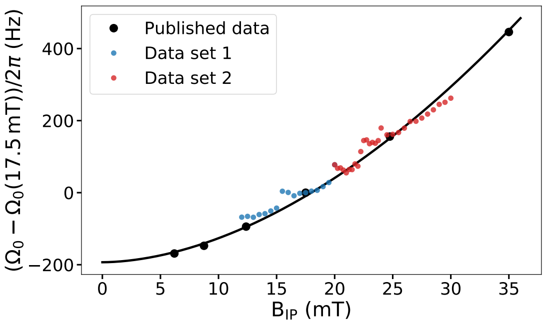

Figure 6.3.2.: Uncoupled mechanical frequency $\Omega_0/2\pi$ as a function of in-plane magnetic field B_{IP}. Blue and red points are our data from Fig. 6.3.1 and black points are data published in Ref. [31]. The black line is a fit to the black data points with Eq. 2.85.

usual frequency change between subsequent in-plane fields is rather $\pm 10\,\mathrm{Hz}$. In Fig. 6.3.2 we superimpose our data for the bare mechanical frequency $\Omega_0/2\pi$ from Fig. 6.3.1 (a) with the data presented in Ref. [31] that was obtained doing the same analysis as described here. We first align the published data and data set 1 such that the data points for the mechanical frequency at $B_{\mathrm{IP}} = 17.5\,\mathrm{mT}$, that is contained in both the published data and data set 1, coincide. Then, we align data set 2 with respect to data set 1 such that the data points for the mechanical frequency at $B_{\mathrm{IP}} = 20\,\mathrm{mT}$ coincide. We see that our data agrees well with the data from Ref. [31] and the fit of that data to Eq. 2.85 that revealed a field dependence of the Labusch parameter following $\alpha \propto B_{\mathrm{IP}}^{1.81}$ (cf. Ref. [31]).

When evaluating the data with our model (see Fig. 6.3.3), the discontinuities persist at the same in-plane fields as in the evaluation with the model from Ref. [26]. Only the last discontinuity (that might also be an artifact) is now located at $25.5\,\mathrm{mT}$. At least for the first three discontinuities, the associated change in $\Omega_0/2\pi$ is again of the order of $40\,\mathrm{Hz}$. In between the discontinuities, $\Omega_0/2\pi$ decreases quite sharply. We suppose that this is related to the fact that we have to fix the loop inductance to the value obtained from fitting the resonance frequency of the FTR to Eq. 2.65, which is a model we have shown to be incompatible with our model for the mechanical frequency shift (Eq. 2.83).

As pointed out in Sec. 2.4.2, the discontinuities in $\Omega_0/2\pi$ might be caused by the creation of single flux lines in the nanostring that couple to the mechanical motion. For this to be the case, the superconducting Al thin film must be in the Shubnikov phase of type-II superconductors. Although Al is a type-I superconductor in the bulk, superconducting thin films are well known to exhibit behavior characteristic of type-II superconductors [73]. The quantity that discriminates type-I from type-II superconductors is the Ginzburg-Landau parameter [50]

$$\kappa = \frac{\lambda_{\mathrm{L}}}{\xi_{\mathrm{GL}}}, \tag{6.3}$$

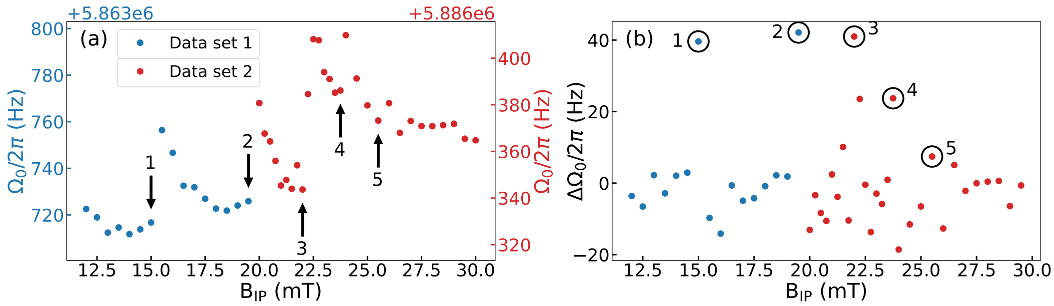

Figure 6.3.3.: First measurement run. (a) Uncoupled mechanical frequency $\Omega_0/2\pi$ as a function of in-plane magnetic field B_{IP}. At each B_{IP}, $\Omega_0/2\pi$ was extracted from fits of the mechanical frequency as a function of bias flux to Eq. 2.83 (see Sec. 6.2). Black arrows indicate the locations of discontinuities in $\Omega_0/2\pi$. The uncertainties on $\Omega_0/2\pi$ that we determine as explained in Chap. A are quite large (several 100 Hz) and not shown for clarity. Panel (b) shows the change in the uncoupled mechanical frequency $\Delta\Omega_0/2\pi$ between subsequent in-plane fields. The changes that correspond to the discontinuities in the left panel are encircled and numbered correspondingly. The data is composite from two measurement runs and the axes are aligned based on the mechanical frequency at $B_{\mathrm{IP}} = 20\,\mathrm{mT}$ that was determined in both runs.

which is the ratio between the two characteristic length scales of a superconductor: the London penetration depth λ_{L} and the Ginzburg-Landau coherence length ξ_{GL}. The London penetration depth is the length scale on which a magnetic field can penetrate the superconductor and the Ginzburg-Landau coherence length sets the length scale of spatial variations of the Cooper pair density. For $\kappa < 1/\sqrt{2}$, the material is a type-I superconductor, whereas for $\kappa > 1/\sqrt{2}$ it is a type-II superconductor [72]. In a thin film, the penetration depth and the coherence length differ from their bulk values $\lambda_{\mathrm{L}}^{\infty}$ and $\xi_{\mathrm{GL}}^{\infty}$ due to a finite mean free path l [50]. For Al, $\lambda_{\mathrm{L}}^{\infty} = 50\,\mathrm{nm}$ and $\xi_{\mathrm{GL}}^{\infty} = 1600\,\mathrm{nm}$ [50]. Our Al thin film does not consist of a single crystal but of multiple grains whose typical size is reported to be of the order of 4 nm [94]. We take this value as an estimate for the mean free path l. In the present limit of $l \ll \xi_{\mathrm{GL}}^{\infty}$, the penetration depth and coherence length can be calculated via the following formulas [50]

$$\lambda_{\mathrm{L}} = \lambda_{\mathrm{L}}^{\infty}\left(1 + \frac{\xi_{\mathrm{GL}}^{\infty}}{l}\right)^{1/2} \tag{6.4}$$

$$\tag{6.5}$$

$$\xi_{\mathrm{GL}} = \xi_{\mathrm{GL}}^{\infty}\left(1 + \frac{\xi_{\mathrm{GL}}^{\infty}}{l}\right)^{-1/2}. \tag{6.6}$$

This yields $\kappa = 12.5$, which shows that we can expect our thin film to behave like a type-II superconductor. For the coherence length, we obtain a value of $\xi_{\mathrm{GL}} = 80\,\mathrm{nm}$, which is comparable to the nanostring's thickness of 110 nm. As the diameter of a vortex is roughly given by ξ_{GL} [50], this means that vortices do fit into the nanostring.

Next, we analyze whether the field interval between the discontinuities in $\Omega_0/2\pi$ agrees with the expected value for the generation of single vortices. In a very naive approach, one can estimate the number n of flux vortices inside the nanostring at a given local field B_{loc} as

$$n = \frac{B_{\mathrm{loc}} l d}{\Phi_0}, \tag{6.7}$$

where l is the length of the nanostring and d its thickness. Thus, to create an additional flux vortex in the nanostring, an increase in the local field of

$$\Delta B_{\mathrm{loc}} = \frac{\Phi_0}{l d} \tag{6.8}$$

is needed. With the value of the flux quantum $\Phi_0 \approx 2 \times 10^{-15}\,\mathrm{V\,s}$, the length of the nanostring $l = 30\,\mu\mathrm{m}$ and its thickness $d = 110\,\mathrm{nm}$, we arrive at a value of $\Delta B_{\mathrm{loc}} \approx 0.6\,\mathrm{mT}$. Next, we want to establish a relation between the local and the external field by taking the diamagnetic response of the superconducting material and the demagnetizing field into account. The demagnetizing field H_{N} arises due to the finite size of the nanostring and the direction in which we apply the external field. It is related to the magnetization M via [50]

$$H_{\mathrm{N}} = -NM, \tag{6.9}$$

where N is known as the demagnetizing factor. In the case of an infinitely long cylinder, $N = 1/2$ when the external field is applied perpendicular to the cylinder's long axis. This case approximates our experimental situation sufficiently well. The local magnetic field inside the nanostring is then given by [50]

$$H_{\mathrm{loc}} = H_{\mathrm{ext}} - NM, \tag{6.10}$$

where H_{ext} is the external magnetic field we apply in the experiment. With the usual relation between magnetic flux density B, the magnetic field H and the magnetization M, the local flux density inside the nanostring reads

$$B_{\mathrm{loc}} = \mu_0(H_{\mathrm{loc}} + M) = B_{\mathrm{ext}} + (1 - N)\mu_0 M, \tag{6.11}$$

where we have inserted Eq. 6.10. We see that this equation relates the local flux density B_{loc} that would be responsible for the creation of vortices to the external flux density B_{ext} that we control experimentally. As superconductors are diamagnets that (partially) expel magnetic fields from their interior, M is negative and we see that B_{loc} is always smaller than B_{ext}. When the type-II superconductor is in the Shubnikov phase, the modulus of the magnetization decreases monotonically with increasing B_{ext}, i.e. M

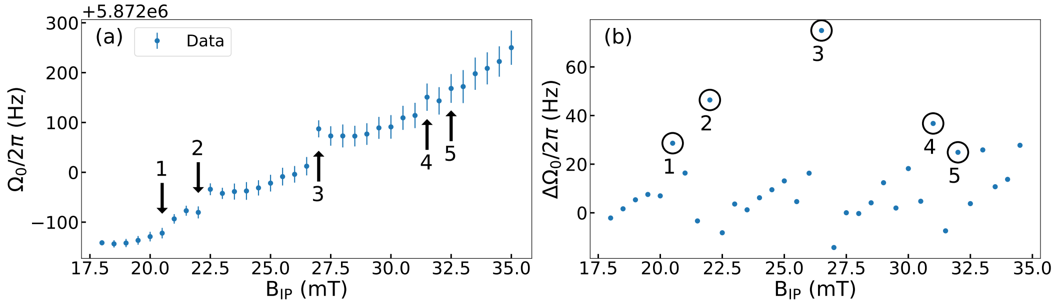

Figure 6.3.4.: Second measurement run. (a) Uncoupled mechanical frequency $\Omega_0/2\pi$ as a function of in-plane field B_{IP}. For each B_{IP}, $\Omega_0/2\pi$ was extracted from fits of the mechanical frequency $\Omega_{\mathrm{m}}/2\pi$ as a function of bias flux to Eq. 2.78. The black arrows indicate the location of discontinuities. Uncertainties on $\Omega_0/2\pi$ were determined as explained in Chap. A. (b) Change in uncoupled mechanical frequency $\Delta\Omega_0/2\pi$ between subsequent in-plane fields as a function of B_{IP}. The frequency changes corresponding to the discontinuities are encircled and numbered correspondingly.

increases. Therefore, the difference between the magnetization at two different external fields $\Delta M > 0$ and we see that $\Delta B_{\mathrm{loc}} > \Delta B_{\mathrm{ext}}$. Thus, we would expect the interval in the external field between the discontinuities to be smaller than 0.6 mT, which is not what we see in the experiment. Therefore, this simple picture does not corroborate the hypothesis that the creation of single vortices in the nanostring is at the origin of the discontinuities we observe experimentally.

From the frequency increase of $\Delta\Omega_0/2\pi = 40\,\mathrm{Hz}$ associated with the discontinuities, we can estimate the change in stiffness of the nanostring that might be due to the sudden presence of an additional vortex. In the approximation of a nanobeam with high tensile stress, the bare mechanical frequency of the nanostring is given by (cf. Eq. 2.76)

$$\frac{\Omega_0}{2\pi} = \frac{1}{2l}\sqrt{\frac{\sigma_0}{\rho}}, \tag{6.12}$$

where σ_0 is the prestress and ρ the density of the nanobeam. The length and the density of the nanostring stay constant during the experiment, such that an increase in frequency can only be brought about by an increased stress $\sigma_0 + \Delta\sigma$. As $\Delta\Omega_0/\Omega_0 \ll 1$, $\Delta\sigma/\sigma_0 \ll 1$ as well and the following expansion is justified:

$$\frac{1}{2l}\sqrt{\frac{\sigma_0+\Delta\sigma}{\rho}} \approx \frac{1}{2l}\sqrt{\frac{\sigma_0}{\rho}}\left(1+\frac{\Delta\sigma}{2\sigma_0}\right) = \frac{\Omega_0}{2\pi} + \frac{\Delta\Omega_0}{2\pi} \tag{6.13}$$

With $\Omega_0/2\pi \approx 5.9\,\mathrm{MHz}$, this yields $\Delta\sigma/\sigma_0 = 2\Delta\Omega_0/\Omega_0 \approx 1.4\times10^{-5}$. Using $\rho = 2700\,\mathrm{kg/m^3}$ [50], we calculate the prestress $\sigma_0 = 338\,\mathrm{MPa}$ and thus obtain $\Delta\sigma = 4.7\,\mathrm{kPa}$.

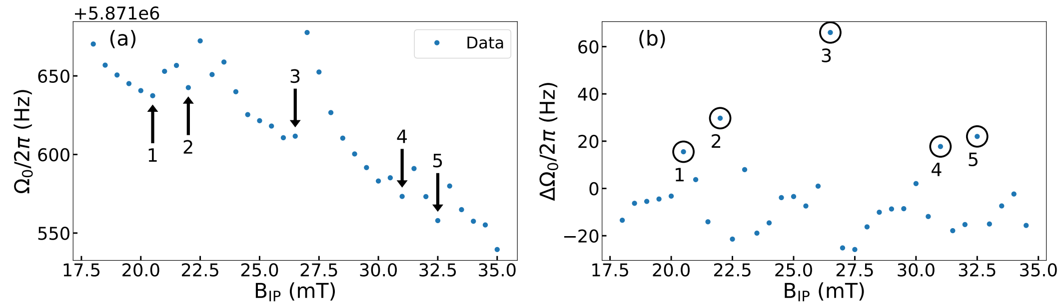

Figure 6.3.5.: Second measurement run. (a) Uncoupled mechanical frequency $\Omega_0/2\pi$ as a function of in-plane field B_{IP}. For each B_{IP}, $\Omega_0/2\pi$ was extracted from fits of the mechanical frequency $\Omega_{\mathrm{m}}/2\pi$ as a function of bias flux to Eq. 2.83. The black arrows indicate the location of discontinuities. Uncertainties on $\Omega_0/2\pi$ determined as explained in Chap. A are quite large (several 100 Hz) and therefore not shown for clarity. (b) Change in uncoupled mechanical frequency $\Delta\Omega_0/2\pi$ between subsequent in-plane fields as a function of B_{IP}. The frequency changes corresponding to the discontinuities are encircled and numbered correspondingly.

Finally, we have confirmed the presence of discontinuities in $\Omega_0/2\pi$ as a function of B_{IP} in a second, independent measurement run. Here, we applied in-plane fields ranging from 18 mT to 35 mT. At 18 mT, both $\Omega_0/2\pi$ and I_{c} are free fit parameters and as before, we extrapolate the critical current at subsequent in-plane fields based on $I_{\mathrm{c}}(18\,\mathrm{mT})$. The result of the evaluation with Eq. 2.78 is shown in Fig. 6.3.4 and with Eq. 2.83 in Fig. 6.3.5. In both figures, panel (a) shows the uncoupled mechanical frequency $\Omega_0/2\pi$ as a function of B_{IP} and panel (b) the change $\Delta\Omega_0/2\pi$ in the uncoupled mechanical frequency between subsequent in-plane fields. When evaluating the data with Eq. 2.78, we observe five discontinuities at in-plane fields that do not coincide with the ones from the first measurement run. Now, the discontinuities are located at in-plane fields of 20.5 mT, 22 mT, 26.5 mT, 31 mT and 32 mT (see Fig. 6.3.4(a)) with corresponding changes $\Delta\Omega_0/2\pi$ between 24 Hz and 75 Hz (see Fig. 6.3.4(b)) that are of the same order as the ones found in the first measurement run. As the errors on $\Omega_0/2\pi$ increase with increasing B_{IP}, the presence of the last two discontinuities is less certain. For the evaluation with Eq. 2.83, the first four discontinuities are found at the same in-plane fields and the fifth discontinuity shifts to 32.5 mT. The corresponding changes $\Delta\Omega_0/2\pi$ now lie between 15 Hz and 66 Hz and are thus comparable to the ones found in the evaluation with Eq. 2.78.

We conclude that the fact that discontinuities in $\Omega_0/2\pi$ persist between independent measurement runs is a strong evidence for a physical origin. As shown in Fig. 6.3.2, our results match the data presented in [31], which means that the physical origin is likely to be related to the coupling between flux line vortices and the mechanical motion of the nanostring. When evaluating data from the same measurement run with the models in

Eq. 2.78 and Eq. 2.83, discontinuities are found at the same in-plane fields and associated with changes of the uncoupled mechanical frequency of roughly 20 Hz to 60 Hz. However, the locations of the discontinuities between different measurement runs do mostly not coincide. Moreover, the magnetic field spacing of 2 mT to 5 mT does not match the predictions of a simple model that assumes that the creation of single vortices leads to discontinuities in Ω_0. Instead, a more complex mechanism involving several vortices might be at the origin of the discontinuities.

Chapter 7.

Summary and outlook

The goal of this thesis was the realization of an inductively coupled nano-electromechanical device that would constitute a major advancement towards the single-photon strong coupling regime. Based on the device presented in Ref. [28], we have developed a multi-step process for the fabrication of a new device generation. Our device consists of a $\lambda/4$ microwave CPW resonator patterned into a Nb thin film and shunted to ground by a SQUID made from Al with mechanically compliant strings. The advantage of this multi-step process in comparison to the device presented in Ref. [28] is that the presence of oxide layers is restricted to the area of the Josephson junctions only. In principle, this greatly reduces the internal loss rate κ_{int} of the flux-tunable resonator and, conversely, enhances the ratio $g_0/\kappa_{\mathrm{int}}$.

We were able to demonstrate high internal quality factors and outstanding stability in external in-plane fields of fixed-frequency Nb CPW resonators, justifying their use as component of the FTRs. In the fabrication of FTRs, we were confronted with several challenges, including the yield of Josephson junctions and insufficient alignment accuracy between subsequent e-beam steps for which we managed to find solutions or workarounds. One of the measured FTRs showed very low Q_{int} that we attributed to the presence of defects introduced in the bandaging process. Moreover, it exhibited a hysteretic frequency tuning behavior and an unusually small Kerr shift. In order to improve the bandaging process, we fabricated a test sample and found a bandaging recipe yielding an increase in Q_{int} by a factor of 1.5 to 2.5. This optimization of the bandaging process can be further continued until arriving at an optimal recipe. Using the improved bandaging recipe, we were able to fabricate a FTR with internal quality factor on the order of 1×10^5. Similar to the first FTR, this second FTR showed hysteretic behavior as well, which might be due to spurious inductances and hence points to the need for an optimization of the current design. A straightforward adjustment would be to enlarge the overlap between bandages and Josephson junctions by increasing the width of the bandaged part of the junctions.

In parallel, using a device of the earlier generation, we built upon the investigation of the mechanical frequency shift in SQUID based nano-electromechanical systems presented in Ref. [31]. We found out that fitting the mechanical resonance frequency as a function of bias flux to the model from Ref. [26] while fixing the critical current to the value extracted from fitting the frequency tuning curve to the model from Ref. [62] does not work. Instead, we came up with a different fitting routine in order to extract the uncoupled mechanical resonance frequency Ω_0. We verified that the obtained results match the data presented in Ref. [31], reaffirming that the coupling of the flux line vortices to the mechanical motion is a plausible explanation for the observed frequency shift. Moreover, we observed discontinuities in Ω_0 as a function of in-plane field B_{IP} and derived an alternative model for the mechanical frequency that confirms the location of the discontinuities. While the appearance of discontinuities is consistent with the flux line lattice theory presented in Refs. [70, 69], we did not find a quantitative explanation for the magnitude and spacing of these discontinuities, but could argue that the magnetic field spacing does not fit to the predictions of a simple model that assumes that flux lines are created in the nanostring one by one. As a next step, a model that is able to distinguish whether pinning of single flux lines or an interplay of several flux lines is at the origin of the observed phenomenon would be highly desirable.

Appendix A.

Uncertainty on the uncoupled mechanical frequency

We take into account two contributions to the uncertainty on the uncoupled mechanical frequency $\Omega_0/2\pi$. First, there is a statistical uncertainty on $\Omega_0/2\pi$ from the fit of the mechanical frequency Ω_m as a function of bias flux to Eq. 2.78 and 2.83, respectively. A second contribution is due to the fact that for each B_IP above 12 mT (or 18 mT for the second measurement run), we calculate the critical current with Eq. 2.42 based on $I_0(12\,\mathrm{mT})$, which itself has a finite statistical uncertainty σ_{I_0}. In order to account for the propagation of this uncertainty to the uncertainty on $\Omega_0/2\pi$, we again fit the mechanical frequency $\Omega_\mathrm{m}/2\pi$, but now with a critical current based on $I_0(12\,\mathrm{mT}) \pm \sigma_{I_0}$. This yields two values for the uncoupled mechanical frequency, $\tilde{\Omega}_{0,+}/2\pi$ and $\tilde{\Omega}_{0,-}/2\pi$ that are slightly different from the original value $\Omega_0/2\pi$. We then take the larger one of the two deviations from $\Omega_0/2\pi$, $|\tilde{\Omega}_{0,+}/2\pi - \Omega_0/2\pi|$ and $|\tilde{\Omega}_{0,-}/2\pi - \Omega_0/2\pi|$, as the additional uncertainty on the uncoupled mechanical frequency.

Appendix B.

Fabrication recipes

(a) Resonators

1) Clean the chip in acetone and isopropanol (IPA).
2) Spin-coat the chip with 40 µL of AZ MIR 701 positive photoresist at 4000 rpm for 60 s.
3) Pre-exposure bake at 90 °C for 75 s
4) Write resonators in a PicoMaster 200 direct laser writer with an exposure of 120 mJ
5) Post-exposure bake at 110 °C for 90 s
6) Development in AZ MIF 726 for 70 s. Move the chip inside the development beaker with tweezers. Stop the development in water for 30 s and transfer the chip to a beaker with unused water. Blow the chip dry with a nitrogen gun.
7) Reactive ion etching (RIE) with Ar ions and SF_6 for about 70 s and for later samples with SF_6 only for about 165 s.
8) Resist removal with Technistrip P1331 at 70 °C for 120 s. Stop in water and clean in IPA.

(b) SQUIDs

1) Dehydrate the chip at 150 °C for 60 s.
2) Bottom layer: spin-coat the chip with 27 µL of AR CSAR 6200.13 at 1500 rpm for 120 s. Then, bake at 150 °C for 60 s.
3) Top layer: spin-coat the chip with 25 µL of AR-P 672.045 PMMA 950K at 1600 rpm for 105 s. Then, bake at 150 °C for 180 s.
4) Do a proximity error correction (PEC) on the layout with *BEAMER* and write the SQUID in the nanobeam with a base dose of 4.5 C/m^2.

5) Development: develop the top layer in AR 600-56 for 180 s, stop in IPA for 30 s. Then, develop the bottom layer in AR 600-546 for 90 s and stop in IPA for 30 s. For later samples, both layers were developed in AR 600-546 for 120 s and stopped in IPA for 30 s.
6) Ozone descumming for 180 s in the Plassys and subsequent evaporation of 150 nm of Al.
7) Lift-off: Put the chip in AR600-71 at 40 °C for at least 2 h. Then, remove Al by carefully blowing with a pipette and rinse in IPA.

(c) Josephson junctions

1) Spin-coat the chip with the double-layer resist stack as for the SQUIDs.
2) PEC with *BEAMER*. Write the junctions in the nanobeam with a base dose of $4.2\,\mathrm{C/m^2}$.
3) Development of the double-layer resist stack as for the SQUIDs.
4) Ozone descumming for 180 s in the Plassys.
5) Evaporation of 30 nm of Al under an angle of 45°.
6) Dynamic oxidation of Al at 5 mTorr for a duration between 30 min and 75 min (cf. main text).
7) After a planetary rotation by 90°, evaporation of 70 nm of Al.
8) Lift-off as for the SQUIDs.

(d) Bandages

1) Spin-coat the chip with the double-layer resist stack as for the SQUIDs.
2) PEC with *BEAMER*. Write the bandages in the nanobeam with a base dose of $4.5\,\mathrm{C/m^2}$.
3) Development of the double-layer resist stack as for the SQUIDs.
4) Ar-ion milling in the Plassys with one of the recipes given in Tab. 5.2.1.
5) Evaporation of about 300 nm of Al, depending on the etch depth resulting from the RIE process.
6) Lift-off as for the SQUIDs.

Bibliography

[1] M. Aspelmeyer, T. J. Kippenberg, and F. Marquardt. “Cavity Optomechanics”. In: *Reviews of Modern Physics* 86 (2014), pp. 1391–1452.

[2] LIGO Scientific Collaboration and Virgo Collaboration et al. “Observation of Gravitational Waves from a Binary Black Hole Merger”. In: *Physical Review Letters* 116 (2016), p. 061102.

[3] C. A. Regal, J. D. Teufel, and K. W. Lehnert. “Measuring Nanomechanical Motion with a Microwave Cavity Interferometer”. In: *Nature Physics* 4 (2008), pp. 555–560.

[4] J. D. Teufel et al. “Nanomechanical Motion Measured with an Imprecision below That at the Standard Quantum Limit”. In: *Nature Nanotechnology* 4 (2009), pp. 820–823.

[5] O. Arcizet et al. “High-Sensitivity Optical Monitoring of a Micromechanical Resonator with a Quantum-Limited Optomechanical Sensor”. In: *Physical Review Letters* 97 (2006), p. 133601.

[6] S. Etaki et al. “Motion Detection of a Micromechanical Resonator Embedded in a d.c. SQUID”. In: *Nature Physics* 4 (2008), pp. 785–788.

[7] M. Poot and H. S. J. van der Zant. “Mechanical Systems in the Quantum Regime”. In: *Physics Reports*. Mechanical Systems in the Quantum Regime 511 (2012), pp. 273–335.

[8] J. Chan et al. “Laser Cooling of a Nanomechanical Oscillator into Its Quantum Ground State”. In: *Nature* 478 (2011), pp. 89–92.

[9] J. D. Teufel et al. “Sideband Cooling of Micromechanical Motion to the Quantum Ground State”. In: *Nature* 475 (2011), pp. 359–363.

[10] S. Gröblacher et al. “Observation of Strong Coupling between a Micromechanical Resonator and an Optical Cavity Field”. In: *Nature* 460 (2009), pp. 724–727.

[11] J. D. Teufel et al. “Circuit Cavity Electromechanics in the Strong-Coupling Regime”. In: *Nature* 471 (2011), pp. 204–208.

[12] E. Verhagen et al. “Quantum-Coherent Coupling of a Mechanical Oscillator to an Optical Cavity Mode”. In: *Nature* 482 (2012), pp. 63–67.

[13] T. A. Palomaki et al. “Coherent State Transfer between Itinerant Microwave Fields and a Mechanical Oscillator”. In: *Nature* 495 (2013), pp. 210–214.

[14] T. A. Palomaki et al. “Entangling Mechanical Motion with Microwave Fields”. In: *Science* 342 (2013), pp. 710–713.

[15] C. F. Ockeloen-Korppi et al. “Stabilized Entanglement of Massive Mechanical Oscillators”. In: *Nature* 556 (2018), pp. 478–482.

[16] S. Kotler et al. “Direct Observation of Deterministic Macroscopic Entanglement”. In: *Science* 372 (2021), pp. 622–625.

[17] E. E. Wollman et al. “Quantum Squeezing of Motion in a Mechanical Resonator”. In: *Science* 349 (2015), pp. 952–955.

[18] J.-M. Pirkkalainen et al. “Squeezing of Quantum Noise of Motion in a Micromechanical Resonator”. In: *Physical Review Letters* 115 (2015), p. 243601.

[19] F. Lecocq et al. “Quantum Nondemolition Measurement of a Nonclassical State of a Massive Object”. In: *Physical Review X* 5 (2015), p. 041037.

[20] M. Forsch et al. “Microwave-to-Optics Conversion Using a Mechanical Oscillator in Its Quantum Ground State”. In: *Nature Physics* 16 (2020), pp. 69–74.

[21] P. Rabl. “Photon Blockade Effect in Optomechanical Systems”. In: *Physical Review Letters* 107 (2011), p. 063601.

[22] J. Qian et al. “Quantum Signatures of the Optomechanical Instability”. In: *Physical Review Letters* 109 (2012), p. 253601.

[23] M. P. Blencowe and E. Buks. “Quantum Analysis of a Linear Dc SQUID Mechanical Displacement Detector”. In: *Physical Review B* 76 (2007), p. 014511.

[24] P. D. Nation, M. P. Blencowe, and E. Buks. “Quantum Analysis of a Nonlinear Microwave Cavity-Embedded Dc SQUID Displacement Detector”. In: *Physical Review B* 78 (2008), p. 104516.

[25] P. D. Nation, J. Suh, and M. P. Blencowe. “Ultrastrong Optomechanics Incorporating the Dynamical Casimir Effect”. In: *Physical Review A* 93 (2016), p. 022510.

[26] O. Shevchuk, G. A. Steele, and Ya. M. Blanter. “Strong and Tunable Couplings in Flux-Mediated Optomechanics”. In: *Physical Review B* 96 (2017), p. 014508.

[27] I. C. Rodrigues, D. Bothner, and G. A. Steele. “Coupling Microwave Photons to a Mechanical Resonator Using Quantum Interference”. In: *Nature Communications* 10 (2019), p. 5359.

[28] P. Schmidt et al. “Sideband-Resolved Resonator Electromechanics Based on a Nonlinear Josephson Inductance Probed on the Single-Photon Level”. In: *Communications Physics* 3 (2020), p. 233.

[29] D. Zoepfl et al. “Single-Photon Cooling in Microwave Magnetomechanics”. In: *Physical Review Letters* 125 (2020), p. 023601.

[30] T. Bera et al. “Large Flux-Mediated Coupling in Hybrid Electromechanical System with a Transmon Qubit”. In: *Communications Physics* 4 (2021), p. 12.

[31] T. Luschmann et al. “Mechanical Frequency Control in Inductively Coupled Electromechanical Systems”. In: *Scientific Reports* 12 (2022), p. 1608.

[32] M. Aspelmeyer, P. Meystre, and K. Schwab. “Quantum Optomechanics”. In: *Physics Today* 65 (2012), pp. 29–35.

[33] J.-Q. Liao and F. Nori. “Single-Photon Quadratic Optomechanics”. In: *Scientific Reports* 4 (2014), p. 6302.

[34] F. Marquardt et al. “Quantum Theory of Cavity-Assisted Sideband Cooling of Mechanical Motion”. In: *Physical Review Letters* 99 (2007), p. 093902.

[35] R. R. Jones et al. “Raman Techniques: Fundamentals and Frontiers”. In: *Nanoscale Research Letters* 14 (2019), p. 231.

[36] A. Nunnenkamp, K. Børkje, and S. M. Girvin. “Single-Photon Optomechanics”. In: *Physical Review Letters* 107 (2011), p. 063602.

[37] M. H. Schleier-Smith et al. “Optomechanical Cavity Cooling of an Atomic Ensemble”. In: *Physical Review Letters* 107 (2011), p. 143005.

[38] F. Brennecke et al. “Cavity Optomechanics with a Bose-Einstein Condensate”. In: *Science* 322 (2008), pp. 235–238.

[39] P. Schmidt. “Inductive Switchable Cavity Electromechanics”. MA thesis. Walther-Meißner-Institut, TU München, 2015.

[40] J. Goetz. “The Interplay of Superconducting Quantum Circuits and Propagating Microwave States”. PhD thesis. 2017.

[41] M. Göppl et al. “Coplanar Waveguide Resonators for Circuit Quantum Electrodynamics”. In: *Journal of Applied Physics* 104 (2008), p. 113904.

[42] J. Zmuidzinas. “Superconducting Microresonators: Physics and Applications”. In: *Annual Review of Condensed Matter Physics* 3 (2012), pp. 169–214.

[43] D. Pozar. *Microwave Engineering*. 4th Edition. John Wiley & Sons, 2012.

[44] C. R. H. McRae et al. “Materials Loss Measurements Using Superconducting Microwave Resonators”. In: *Review of Scientific Instruments* 91 (2020), p. 091101.

[45] C. W. Gardiner and M. J. Collett. “Input and Output in Damped Quantum Systems: Quantum Stochastic Differential Equations and the Master Equation”. In: *Physical Review A* 31 (1985), pp. 3761–3774.

[46] D. F. Walls and G. J. Milburn. *Quantum Optics*. 1st Edition. Springer, 1994.

[47] S. Probst et al. “Efficient and Robust Analysis of Complex Scattering Data under Noise in Microwave Resonators”. In: *Review of Scientific Instruments* 86 (2015), p. 024706.

[48] D. Zoepfl et al. *Kerr Enhanced Backaction Cooling in Magnetomechanics*. 2022. arXiv: `2202.13228 [quant-ph]`.

[49] B. D. Josephson. “Possible New Effects in Superconductive Tunnelling”. In: *Physics Letters* 1 (1962), pp. 251–253.

[50] R. Gross and A. Marx. *Festkörperphysik*. De Gruyter Studium, 2018.

[51] J. M. Martinis and K. Osborne. *Superconducting Qubits and the Physics of Josephson Junctions*. 2004. arXiv: `cond-mat/0402415`.

[52] J. Koch et al. “Charge-Insensitive Qubit Design Derived from the Cooper Pair Box”. In: *Physical Review A* 76 (2007), p. 042319.

[53] J. Clarke and A. Braginski. *The SQUID Handbook*. Vol. 1. Wiley, 2004.

[54] M. Tinkham. *Introduction to Superconductivity*. Second. Dover Publications.

[55] M. Sandberg et al. “Tuning the Field in a Microwave Resonator Faster than the Photon Lifetime”. In: *Applied Physics Letters* 92 (2008), p. 203501.

[56] R. Gross and A. Marx. *Applied Superconductivtiy: Josephson Effect and Superconducting Electronics*. Lecture Notes: Walther-Meißner-Institut, TU München, 2005.

[57] Y.-C. Chen. “Macroscopic Quantum Tunneling in a Dc SQUID”. In: *Journal of Low Temperature Physics* 65 (1986), pp. 133–147.

[58] M. Wallquist, V. S. Shumeiko, and G. Wendin. “Selective Coupling of Superconducting Charge Qubits Mediated by a Tunable Stripline Cavity”. In: *Physical Review B* 74 (2006), p. 224506.

[59] W. Wustmann and V. Shumeiko. “Parametric Resonance in Tunable Superconducting Cavities”. In: *Physical Review B* 87 (2013), p. 184501.

[60] P. Schmidt. “Nanomechanical Quantum Systems”. PhD thesis. Walther-Meißner-Institut, TU München, 2020.

[61] P. Bhupathi et al. “Transient Dynamics of a Superconducting Nonlinear Oscillator”. In: *Physical Review Applied* 5 (2016), p. 024002.

[62] S. Pogorzalek et al. “Hysteretic Flux Response and Nondegenerate Gain of Flux-Driven Josephson Parametric Amplifiers”. In: *Physical Review Applied* 8 (2017), p. 024012.

[63] F. Massel et al. “Microwave Amplification with Nanomechanical Resonators”. In: *Nature* 480 (2011), pp. 351–354.

[64] X. Zhou et al. “Slowing, Advancing and Switching of Microwave Signals Using Circuit Nanoelectromechanics”. In: *Nature Physics* 9 (2013), pp. 179–184.

[65] M. Poot et al. “Tunable Backaction of a DC SQUID on an Integrated Micromechanical Resonator”. In: *Physical Review Letters* 105 (2010), p. 207203.

[66] M. Pernpeintner. “Nanomechanical Hybrid Systems”. PhD thesis. Walther-Meißner-Institut, TU München, 2016.

[67] A. A. Pishchimova et al. *Improving Josephson Junction Reproducibility for Superconducting Quantum Circuits: Junction Area Fluctuation*. 2022. arXiv: `2210.15293 [cond-mat, physics:quant-ph]`.

[68] H. R. Ott. “The Volume Change at the Superconducting Transition of Lead and Aluminum”. In: *Journal of Low Temperature Physics* 9 (1972), pp. 331–343.

[69] P. Esquinazi. “Vibrating Superconductors”. In: *Journal of Low Temperature Physics* 85 (1991), pp. 139–232.

[70] E. H. Brandt, P. Esquinazi, and H. Neckel. “A Superconducting Vibrating Reed Applied to Flux-Line Pinning. I. Theory”. In: *Journal of Low Temperature Physics* 63 (1986), pp. 187–214.

[71] J. Kober et al. “Vibrating-Reed Experiments on Superconducting Suspensions”. In: *Physical Review Letters* 66 (1991), pp. 2507–2510.

[72] A. A. Abrikosov. “The Magnetic Properties of Superconducting Alloys”. In: *Journal of Physics and Chemistry of Solids* 2 (1957), pp. 199–208.

[73] B. L. Brandt, R. D. Parks, and R. D. Chaudhari. “Intermediate State of Thin Superconductors”. In: *Journal of Low Temperature Physics* 4 (1971), pp. 41–63.

[74] A. Gupta et al. “Vibrating Reed Studies on High-Tcsuperconductors”. In: *Bulletin of Materials Science* 14 (1991), pp. 877–882.

[75] A. Schliesser et al. “Resolved-Sideband Cooling of a Micromechanical Oscillator”. In: *Nature Physics* 4 (2008), pp. 415–419.

[76] J. D. Teufel et al. “Dynamical Backaction of Microwave Fields on a Nanomechanical Oscillator”. In: *Physical Review Letters* 101 (2008), p. 197203.

[77] D. P. Pappas et al. “Two Level System Loss in Superconducting Microwave Resonators”. In: *IEEE Transactions on Applied Superconductivity* 21 (2011), pp. 871–874.

[78] N. Bruckmoser. “Development of a Fabrication Process for High-Coherence Niobium Qubits”. MA thesis. Walther-Meißner-Institut, TU München, 2021.

[79] M. V. Costache et al. “Lateral Metallic Devices Made by a Multiangle Shadow Evaporation Technique”. In: *Journal of Vacuum Science & Technology B* 30 (2012), 04E105.

[80] J. M. Kreikebaum et al. “Improving Wafer-Scale Josephson Junction Resistance Variation in Superconducting Quantum Coherent Circuits”. In: *Superconductor Science and Technology* 33 (2020), 06LT02.

[81] J. Goetz et al. “Loss Mechanisms in Superconducting Thin Film Microwave Resonators”. In: *Journal of Applied Physics* 119 (2016), p. 015304.

[82] A. Dunsworth et al. “Characterization and Reduction of Capacitive Loss Induced by Sub-Micron Josephson Junction Fabrication in Superconducting Qubits”. In: *Applied Physics Letters* 111 (2017), p. 022601.

[83] G. J. Dolan. “Offset Masks for Lift-off Photoprocessing”. In: *Applied Physics Letters* 31 (1977), pp. 337–339.

[84] P. Krantz et al. “A Quantum Engineer’s Guide to Superconducting Qubits”. In: *Applied Physics Reviews* 6 (2019), p. 021318.

[85] S. Weichselbaumer. “Spin Dynamics in Strongly Coupled Spin-Photon Hybrid Systems”. PhD thesis. Walther-Meißner-Institut, TU München, 2020.

[86] A. P. M. Place et al. “New Material Platform for Superconducting Transmon Qubits with Coherence Times Exceeding 0.3 Milliseconds”. In: *Nature Communications* 12 (2021), p. 1779.

[87] C. Song et al. “Microwave Response of Vortices in Superconducting Thin Films of Re and Al”. In: *Physical Review B* 79 (2009), p. 174512.

[88] R. Reuschling and E. Schultheiss. “Ion Sources for Vacuum Thin Film Technology”. In: *Vakuum in Forschung und Praxis* 18 (2006), pp. 46–51.

[89] F. Hocke. “Microwave Circuit-Electromechanics in a Nanomechanical Hybrid System”. PhD thesis. Walther-Meißner-Institut, TU München, 2013.

[90] I. C. Rodrigues. “Coupling Harmonic Oscillators to Superconducting Quantum Interference Cavities”. PhD thesis. Delft University of Technology, 2021.

[91] I. Besedin and A. P. Menushenkov. “Quality Factor of a Transmission Line Coupled Coplanar Waveguide Resonator”. In: *EPJ Quantum Technology* 5 (2018), p. 2.

[92] M. Xu et al. “Frequency-Tunable High-Q Superconducting Resonators via Wireless Control of Nonlinear Kinetic Inductance”. In: *Applied Physics Letters* 114 (2019), p. 192601.

[93] C. Kittel. *Introduction to Solid State Physics*. 8th Edition. John Wiley & Sons, Inc., 2005.

[94] G. Deutscher et al. “Transition to Zero Dimensionality in Granular Aluminum Superconducting Films”. In: *Journal of Low Temperature Physics* 10 (1973), pp. 231–243.

Acknowledgements

It goes without saying that this master's thesis is not only my work, but the work of many people who have advised, supported and encouraged me throughout the last year. In particular, I would like to express my gratitude to the following people.

Hans, I would like to thank you for the opportunity to write my thesis in your group and for your valuable scientific input! Thank you for taking your time to discuss with me, be it problems in the fabrication of FTRs or new theory models. Also, I am very grateful to you for giving me an extension of four weeks, which made things much easier for me. Under your experienced guidance, I was always confident to bring my thesis to a good end.

Thomas, I think I could not have wished for a better advisor than you. At any time, I had the feeling that we were working together on this topic and you were always prepared to give me helpful advice on almost any question I would ask you. Especially your support in the lab was extremely valuable to me and I am thankful that I could measure a large chunk of the data for this thesis on your setup! Apart from working together, I also enjoyed our non-scientific conversations at lunch or in the office. You know I had some hard times during this year, but without you, they would have been much harder.

Alex, I was very lucky that you started your master's thesis at the same time as me! The tips and tricks on Python, Adobe Illustrator and LaTeX you shared with me made my life much easier and it was a good feeling to see that you were interested in my work and cared about the problems I encountered. Our scientific discussions were an enrichment to me and the discussions on other topics just as much.

Julian, I am glad we moved to a new office in late summer that serves you as a regular stopover on your ways through the institute, as this way, we got to know each other much better than before. The DPG conference in Regensburg with you was one of the best experiences during my time at the WMI. Thank you for cheering me up every day with your memes and funny ideas! At the same time, I appreciate that we can also talk seriously and that you were truly interested in how I was doing. Last but not least, your notes on the derivation of the scattering parameters were very helpful in writing up that part for my own thesis.

Christian, you were the laid-back guy in our office who was not taking things as seriously as the others. Thank you for being that way, as this master's thesis was stressful enough for me anyways! It was interesting to listen to your stories from your semester in South Korea and your supply of random facts from the Internet was definitely diverting.

Patricia, talking to you was always a pleasure due to your open-minded and supportive personality! Hearing your perspective as a recently graduated student on the struggles of a master's thesis was comforting and gave me strength to keep going. I especially remember the day you introduced me to your measurement setup when I did not feel like working and the delicious cake you brought for your birthday.

Kedar, you were the first guy I ran into on my first day at the institute and I immediately knew you were a kind and helpful person. In particular, I want to thank you for carrying out HF dips for me several times, helping me when the Plassys stopped working and of course for initiating and advancing our bandaging project! I spite of your challenging work, you always keep your serenity and that is admirable to me.

Daniil, although we did not really work together during the last year, it was nonetheless a delight being in your company at the institute. I especially enjoyed talking in Russian with you and your compliments on my language skills made me happy!

Leon, thank you for teaching me the basics of working in the clean room and for your valuable tips for the fabrication of my samples!

Niklas, thank you for sharing tricks and knowledge of clean room fabrication with me and for your immediate help when I was struggling with the laser writer or wire bonder.

Franz, thank you that I could rely on your soldering skills whenever I had to solder my coil to a Fischer connector and for your patience and help that day when we measured one of my FTRs that miraculously disappeared.

Lastly, I want to express my deep gratitude to my parents, my sisters and my grandparents for their steady support and unconditional love, not only during this master's thesis, but during my whole studies. You were the ones I could share both my excitement and my frustration with and you always encouraged me to keep going and keep believing in myself. Especially my mother was a source of constant moral support for me during the past months. Although the master's certificate will carry my name, it is in large part to you!